

OBJECTIVE ASSESSMENT OF IMAGE QUALITY (OAIQ) IN FLUORESCENCE-ENHANCED OPTICAL IMAGING

A Dissertation

by

AMIT K. SAHU

Submitted to the Office of Graduate Studies of
Texas A&M University
in partial fulfillment of the requirements for the degree of

DOCTOR OF PHILOSOPHY

December 2006

Major Subject: Chemical Engineering

**OBJECTIVE ASSESSMENT OF IMAGE QUALITY (OAIQ) IN
FLUORESCENCE-ENHANCED OPTICAL IMAGING**

A Dissertation

by

AMIT K. SAHU

Submitted to the Office of Graduate Studies of
Texas A&M University
in partial fulfillment of the requirements for the degree of

DOCTOR OF PHILOSOPHY

Approved by:

Co-Chairs of Committee,	Eva M. Sevick-Muraca Mahmoud El-Halwagi
Committee Members,	Michael A. Bevan Wolfgang Bangerth
Head of Department,	N. K. Anand

December 2006

Major Subject: Chemical Engineering

ABSTRACT

Objective Assessment of Image Quality (OAIQ) in Fluorescence-Enhanced Optical
Imaging. (December 2006)

Amit K. Sahu, B. Tech., Indian Institute of Technology, Roorkee, India

Co-Chairs of Advisory Committee: Dr. Eva Marie Sevick-Muraca
Dr. Mahmoud El-Halwagi

The statistical evaluation of molecular imaging approaches for detecting, diagnosing, and monitoring molecular response to treatment are required prior to their adoption. The assessment of fluorescence-enhanced optical imaging is particularly challenging since neither instrument nor agent has been established. Small animal imaging does not address the depth of penetration issues adequately and the risk of administering molecular optical imaging agents into patients remains unknown. Herein, we focus upon the development of a framework for OAIQ which includes a lumpy-object model to simulate natural anatomical tissue structure as well as the non-specific distribution of fluorescent contrast agents. This work is required for adoption of fluorescence-enhanced optical imaging in the clinic.

Herein, the imaging system is simulated by the diffusion approximation of the time-dependent radiative transfer equation, which describes near infra-red light propagation through clinically relevant volumes. We predict the time-dependent light propagation within a 200 cc breast interrogated with 25 points of excitation illumination and 128 points of fluorescent light collection. We simulate the fluorescence generation from Cardio-Green at tissue target concentrations of 1, 0.5, and 0.25 μM with

backgrounds containing 0.01 μM . The fluorescence boundary measurements for 1 *cc* spherical targets simulated within lumpy backgrounds of (i) endogenous optical properties (absorption and scattering), as well as (ii) exogenous fluorophore cross-section are generated with lump strength varying up to 100% of the average background. The imaging data are then used to validate a PMBF/CONTN tomographic reconstruction algorithm. Our results show that the image recovery is sensitive to the heterogeneous background structures. Further analysis on the imaging data by a Hotelling observer affirms that the detection capability of the imaging system is adversely affected by the presence of heterogeneous background structures. The above issue is also addressed using the human-observer studies wherein multiple cases of randomly located targets superimposed on random heterogeneous backgrounds are used in a “double-blind” situation. The results of this study show consistency with the outcome of above mentioned analyses. Finally, the Hotelling observer’s analysis is used to demonstrate (i) the inverse correlation between detectability and target depth, and (ii) the plateauing of detectability with improved excitation light rejection.

DEDICATION

To Ma and Papa

ACKNOWLEDGEMENTS

I would like to extend my gratitude to a number of people who helped me progress relatively steadily through the arduous path of doctoral studies (pardon the cliché). First, I am grateful to Dr. Eva Sevick, my advisor and teacher, for helping me ease through my research objectives as a Ph.D. student. I am amazed at her skills as an efficient professional and hope to emulate those as much as I possibly can into my future endeavors. Next, I want to thank my previous advisors, Dr. Michael A. Bevan and Dr. David M. Ford, for the help and support they provided me at the initial stages of my studies at Texas A&M. I thank Dr. Mahmoud El-Halwagi (co-chair) and Dr. Wolfgang Bangerth (committee member) for their help and suggestions.

I am very thankful to the members of the Photon Migration Laboratories (PML) for making my stay a learning as well as an enjoying experience. I especially thank Dr. Amit Joshi for helping me understand the fundamentals of Optical Tomography and I wish him my best in his future endeavors. Collaborator Dr. Matthew A. Kupinski's help in understanding statistical analysis added greatly to my work. Former member of PML, Dr. Ranadhir Roy, was a great help at the beginning of my Ph.D. work and I am grateful to him for that. I appreciate the support of my colleagues Dr. Sarabjot Dali, Dr. Tianshu Pan, Kildong Hwang, John Rasmussen, Dr. Feng Liang, Sunkuk Kwon, Dr. Daniel Lee, Ruchi Sharma, Laxmi Sampath, Arlin Cameron, and Dr. Kristen Adams. I am grateful to Martha Stafford (former Administrative Assistant at PML), Towanna

Hubacek (Program Assistant at Chemical Engineering Department) and Jessica Nollkamper (Administrative Assistant at PML) for helping me in many ways.

My sincere gratitude to the friends at IIT-Roorkee and TAMU-College Station for being my pals in good times and bad times.

Finally, I would like to convey my deepest regards to my parents, Brijbhan and Usha Sahu, and my sisters, Jyoti, Aarati and Bharati, for the unconditional love they have bestowed upon me over the years. To them I dedicate this dissertation.

ABBREVIATIONS

ADC	Analog-to-digital converter
AMD	Advanced Micro Devices, Inc.
AUC	Area under the curve
CCD	Charged-couple device
CG	Conjugate gradient
CONTN	Constrained truncated Newton
CPU	Central processing unit
DOT	Diffuse optical tomography
EBC	Extrapolated boundary condition
FD	Finite difference
FDPM	Frequency domain photon migration
FEM	Finite element method
FOV	Field of view
FWHM	Full width at half maximum
GMV	General mesh viewer
GN	Gauss-Newton
GPST	Generalized pulse spectrum technique
ICD	Iterative coordinate descent
ICG	Indocyanine green
MCP	Micro channel plate
MSE	Mean square error
NIR	Near infrared
NRMSE	Normalized root mean square error
OAIQ	Objective assessment of image quality
OD	Optical density
PCB	Partial current boundary

PDF	Probability distribution function
PET	Positron emission tomography
PMBF	Penalty modified barrier function
RMSE	Root mean square error
RAM	Random access memory
ROC	Receiver operating characteristic
RTE	Radiative transfer equation
SDT	Signal detection theory
SKE	Signal-known-exactly
SNR	Signal-to-noise ratio
SPECT	Single photon emission computed tomography
SSS	Strict sense stationary
TBR	Target to background ratio
TN	Truncated Newton
WSS	Wide sense stationary
ZBC	Zero-boundary condition

NOMENCLATURE

b	The lumpy background
b_0	Spatial mean of the lumpy background
$\underline{\mathbf{B}}_{x \rightarrow m}$	Coupling matrix
c	Speed of light in the medium
D	Dirac matrix
d^k	Search direction for k th step of the optimization process
D_x^e	Average value of D_x over the element ‘ e ’, etc.
$D_{x,m}$	Photon diffusion coefficients at excitation/emission wavelengths
E_{Φ_m}	Error function representing mismatch between Φ_m^{meas} and Φ_m^{calc}
\mathbf{f}	A vector containing the spatial values of the optical parameter being imaged
FNF	False-negative fraction
FPF	False-positive fraction
g	Coefficient of anisotropy of the medium
\mathbf{g}	A vector containing the measurements at the specified boundary locations
$\Delta \bar{\mathbf{g}}$	Vector difference in the means of \mathbf{g} under H_1 and H_0 hypotheses
\mathbf{H}	The imaging operator
H_0	Signal-absent hypothesis
H_1	Signal-present hypothesis
$\mathbf{H}_{E_{\Phi_m}}$	Hessian sensitivity matrix of the error function E_{Φ_m}
I	Intensity of the transmitted light
I_0	Intensity of the incident light
$I_{AC_{x,m}}$	Amplitudes of the photon density wave at excitation/emission wavelengths
$I_{AC_{refp}}$	Referenced AC intensity at node p
$\mathbf{J}_{E_{\Phi_m}}$	Jacobian sensitivity matrix of the error function E_{Φ_m}

\mathbf{K}_g	Average covariance of the vector \mathbf{g}
$\mathbf{K}_{\bar{g}}$	Average-data covariance matrix
$\bar{\mathbf{K}}_n$	Average noise-covariance matrix
K_n	Number of lumps in the n th cluster
K_{nr}	The rate constant for non-radiative relaxation
$\underline{\mathbf{K}}_{x,m}$	Elemental stiffness matrices
l_0	Lump strength
M	Total number of boundary measurements
n	Optical refractive index of the medium
\mathbf{n}	Noise vector
N	Total number of nodes in the discretized domain
$\hat{\mathbf{n}}$	Outward drawn normal to the surface of the boundary
n_1	Refractive index of the turbid medium
n_2	Refractive index of the outside medium
N_{cl}	Number of clusters in clustered lumpy background
N_{FN}	Number of false-negatives
N_{FP}	Number of false-positives
n_{rel}	Relative refractive index
N_{TN}	Number of true-negatives
N_{TP}	Number of true-positives
N_p	Number of lumps
$\mathbb{N}(0,1)$	Gaussian distribution with zero mean and unit variance
n_θ	Noise estimate in the phase measurements
$pr(t H_j)$	PDF on t depend on the underlying hypothesis H_j
OD_λ	Optical density value at some wavelength
\mathbf{r}	Location of some point in a 3D space
$[\mathbf{r}]$	Residual vector representing mismatch between Φ_m^{meas} and Φ_m^{calc}
\mathbf{r}_C	Centroid of the reconstructed target

R_{eff}	Effective refractive index
$R_{Fresnel}$	Fresnel reflection coefficient
R_j, R_ϕ	Fresnel's reflections
\mathbf{r}_n	Uniformly distributed location of the n th lump
R_{ϕ_n}	Rotation matrix
S	Photon source strength
SNR_{Hot}	The Hotelling observer's signal-to-noise ratio
$SNR_{opt\ lin}$	Signal-to-noise ratio of the optimal linear observer
$\underline{\mathbf{S}}_x$	Excitation source matrix
T	Transmittance
$T(\mathbf{g})$	Discriminating function for data \mathbf{g}
$\langle t \rangle_j$	Mean of t under hypothesis H_j
TNF	True-negative fraction
TPF	True-positive fraction
$V(\Omega)$	Volume of the hemispherical portion of the breast geometry
w	Lump width
$\mathbf{w}_{opt\ lin}$	Optimal linear discriminant
\perp	The normal direction outward to the surface
$\langle \dots \rangle_{n f}$	Average over all noise for a fixed object
$\langle \dots \rangle_{n,f}$	Average over all noise and object variations
$\ \dots \ _{L_2}$	The L_2 norm (alternatively written as $\ \dots \ $)
∇	The del operator
χ_{Hot}	Hotelling observer's test statistic
ϕ	Fluorescence quantum
ϕ_n	A solid angle uniformly distributed between 0 and 4π
Φ_m^{calc}	Photon emission fluence calculated from forward solver
Φ_m^{meas}	Experimentally measured photon emission fluence

$\Phi_{x,m}$	Excitation/emission photon fluence rates
γ	Constant related to the optical refractive index mismatch at the boundary
Γ	First order rate constant for radiative relaxation
λ	Lagrange multiplier term in PMBF/CONTN algorithm
λ_m	Wavelength of the emission photon density waves
λ_x	Wavelength of the excitation photon density waves
$\mu_{ax,mf}$	Exogenous absorption coefficients at excitation/emission wavelengths
$\mu_{ax,mi}$	Endogenous absorption coefficients at excitation/emission wavelengths
$\mu_{sx,m}$	Scattering coefficients at excitation/emission wavelengths
η	Penalty/barrier term in PMBF/CONTN algorithm
σ_j	Standard deviation of test statistic under H_j hypothesis
θ_c	Critical angle for the total internal reflection at the tissue/outside boundary
θ_{ref_p}	Referenced phase at node p
$\theta_{x,m}$	Phase lags at excitation/emission wavelengths
τ	Fluorescence lifetime
Ω	The domain representing the hemispherical portion of the breast geometry
ω	Modulation frequency of the NIR source
ξ	Uniformly distributed random number in $[0, 1]$

TABLE OF CONTENTS

	Page
1. INTRODUCTION.....	1
1.1 Motivation	1
1.2 Specific aims	6
1.3 Organization of dissertation	8
2. BACKGROUND.....	9
2.1 Fluorescence photon migration	9
2.1.1 Boundary conditions	15
2.2 Fluorescence-enhanced optical tomography	18
2.2.1 Modeling photon transport (forward problem)	19
2.2.2 Image reconstruction (inverse problem)	26
2.2.2.1 Newton method	28
2.2.2.2 Gauss-Newton method	31
2.2.2.3 Truncated Newton method	32
2.2.2.4 Trust region methods	33
2.2.2.5 Constrained optimization	34
2.3 Object models.....	35
2.3.1 Lumpy-object model	35
2.3.2 Clustered lumpy-object model	36
2.4 Objective assessment of image quality (OAIQ).....	37
2.4.1 System model	39
2.4.2 Detection tasks	40
2.4.3 Hardware design.....	43
3. EVALUATION OF ANATOMICAL STRUCTURE AND NON-UNIFORM DISTRIBUTION OF IMAGING AGENT IN NEAR-INFRARED FLUORESCENCE-ENHANCED OPTICAL TOMOGRAPHY.....	48
3.1 Introduction	48
3.2 Methods	52
3.2.1 Forward model and finite element solver.....	53
3.2.2 Endogenous and exogenous optical property heterogeneity	54
3.2.3 Inverse imaging algorithm	60
3.2.4 Figures of merit for image analysis.....	64
3.3 Results and discussion.....	65
3.3.1 Generation of lumpy backgrounds	65
3.3.2 Tomographic image reconstruction.....	65
3.4 Conclusions	75

	Page
4. ASSESSMENT OF A FLUORESCENCE-ENHANCED OPTICAL IMAGING SYSTEM USING THE HOTELLING OBSERVER.....	76
4.1 Introduction	76
4.2 Methods.....	79
4.2.1 The imaging equation.....	79
4.2.2 Simulated background heterogeneity	83
4.2.3 Experimental conditions.....	86
4.2.3.1 Excitation light leakage.....	86
4.2.3.2 Noise.....	89
4.2.4 Detection tasks	91
4.2.4.1 Hotelling observer	92
4.2.5 Simulated measurements.....	94
4.3 Results	95
4.3.1 Influence of lump strength	97
4.3.2 Influence of target depth	99
4.3.3 Influence of excitation light rejection efficiency	101
4.4 Discussion	101
4.5 Conclusions	104
5. PSYCHOPHYSICAL ANALYSIS OF THE RECONSTRUCTED IMAGES BASED ON A GAUSS-NEWTON ALGORITHM	106
5.1 Introduction	106
5.2 Methods.....	108
5.2.1 The imaging model and the reconstruction algorithm	109
5.2.2 Psychophysical analysis	114
5.2.2.1 The ROC curve.....	116
5.2.3 Simulated imaging data.....	117
5.3 Results and discussion.....	120
5.3.1 Sensitivity of the classifier performance to background variations	120
5.4 Conclusions	126
6. CONCLUSIONS AND SUGGESTED FUTURE WORK.....	128
6.1 Future directions.....	130
REFERENCES.....	132
APPENDIX A	150
APPENDIX B	152

	Page
APPENDIX C	156
VITA	158

LIST OF TABLES

	Page
Table 1.1 Review of the literature for the image quality assessment approaches in near-infrared (NIR) diffusion optical imaging.	4
Table 3.1 Experimental breast optical property values reported in literature.	50
Table 3.2 Constant factors to obtain lumps at emission wavelength from the generated lumps at excitation wavelength.	58
Table 3.3 Average background optical properties. Also given are the parameters used in equations (3.2) through (3.4). The optical properties used in the simulations are similar to breast tissue optical properties reported in literature (see Table 3.1).....	59
Table 3.4 Centroid of the reconstructed targets with varying lump intensities. The coordinate dimensions are in centimeters.	69
Table 3.5 The mean displacement of the reconstructed targets with respect to the actual target's centroid. The dimension is in centimeters.	70
Table 4.1 Average background optical properties. The parameters used to solve the coupled diffusion equations are also tabulated.	82

Table 5.1 Results of the Qualitative Analysis (Visual Inspection): A human observer's decisions on the presence of a randomly located 1 cc spherical fluorescent target (at depths 2 cm or less from the hemispherical surface of the breast-shaped geometry) having 50 times more contrast than the background. The background endogenous optical properties are heterogeneous in nature represented by the lumpy-object model (Number of lumps, $N_p=100$; lump width, $w=0.5$ cm).	122
Table 5.2 Results of the Qualitative Analysis (Visual Inspection): A human observer's decisions on the presence of a randomly located 1 cc spherical fluorescent target (at depths 2.5 cm or less from the hemispherical surface of the breast-shaped geometry) having 50 times more contrast than the average background. The background endogenous as well as exogenous optical properties are heterogeneous in nature represented by the lumpy-object model (Number of lumps, $N_p=50$; lump width, $w=0.5$ cm).....	123

LIST OF FIGURES

	Page
Fig. 1.1 Organization of the dissertation.	8
Fig. 2.1 Illustration of the frequency domain photon migration. Intensity modulated photon density wave of wavelength λ_x is launched into the system, which propagates and encounters a fluorophore molecule, giving rise to fluorescent emission wave of wavelength λ_m	12
Fig. 2.2 Jablonski diagram showing that the excited photon relaxes radiatively while emitting the fluorescence light. Various S denote the singlet electronic states of the fluorophore molecule. http://laxmi.nuc.ucla.edu:8248/M248_98/synprob/part1/prop_fprob.html	13
Fig. 2.3 Boundary surface of the strongly scattering turbid medium. The turbid medium and the outside have refractive indices of n_1 and n_2 respectively. $\hat{\mathbf{n}}$ is the outward drawn normal to the surface of the boundary.	15
Fig. 2.3 A tetrahedral element ' e ' with nodes ' i ', ' j ', ' k ', and ' l '. In finite element method, a given domain is discretized into elements such as this one. First, the solution is sought over each such individual element, and then the overall solution is obtained by combining the elemental solutions.	22
Fig. 3.1 The geometry of the breast-shaped phantom. The dimensions are in centimeters. The bigger cylindrical volume has a circular base of diameter 20 cm. The hemisphere has a radius of 5 cm.	56

- Fig. 3.2 The positions of laser sources and detectors on the breast phantom. The stars are the positions of the sources and the circles are the positions of the detectors. 60
- Fig. 3.3 Figures of the lumps in endogenous and exogenous optical properties using Lumpy object model. The lumps in μ_{axi} (a), μ_{sx} (b), and μ_{axf} (c) are shown as the cutplanes to the breast geometry (Fig. 3.1) parallel to yz-plane and passing through $x=0.20$ cm. The spread of the lumps are 5mm and there are 100 lumps uniformly generated in the hemispherical volume. The lumps have the strength values of 25% of the average background values of μ_{axi} , μ_{sx} , and μ_{axf} given in Table 3.3. 66
- Fig. 3.4 Actual distribution of exogenous optical property of the target inside the breast phantom. The colorbar shows the values of μ_{axf} in cm^{-1} . The target has μ_{axf} value 100 times more than that of the background. The Fig. shown is a cut plane parallel to yz-plane and passing through point $x=0.5$. The lumps in the background are not shown here. 67
- Fig. 3.5 Figure showing the recovered distribution of exogenous optical property in the presence of 1% lumps in endogenous optical properties using the PMBF/CONTN inverse algorithm. The figure shows the isosurface corresponding to the 70% of the maximum value of the reconstructed μ_{axf} 68
- Fig. 3.6 The root mean square error (RMSE) values of the reconstructed images in the presence of endogenous lumps in the background. The target-to-background ratio (TBR) is 100:1 and the RMSE is calculated with respect to the actual distribution of the fluorophore shown in Fig. 3.4. 70

- Fig. 3.7 The recovered distribution of exogenous optical property in the presence of 1% lumps in endogenous as well as exogenous optical properties using the PMBF/CONTN inverse algorithm. Figures (a), (b), and (c) are respectively for TBR values of 100:1, 50:1, and 25:1. The figures show the isosurfaces corresponding to the 70% of the maximum value of the reconstructed μ_{axf}72
- Fig. 3.8 The root mean square error (RMSE) values of the reconstructed images in the presence of endogenous as well as exogenous lumps in the background. The plots for all the three cases of TBR values are shown and the RMSE is calculated with respect to the actual distribution of the fluorophore including the target distribution shown in Fig. 3.4 and the exogenous lumps in the background. The values for 100% are not shown here since we could not reconstruct the target for the TBR values of 50 and 25.73
- Fig. 4.1 The breast-shaped geometry consisting of a 10 *cm* diameter hemispherical top to simulate a human breast. The bottom cylindrical base has 20 *cm* diameter and is 2.5 *cm* high. Also shown is 1 *cm*³ target at a depth *d*. All dimensions are in centimeters.....82
- Fig. 4.2 The locations of the point sources and detectors on the breast-shaped geometry. The red points denote the sources and the blue points denote the detectors.83

- Fig. 4.3 Schematic of the experimental setup. The various components are labeled to describe: (A) a gain-modulated image intensifier, (B) a 16-bit cooled CCD camera, (C) a modulated laser diode used as a light source, (D) an 830-nm band pass filter, (E) a holographic notch filter, (F) the breast shaped phantom, and (G) the detector fibers leading to an interfacing plate. The Figure is not to scale.....87
- Fig. 4.4 Lumpy backgrounds of endogenous and exogenous optical properties using Lumpy object model. The lumps in μ_{axi} , μ_{sx} , and μ_{axf} are shown as cutplanes to the breast geometry (Fig. 4.1) parallel to yz-plane and passing through $x=-1$ cm. In each case, one hundred lumps are uniformly generated in the hemispherical volume with spatial spreads of 5 mm and strength values equal to hundred percent of the average background values of optical properties as given in Table 4.1.....96
- Fig. 4.5 SNR_{Hot} computed from simulated measurements of light intensity (filled circles) and phase (open circles) as a function of strength of lumps in (a) the endogenous optical properties, and (b) endogenous as well as exogenous optical properties vs. the strength of lumps. The target is a 1 cm^3 spherical volume at a depth of 1 cm and contrasted from its surroundings by 10:1. The centroid of the target is at (0, 0, 4) inside the breast geometry (Fig. 4.1).....98
- Fig. 4.6 SNR_{Hot} computed from simulated measurements of light intensity (filled circles) and phase (open circles) in homogeneous background of optical properties vs. the depth of 1 cm^3 spherical target contrasted from its surroundings by 10:1. The centroid of the target lies in the z-axis of breast geometry (Fig. 4.1). The target depth is measured as the distance from its centroid to the point (0, 0, 5) in breast geometry.100

- Fig. 4.7 SNR_{Hot} computed from simulated measurements of light intensity (filled circles) and phase (open circles) in hundred percent lumpy backgrounds of endogenous (μ_{axi} , μ_{ami} , μ_{sx} , and μ_{sm}) as well as exogenous (μ_{axf} , and μ_{amf}) optical properties vs. the depth of 1 cm^3 spherical target contrasted from its surroundings by 10:1. The centroid of the target lies in the z-axis of breast geometry (Fig. 4.1). The target depth is measured as the distance from its centroid to the point (0, 0, 5) in breast geometry. 100
- Fig 4.8 SNR_{Hot} computed from simulated measurements of (a) intensity, I_{AC} , and (b) phase, θ , in one hundred percent lumpy backgrounds of endogenous as well as exogenous optical properties vs. the depth of 1 cm^3 spherical target contrasted from its surroundings by 10:1. The centroid of the target lies in the z-axis and the target depth is measured as the distance from its centroid to the point (0, 0, 5) in breast geometry (Fig. 4.1). The various plots show the affect of varying optical densities (OD) of the excitation light rejection filter. 102
- Fig. 5.1 The true-positive fraction (TPF) of human observer's diagnostic test (based on the visualization of reconstructed images) in a "double-blinded" type setup vs. the strength of endogenous lumps (Number of lumps, $N_p=100$; lump width, $w=0.5\text{ cm}$). The fluorescent target is a 1 cc spherical volume randomly located at depths of 2 cm or less, and is contrasted from its surroundings by 50:1. A total of 40 simulated patients, as shown in Table 5.1, were considered for each lump strength value. 124

- Fig. 5.2 The true-positive fraction (*TPF*) of human observer's diagnostic test (based on the visualization of reconstructed images) in a "double-blinded" type setup vs. the strength of endogenous as well as exogenous lumps (Number of lumps, $N_p=50$; lump width, $w=0.5\text{ cm}$). The fluorescent target is a 1 cc spherical volume randomly located at depths of 2.5 cm or less, and is contrasted from its surroundings by 50:1. A total of 30 simulated patients, as shown in Table 5.2, were considered for each lump strength value..... 124
- Fig. C.1 SNR_{Hot} computed from simulated measurements of intensity, I_{AC} , in one hundred percent lumpy backgrounds of endogenous as well as exogenous optical properties vs. the number of imaging data sets, N . The centroid of the target lies in the z-axis and it is contrasted from its surroundings by 10:1. One twenty eight point detectors (as shown in Fig. 4.2) are used for the collection of light and only one source is lighted such that the measurement data set is a vector of 128×1 157

1. INTRODUCTION

1.1 Motivation

Molecular imaging has progressed significantly since the early literature promised its potential for disease diagnostic abilities.¹⁻⁴ Novel approaches to molecular imaging are being devised in order to reshape the diagnosis and treatment of cancer. Since the detection and localization of metastatic lesions have been proved stubbornly resistant to the conventional imaging techniques, newer molecular approaches are mainly focused to overcome this issue. Currently, the “gold standard” for clinical molecular imaging is mainly based upon the nuclear techniques of gamma scintigraphy, positron emission tomography (PET), and single photon emission computed tomography (SPECT).^{5, 6} Unlike nuclear imaging techniques, in which radiotracers release a single photon imaging event upon relaxation and cannot be reactivated in tissues, *fluorescence-enhanced optical imaging* has higher signal-to-noise ratio (SNR) owing to the ability of a fluorophore to be repeatedly excited.⁷ In addition, fluorophores do not have an intrinsic half-life as do radiopharmaceuticals. This greatly enhances the duration of time for imaging, which is limited in the case of nuclear imaging, and results in higher target-to-background ratios (TBR). Despite these advantages and the fact that its proposed development is ongoing for almost a decade, fluorescence-enhanced optical imaging with new molecular imaging agents has yet to progress into clinical studies on actual cancer patients. One reason for this might be associated to the fact that the

This dissertation follows the style of Optics Express.

administration of molecularly targeted fluorescent contrast agents (fluorophores) do not have a proven record of safety and efficacy and consequently represent an unknown risk to patients. Yet in order to demonstrate the effectiveness of fluorescence imaging for cancer diagnostics, a large number of patient studies need to be performed to gather the appropriate statistics. Hence there is a need to find an alternative approach through which fluorescence imaging systems can be assessed without injecting these contrast agents in cancer patients. Experimental studies on tissue mimicking phantoms⁸⁻¹⁰ and simulation studies using synthetic measurements¹¹ are the approaches that earlier workers have adopted as reliable alternatives. But these studies have focused on detecting a fluorescent target in the presence of a homogeneous background. The studies involving homogeneous backgrounds are important, but more or less irrelevant since in reality the tissue heterogeneity is almost always present in a structured anatomical background, which changes from patient to patient. For molecularly targeting agents, heterogeneous distribution of the disease markers may be unevenly expressed at a lower level than in the target tissue. Furthermore, the background variability could have a substantial effect on an observer's detection performance and thus can not be ignored.^{12, 13}

Additionally, the popularity and credibility of nuclear techniques for the diagnostic medical imaging can be ascribed to the established tools for the objective assessment of image quality (OAIQ).¹⁴⁻¹⁶ These tools aid in the imaging equipment development, performance specification, comparison of different imaging systems, and the imaging technique optimization. More importantly, they can be used to improve the

diagnostic ability of medical imaging systems. Since fluorescence-enhanced optical tomography is a highly nonlinear inverse problem, OAIQ tools may not be directly applicable. In the past, the evaluation of optical tomography systems mainly consisted of contrast-detail analysis^{17, 18} (minimum contrast level for detection and characterization) and statistical analysis^{8, 11, 19, 20} (mean square error, image standard deviation, etc) as reported in Table 1.1. Although measures of contrast-detail and statistical analyses are important to test the feasibility of the fluorescence imaging, OAIQ tools are needed to aid in the optimization of instrumentation as well as the imaging algorithms for detection (is there a tumor present or not?) and estimation (what is the location or size of the tumor?) tasks. In this context, the OAIQ tools are intended to be an aid in the understanding of the limitations of fluorescence-enhanced optical imaging technology for appropriate clinical application without exposing patients to unknown risks. To our knowledge, there has been no attempt to assess the fluorescence-enhanced optical imaging systems using OAIQ tools until now. Although Pineda and Arridge²¹ used these tools for *time domain* optical tomography, their system, a 2D disc phantom, lacks a realistic description of a patient's anatomy. Besides, they use a diffuse optical tomography approach to image the endogenous optical properties in a 2D medium, which is in contrast to our study that involves an exogenous fluorescent imaging agent. In this contribution we propose the employment of (i) a model to simulate the natural tissue structure, and (ii) the OAIQ tools to assess the *detection* task of the fluorescence-enhanced imaging. The main goals of this dissertation will be to develop and use OAIQ tools to evaluate fluorescence imaging for clinical studies.

Table 1.1 Review of the literature for the image quality assessment approaches in near-infrared (NIR) diffusion optical imaging.

Authors	Imaging modality	Measurement	Image reconstruction technique	Image quality assessment tools	Comments
Pogue <i>et al.</i> (2000) ¹⁷	Diffuse optical tomography, DOT (no fluorescence)	Epoxy resin phantoms to mimic optical properties of human breast; 16 point sources and 16 detector fibers.	Newton-Raphson method with Levenberg-Marquardt regularization (finite element based) 2D	Contrast-detail analysis (minimum contrast level for detection and characterization)	It is not possible for such nonlinear modalities to arrive at a single number which can provide the resolution limit achievable for such nonlinear imaging modalities.
Roy <i>et al.</i> (2001) ¹¹	DOT (fluorescence-enhanced)	Synthetic measurements on a frustum-shaped phantom; 43 source nodes and 42 detector nodes on the curved surface.	Truncated Newton method with trust regions (finite element based) 3D	Statistical analysis (sum of square errors, mean of relative error, standard deviation)	The statistical quantities on the left column are used to determine the convergence criteria for the inverse imaging algorithm.
Pogue <i>et al.</i> (2002) ²⁰	DOT (no fluorescence)	100 repeated reconstruction of a simulated 2D test image with randomly distributed noise added.	Newton-Raphson method with Levenberg-Marquardt regularization (finite element based) 2D	Statistical analysis (mean square error, MSE, over the image, image bias, image variance)	1. Bias error dominates at high regularization parameter values while variance dominates as the near the optimal solution. 2. In order to achieve a minimum MSE in the overall image with an increment in measurement noise, higher values of regularization parameters were needed.
Song <i>et al.</i> (2002) ¹⁹	DOT (no fluorescence)	Gelatin phantoms to mimic optical properties of human breast; 16 point sources (15 detector fibers for each).	Newton-Raphson method with Levenberg-Marquardt regularization (finite element based) 2D	Statistical analysis (MSE over the image, image bias, image variance)	1. Imaging performance is not limited by random measurement error, but rather by calibration issues. 2. The minimization of the objective function is not always correlated with an overall image error decrease.

Table 1.1 Continued

Authors	Imaging modality	Measurement	Image reconstruction technique	Image quality assessment tools	Comments
Millstein <i>et al.</i> (2003)⁸	DOT (fluorescence-enhanced)	A cubic phantom box filled with Intralipid solution and a spherical heterogeneity (ICG); nine source fibers at the bottom and 14 detector fibers at the top.	Iterative coordinate descent, ICD, algorithm based on Bayesian inversion strategy (finite-difference scheme) 3D	Statistical analysis (weighted average, normalized root mean square error, NRMSE)	1. This method can track even very small changes in diagnostic lifetime imaging applications. 2. For yield reconstructions, the error propagation study suggests that the qualitative results may be obtained by using simplified models rather than the full absorption problem.
Dehgani <i>et al.</i> (2003)²²	DOT (no fluorescence)	A cylindrical phantom filled with Intralipid solution and India ink; three measurement planes each with 16 sources and 16 detectors.	Levenberg-Marquardt algorithm (finite element based) 3D	Resolution studies (peak and full width at half maximum, FWHM)	1. The study of variation in resolution of target with mid-plane and out-of-plane movement. 2. Report improvement in the image reconstruction when using <i>a priori</i> information.
Millstein <i>et al.</i> (2005)²³	DOT (fluorescence-enhanced)	A cylindrical plastic dish filled with solid gel (suspension of 1% Intralipid and agarose); a fluorescently labeled mouse tumor; 1D measurement scans.	A binary hypothesis testing approach for detection; Maximum likelihood approach for localization. 2D	Probability of detection for a given false alarm rate; Cramer-Rao lower bound for localization estimation error.	1. Detection studies are done using a statistical model of the measurement system validated using phantom studies. 2. Actual tomographic reconstructions are not performed and the detection-localization approaches presented are used as its complement.
Gao <i>et al.</i> (2005)¹⁸	DOT (no fluorescence)	Simulated measurements on a 2D circular domain with two target inclusions;	A modified generalized pulse spectrum technique (GPST) 2D	Target size and contrast analysis	1. The GPST is validated using DOT experiments on human lower legs and forearms. 2. The numerical phantoms were devised with reference to the anatomy and MRI images of the lower-leg and forearm.

1.2 Specific aims

The specific aims of the dissertation are listed below:

1. **To employ a model to simulate both natural tissue heterogeneity as well as heterogeneous distribution in a molecularly targeted fluorophore:** The *lumpy-object model* was used to simulate the natural anatomical backgrounds. The object model was employed in a finite element framework suitable for generating imaging data sets in fluorescence imaging.
2. **To validate tomographic imaging algorithm based upon finite elements for repetitious image reconstruction in the presence of simulated heterogeneity:** The finite element based algorithm for fluorescence tomography developed by Dr. Ranadhir Roy was modified to incorporate lumpy-object model. A large, breast-shaped geometry was used in simulation studies. The heterogeneous backgrounds representing the tissue anatomy as well as the uneven fluorophore distribution were introduced using the lumpy-object model. The sensitivity of the imaging algorithm to the simulated tissue heterogeneity in terms of the contrast level was investigated for tumor detection tasks.
3. **To employ the Hotelling observer model to assess imaging data sets generated by the forward predictor in the presence of lumpy backgrounds:** A finite element program was developed to solve the coupled diffusion equations, otherwise

known as the *forward solver*. The assessment of imaging data sets generated by the forward solver in the presence of lumpy backgrounds was performed using an optimal linear observer, the Hotelling observer model. The SNR of the Hotelling observer was analyzed as a function of *background perturbations* and *tumor depth*. The systematic errors and noise associated with the actual experimental conditions were incorporated into the simulated imaging data sets.

4. **To assess the detection performance of a Gauss-Newton based tomographic algorithm for multiple cases of randomly located targets superimposed on random heterogeneous backgrounds:** A Gauss-Newton algorithm was developed for the tomographic problem of fluorescence imaging. The finite element based forward solver developed for Hotelling observer studies was employed in the algorithm for Gauss-Newton updates. The algorithm was implemented in Matlab (The Mathworks, Inc., Natick, MA) platform. The targets were placed randomly inside the breast-shaped geometry with heterogeneous backgrounds simulated by lumpy-object model. The human observer performing the detection task had no prior knowledge of either the location of the target or the background structure.

1.3 Organization of dissertation

The organization of this dissertation is presented in Fig. 1.1 below.

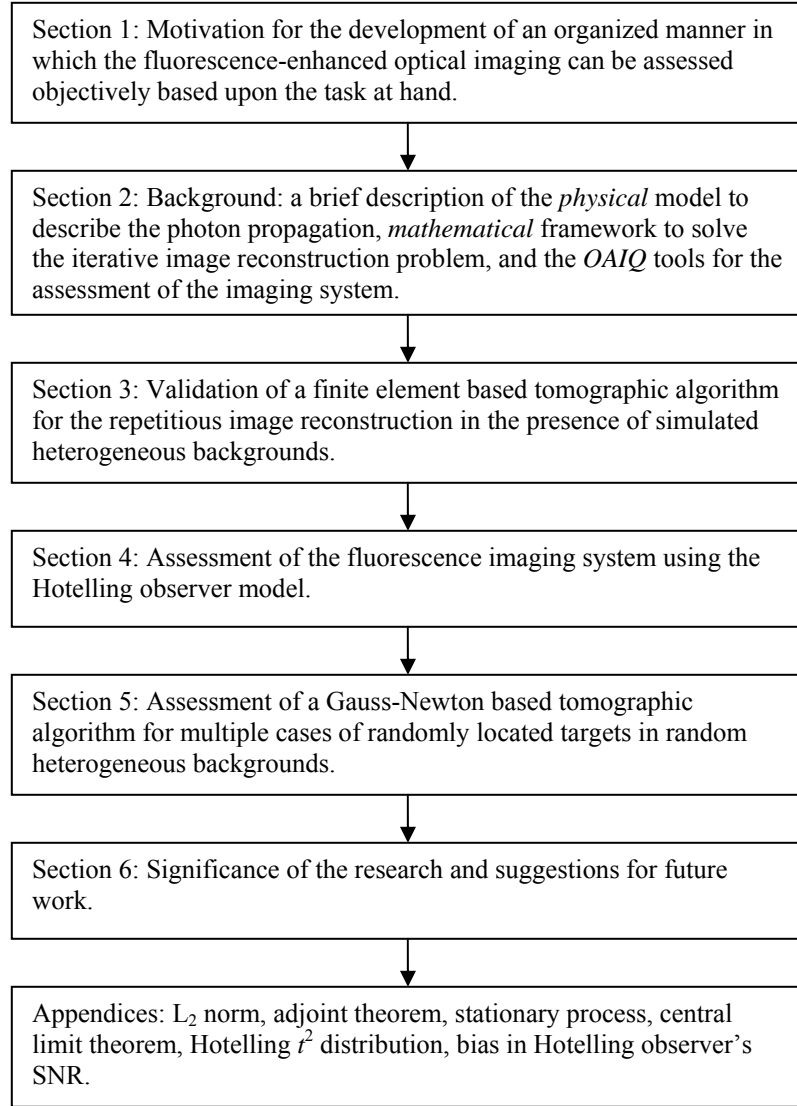


Fig 1.1 Organization of the dissertation.

2. BACKGROUND

2.1 Fluorescence photon migration

Near-infrared (NIR) light within the 750-900 nm wavelength range can penetrate deep into the biological tissues because in this range, the absorption of photons by hemoglobin, water, and fat is least. Consequently photons can travel several centimeters inside the tissue undergoing multiple scattering. This is why the NIR light is essential for probing the molecular activity at a depth of more than few millimeters. Fluorescence-enhanced optical imaging uses NIR light and a fluorophore (a fluorescent contrast agent which enhances the optical contrast between normal and diseased tissue) to investigate the exogenous optical properties of the tissue medium such as the absorption coefficient owing to the fluorophore. This, coupled with the fact that tissue autofluorescence is at minimum at NIR wavelengths, further enhances the optical contrast between the normal and diseased tissue and improves detection. Thus, fluorescence imaging provides a way to non-invasively diagnose tissue anomalies since the difference in fluorophore cross section can be used to molecularly locate and characterize the diseased state of the tissue.

The propagation of the NIR photons through the tissue media can be modeled by the Boltzmann radiative transport equation (RTE).²⁴ Although the full RTE is difficult to solve and is computationally intensive, several researchers have used it to model NIR light transport in tissue.^{25, 26} A simplification of the RTE, known as *diffusion approximation*, can be used to model light propagation in an isotropic scattering media

and results in significant computational savings. The assumption here is that after multiple scattering events, photons will travel *almost* equally in all directions. This is known as isotropic propagation and is a valid assumption if photons travel longer than the transport mean free path. Recently, Tarvainen *et al.* have coupled RTE and diffusion approximation approach so that the RTE can be employed in subdomains where diffusion approximation is not valid.^{27, 28} In our system, the diffusion approximation to the RTE works well and has been employed as a physical model for light propagation. The photon diffusion equation in its most general form can be written as:

$$\frac{1}{c} \frac{\partial \Phi(\mathbf{r}, t)}{\partial t} - \nabla \cdot [D(\mathbf{r}) \nabla \Phi(\mathbf{r}, t)] + \mu_a(\mathbf{r}) \Phi(\mathbf{r}, t) = S(\mathbf{r}, t) \quad (2.1)$$

Here $\Phi(\mathbf{r}, t)$ is the photon fluence rate (*photons/(cm²s)*) at position \mathbf{r} and time t ; D is the photon diffusion coefficient (*cm*); μ_a is the absorption coefficient (*cm⁻¹*); $S(\mathbf{r}, t)$ is the photon source strength (*photons/(cm³s)*) at position \mathbf{r} and time t ; c is the speed of light in the medium. In frequency domain photon migration (FDPM), a sinusoidal intensity modulated NIR light is used as a source and the diffusion equation is given by the Fourier transform of the above Eq. (2.1):

$$\frac{i\omega}{c} \Phi(\mathbf{r}, \omega) - \nabla \cdot [D(\mathbf{r}) \nabla \Phi(\mathbf{r}, \omega)] + \mu_a(\mathbf{r}) \Phi(\mathbf{r}, \omega) = S(\mathbf{r}, \omega) \quad (2.2)$$

Here ω is the modulation frequency of the NIR source (*rad/s*). The above equation (2.2) has been used by researchers in optical tomographic problems using endogenous contrast (i.e. due to the uneven absorption of photons) between normal and diseased tissue.^{19, 29} But in reality the endogenous optical contrast between healthy and diseased tissue might not be sufficient for the detection and this necessitates the use of exogenous

contrast agents (fluorophores). Exogenous fluorophores are introduced into the tissue for molecular targeting to a specific tissue region, such as the tumor. When NIR light reaches a fluorophore molecule bonded to some tissue site, the fluorophore excites and thus fluoresces (Fig. 2.1). When this excited fluorophore molecule releases its energy and comes to ground state, fluorescence emission occurs (see Jablonski diagram in Fig. 2.2). The fluorescent quantum yield, ϕ , of this process is given by the ratio of number of photons emitted to the number of photons absorbed. Mathematically it can be represented by:

$$\phi = \frac{\Gamma}{\Gamma + K_{nr}} \quad (2.3)$$

Where Γ is the first order rate constant for radiative relaxation and K_{nr} is the rate constant for non-radiative relaxation. Similarly, the fluorophore lifetime, τ (typically of the order of nanoseconds,) is the average time a fluorophore molecule spends in its excited state and mathematically can be given by:

$$\tau = \frac{1}{\Gamma + K_{nr}} \quad (2.4)$$

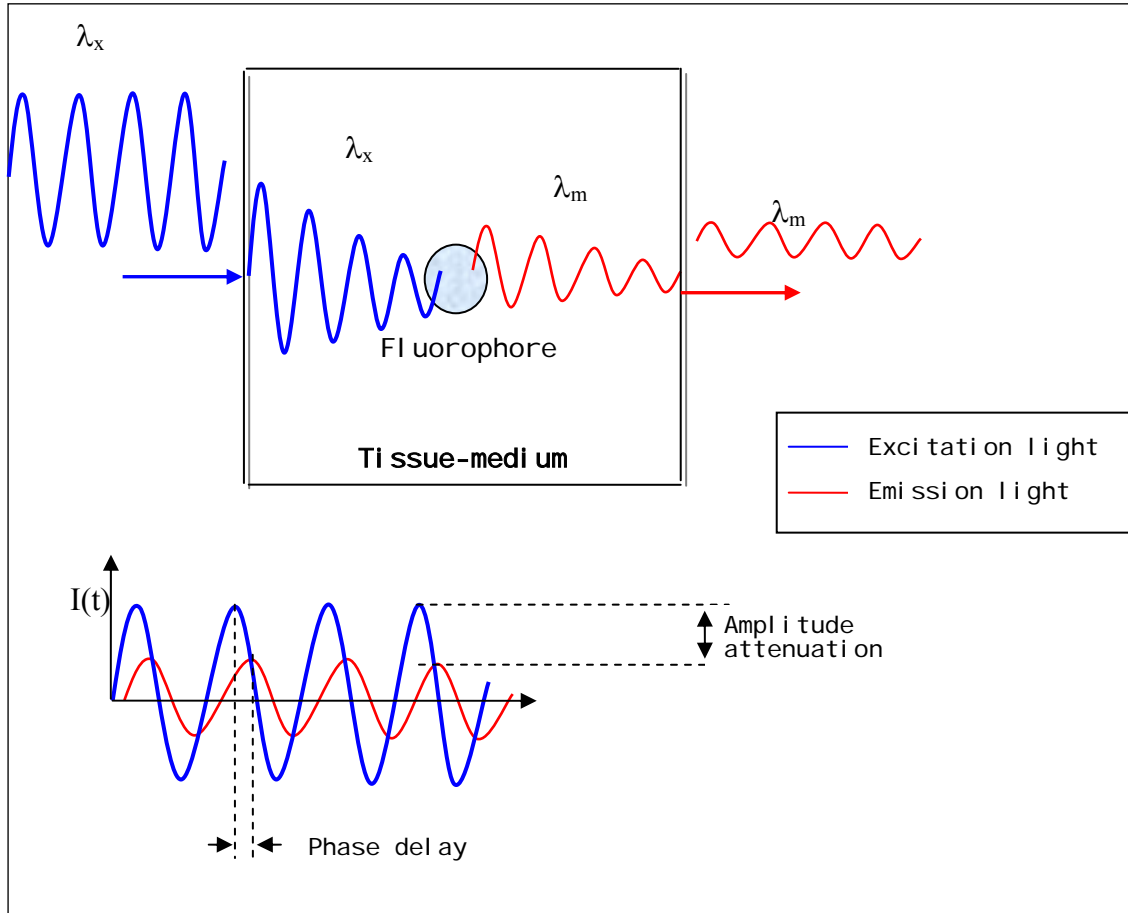


Fig. 2.1 Illustration of the frequency domain photon migration. Intensity modulated photon density wave of wavelength λ_x is launched into the system, which propagates and encounters a fluorophore molecule, giving rise to fluorescent emission wave of wavelength λ_m .

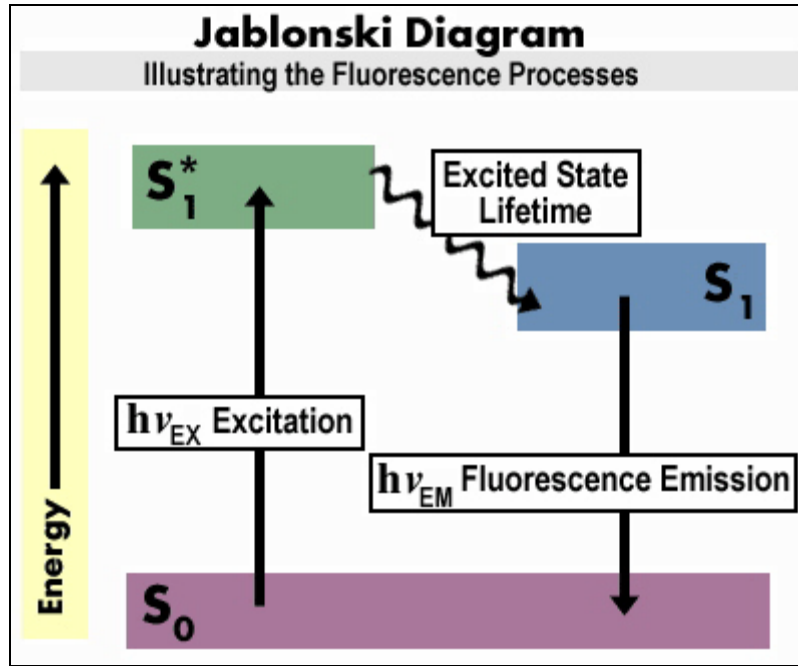


Fig. 2.2 Jablonski diagram showing that the excited photon relaxes radiatively while emitting the fluorescence light. Various **S** denote the singlet electronic states of the fluorophore molecule. http://laxmi.nuc.ucla.edu:8248/M248_98/synprob/part1/prop_fprob.html.

The generation and propagation of the fluorescence diffuse photon density waves can be described by the following coupled diffusion equations:^{30, 31}

$$-\nabla \cdot [D_x(\mathbf{r}) \nabla \Phi_x(\mathbf{r}, \omega)] + \left[\frac{i\omega}{c} + \mu_{axi}(\mathbf{r}) + \mu_{axf}(\mathbf{r}) \right] \Phi_x(\mathbf{r}, \omega) = S(\mathbf{r}, \omega) \quad (2.5)$$

$$\begin{aligned} -\nabla \cdot [D_m(\mathbf{r}) \nabla \Phi_m(\mathbf{r}, \omega)] + \left[\frac{i\omega}{c} + \mu_{ami}(\mathbf{r}) + \mu_{amf}(\mathbf{r}) \right] \Phi_m(\mathbf{r}, \omega) \\ = \phi \mu_{axf}(\mathbf{r}) \frac{1}{1 + i\omega\tau} \Phi_x(\mathbf{r}, \omega) \end{aligned} \quad (2.6)$$

Where the subscript x denotes excitation and m denotes emission*. The term $\mu_{ax,mi}$ is the absorption due to endogenous chromophores; $\mu_{ax,mf}$ is the absorption due to the exogenous fluorophores. The diffusion coefficient is given by:

$$D_{x,m} = \frac{1}{3(\mu_{ax,mi} + \mu_{ax,mf} + \mu_{sx,m}(1-g))} \quad (2.7)$$

Where $\mu_{sx,m}$ is the scattering coefficient and g is the coefficient of anisotropy of the medium. The coefficient g is defined as the average cosine of the scattering angle, and varies from 0 (for an isotropic medium) to 1 (for a forward scattering medium). For biological tissues, the typical value of g is greater than or equal to 0.9. The coupled diffusion equations (2.5) and (2.6) can be solved employing one of the boundary conditions described in Section 2.1.1 to yield,

$$\Phi_{x,m}(\mathbf{r}, \omega) \propto I_{AC_{x,m}} \exp(-i\theta_{x,m}(\mathbf{r}, \omega)) \quad (2.8)$$

Here $\Phi_{x,m}$ is a complex number; $\theta_{x,m}$ are the measured phase lags and $I_{AC_{x,m}}$ are the amplitudes of the photon density wave at excitation/emission wavelengths. The description of the finite element method (FEM) to solve the coupled diffusion equations (2.5) and (2.6) is given in the Section 2.2.1.

* Subscript x,m denotes two quantities, one with subscript x and the other with subscript m . For example, $a_{x,m}+b_{x,m}=0$ actually is a set of the following two equations: $a_x+b_x=0$; $a_m+b_m=0$.

2.1.1 Boundary conditions

The most common types of boundary conditions to represent a tissue boundary (see Fig. 2.3) are: (a) zero-boundary condition (Dirichlet type), (b) partial current boundary condition (Robin type), and (c) extrapolated boundary condition.

(a) Zero-boundary condition (ZBC)

Dirichlet boundary condition is often referred to as *first-type* boundary condition in mathematical terminology and specifies the *value* a solution takes on the boundary of the domain. In the context of fluorescence photon migration, the zero-boundary condition imposes the fluence Φ to be zero on and outside the boundary:

$$\Phi_{x,m}(\mathbf{r}, \omega) = 0 \Big|_{z=0}. \quad (2.9)$$

Although zero fluence boundary condition is unphysical and violates the diffusion approximation, it is mathematically simple to implement and researchers have advocated that it is a good approximation of the biological tissues.³²

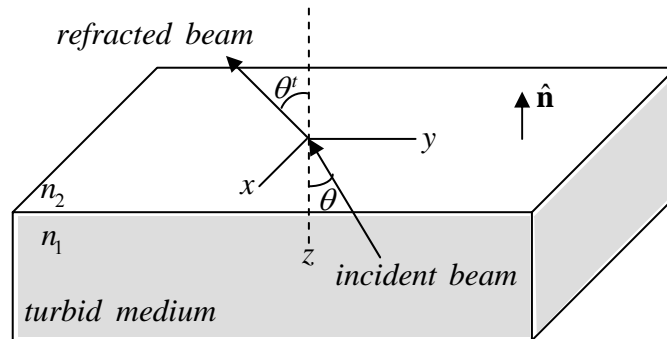


Fig. 2.3 Boundary surface of the strongly scattering turbid medium. The turbid medium and the outside have refractive indices of n_1 and n_2 respectively. $\hat{\mathbf{n}}$ is the outward drawn normal to the surface of the boundary.

(b) Partial current boundary condition (PCB)

The Robin boundary condition is often referred to as the *third-type* boundary condition and specifies a *value* that a linear combination of the solution variable and its normal derivative takes on the boundary. In the context of fluorescence photon migration, the partial current boundary condition is a sound representation of physics and signifies that the photons leaving the tissue surface never return and are governed by the Fresnel reflection at the tissue-outside interface:³²⁻³⁴

$$2D_{x,m} \frac{\partial \Phi_{x,m}}{\partial n} + \gamma \Phi_{x,m} = 0. \quad (2.10)$$

Where n denotes the outward normal to the surface; and γ is the constant depending upon the optical refractive index mismatch at the boundary. γ is a function of the effective refractive index (R_{eff}):

$$\gamma = \left(\frac{1 + R_{eff}}{1 - R_{eff}} \right). \quad (2.11)$$

R_{eff} can be determined from the Fresnel's reflections, R_j and R_ϕ , according to:

$$R_{eff} = \left(\frac{1 + R_j}{1 + R_\phi} \right). \quad (2.12)$$

Where

$$R_j = \int_0^{\pi/2} 2 \sin \theta \cos \theta R_{Fresnel}(\theta) d\theta, \quad (2.13)$$

$$R_\phi = \int_0^{\pi/2} 3 \sin \theta \cos^2 \theta R_{Fresnel}(\theta) d\theta, \quad (2.14)$$

and $R_{Fresnel}$ is the Fresnel reflection coefficient, a function of θ , the angle at which the light is incident on the boundary.³²

$$R_{Fresnel}(\theta) = \frac{1}{2} \left(\frac{n_1 \cos \theta' - n_2 \cos \theta}{n_1 \cos \theta' + n_2 \cos \theta} \right)^2 + \frac{1}{2} \left(\frac{n_1 \cos \theta + n_2 \cos \theta'}{n_1 \cos \theta - n_2 \cos \theta'} \right)^2 \quad \text{when } 0 \leq \theta \leq \theta_c \quad (2.15)$$

$$R_{Fresnel}(\theta) = 1 \quad \text{when } \theta_c \leq \theta \leq \pi/2, \quad (2.16)$$

where n_1 and n_2 are the refractive indices of the turbid (tissue) medium and the outside medium, respectively; θ and θ' are the incident angle from within the turbid medium and the refracted angle in the outside medium, respectively, and satisfy Snell's law, $n_1 \sin \theta = n_2 \sin \theta'$. θ_c is the critical angle for the total internal reflection at the tissue/outside boundary. Eq. (2.12) through (2.15) show the dependence of R_{eff} on the relative refractive index, $n_{rel} = n_2 / n_1$.

(c) Extrapolated boundary condition (EBC)

The extrapolated boundary condition uses the concept of a hypothetical boundary at some distance from the tissue-outside interface.³⁴ The location z_b of the hypothetical boundary is obtained by extrapolating the fluence rate into the outside medium with the same slope as at the tissue-outside boundary.³⁴ The fluence is assumed to be zero at the hypothetical boundary in PCB:

$$\Phi_{x,m}(\mathbf{r}, \omega) = 0 \Big|_{z=z_b}. \quad (2.17)$$

It is to be noted that the assumption of zero fluence at the extrapolated boundary does not imply that the fluence is actually zero there, and so PCB is not physical and merely serves as a simplification of the mathematics.

2.2 Fluorescence-enhanced optical tomography

Optical tomography, in general, utilizes light in a specific wavelength range to transilluminate a highly scattering medium (like biological tissues), so that the resulting measurement of light intensity on the boundary of the medium can be used to obtain a spatial map of the optical properties of the medium. Specifically, the fluorescence-enhanced optical tomography uses intensity modulated NIR light (typically modulated at 100 MHz) to activate fluorophores present in the medium, resulting in the boundary measurements of the amplitude as well as the phase of the emission light. Consequently, the boundary measurements are used along with the coupled diffusion equations to reconstruct the spatial distribution of the optical properties of the medium, with the help of analytical or numerical techniques.

Fluorescence-enhanced optical tomography typically involves two steps: (i) to solve the coupled diffusion equations for the boundary values of the emission fluence with an assumption that the spatial map of the optical properties of the medium is known (*the forward problem*); and (ii) to find the spatial map of the optical properties of the medium corresponding to minimum difference between the experimental boundary measurements and the measurements predicted by the forward model (*the inverse problem*). The solution approaches to the inverse problem are often referred to as the *image reconstruction techniques*, probably since the map (image) of the interior optical properties is the main objective in solving the inverse problem. By nature, the tomography problem is an iterative process in which the measurements resulting from an initial guess of optical properties are compared with the experimental measurements in

an optimization framework to obtain a subsequent guess. The process is continued until some specific convergence criterion is met. Usually if the difference between the experimental measurements and the forward model predictions is less than a tolerance value, the iterative process is stopped.

The following sections describe the approaches to solve the forward and the inverse problem in fluorescence-enhanced optical imaging. Specifically, the finite element representation of the forward problem is described in Section 2.2.1; and the optimization approaches to solve the inverse problem are described in Section 2.2.2.

2.2.1 Modeling photon transport (forward problem)

In the context of this dissertation, the forward problem refers to solving coupled diffusion equations (2.5) and (2.6) simultaneously for Φ_x and Φ_m employing one of the boundary conditions in Section 2.1.1 with the assumption that the interior optical property map (spatial values of $\mu_{ax,mi}$, $\mu_{ax,mf}$, and $\mu_{sx,m}$) of the tissue or phantom medium is known.

Finite difference (FD) and the finite element methods are two most common numerical techniques to solve a system of partial differential equations. Unlike FD methods, using finite elements has many advantages, including: (i) problems can be solved on complex irregular regions; (ii) the domain can be discretized into nonuniform meshes to account for the solution gradients; and (iii) easier handling of the unusual specification of boundary conditions, such as boundary conditions involving fluxes. Therefore, we have employed a Galerkin-type finite element scheme to solve the

coupled diffusion equations in this work.^{35, 36} The various steps involved in the development of a finite element model and, subsequently, in the prediction of solutions are described below.

Step 1: Discretization

As a first step, the given domain is discretized into a collection of finite elements. We prefer tetrahedral elements to discretize the solution domain due to their good adaptability to complicated geometries. The meshing of the solution domain can be performed using GAMBIT[®] (Fluent Inc., Lebanon, NH) software, which outputs the numbering of nodes and elements along with the nodal connectivity information as text files.

Step 2: Construction of weak form

In finite difference techniques, the derivatives are approximated by finite differences with respect to the mesh introduced in the domain. With the finite element method, the *method of weighted residuals* is applied to construct an integral formulation of the coupled diffusion equations called a *variational problem*. The formulation for the excitation wave diffusion equation, Eq. (2.5), is described in detail here, and a similar methodology is adopted for the emission wave diffusion equation, Eq. (2.6). Accordingly, Eq. (2.5) is multiplied by a *weight function*, w , and integrated over the solution domain, Ω :

$$\int_{\Omega} \left(-\nabla \cdot [D_x \nabla \Phi_x] + \left[\frac{i\omega}{c} + \mu_{axi} + \mu_{axf} \right] \Phi_x \right) w d\Omega = \int_{\Omega} S w d\Omega. \quad (2.18)$$

Using the chain rule,

$$\nabla \cdot (w \nabla \Phi_x) = (\nabla w) \cdot (\nabla \Phi_x) + w (\nabla^2 \Phi_x), \quad (2.19)$$

the above Eq. (2.18) becomes

$$\int_{\Omega} \left(D_x \nabla w \cdot \nabla \Phi_x - D_x \nabla \cdot (w \nabla \Phi_x) + \left[\frac{i\omega}{c} + \mu_{axi} + \mu_{axf} \right] \Phi_x w \right) d\Omega = \int_{\Omega} S w d\Omega. \quad (2.20)$$

According to the divergence theorem

$$\int_{\Omega} (\nabla \cdot \mathbf{p}) d\Omega = \oint_{\Gamma} \mathbf{p} \cdot \hat{\mathbf{n}} d\Gamma, \quad (2.21)$$

where \mathbf{p} is a dummy vector; Γ denotes the surface of the volume Ω ; and $\hat{\mathbf{n}}$ is the unit vector in the direction normal to the surface Γ . Applying gradient theorem in Eq. (2.20) yields

$$\int_{\Omega} \left(D_x \nabla w \cdot \nabla \Phi_x + \left[\frac{i\omega}{c} + \mu_{axi} + \mu_{axf} \right] \Phi_x w \right) d\Omega - \oint_{\Gamma} D_x (w \nabla \Phi_x) \cdot \hat{\mathbf{n}} d\Gamma = \int_{\Omega} S w d\Omega. \quad (2.22)$$

The above Eq. (2.22) is called the *weak* (or *variational*) form of Eq. (2.5).

Step 3: Deriving interpolation functions

In finite element approach, an approximate solution to the Eq. (2.5) is sought over each tetrahedral finite element (see Fig. 2.3). Thus, the solution, Φ_x^e , within a typical tetrahedral element Ω^e is given by the following polynomial approximation:

$$\Phi_x^e = \sum_{j=1}^{N^e} \Phi_{xj}^e \psi_j^e(\mathbf{r}), \quad (2.23)$$

where Φ_{xj}^e are the solution values at node j of the tetrahedral element Ω^e ; $\psi_j^e(\mathbf{r})$ are the *interpolation functions*; and N^e is the number of nodes in element Ω^e ($N^e=4$ since a tetrahedron has four vertices). In order for the approximate solution, Φ_x^e , to have a tendency to converge to the actual solution for higher discretization levels, the interpolation functions should be chosen such that the approximate solution, Φ_x^e , satisfies following conditions:^{35, 36} (i) it must be continuous over the element, and at least once differentiable, as required by the weak form; (ii) it should be a *complete* polynomial; and (iii) all terms in the polynomial should be linearly independent.

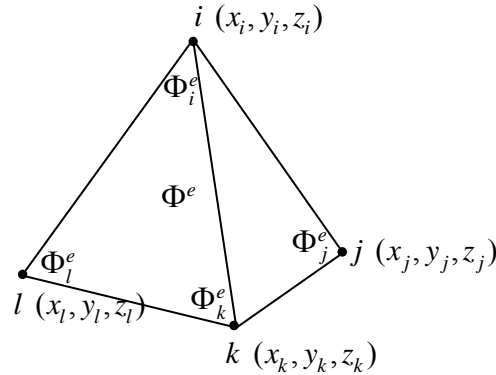


Fig. 2.3 A tetrahedral element ‘ e ’ with nodes ‘ i ’, ‘ j ’, ‘ k ’, and ‘ l ’. In finite element method, a given domain is discretized into elements such as this one. First, the solution is sought over each such individual element, and then the overall solution is obtained by combining the elemental solutions.

For the variational problem of Eq. (2.22), the minimum polynomial order is linear. A complete linear polynomial is of the form

$$\Phi_x^e = a + \mathbf{b} \cdot \mathbf{r} = a + b_1 x + b_2 y + b_3 z, \quad (2.24)$$

and it satisfies all of the above three conditions. By definition, the above expression should satisfy

$$\Phi_{xj}^e = a + b_1 x_j^e + b_2 y_j^e + b_3 z_j^e, \quad j = 1, 2, 3, 4 \quad (2.25)$$

i.e. it should yield the solution value at the node when provided with the nodal coordinates. Equations (2.25) are solved for $[a, b_1, b_2, b_3]$ in terms of Φ_{xj}^e s, and the resulting expressions for $[a, b_1, b_2, b_3]$ are used in Eq. (2.24), and are subsequently compared with Eq. (2.23) to obtain the expressions of interpolation functions $\psi_j^e(\mathbf{r})$.

Step 4: Developing finite element model using weak form

In the Galerkin scheme, the weight functions are restricted to the solution space, and so

$$w = \psi_j^e, \quad j = 1, 2, 3, 4 \quad (2.26)$$

are taken as the weight functions for the element Ω^e . Equations (2.23) and (2.26) are used along with the weak form given in Eq. (2.22) for element Ω^e , to obtain

$$\begin{aligned} & \int_{\Omega^e} \left(D_x^e \nabla \psi_i^e \cdot \left(\sum_{j=1}^4 \Phi_{xj}^e \nabla \psi_j^e \right) + \left[\frac{i\omega}{c} + \mu_{axi}^e + \mu_{axf}^e \right] \psi_i^e \sum_{j=1}^4 \Phi_{xj}^e \psi_j^e \right) d\Omega^e - \oint_{\Gamma^e} D_x^e (\psi_i^e \nabla \Phi_x) \cdot \hat{\mathbf{n}} d\Gamma^e \\ & = \int_{\Omega^e} S \psi_i^e d\Omega^e, \quad i = 1, 2, 3, 4 \end{aligned} \quad (2.27)$$

where D_x^e denotes the average value of the diffusion coefficient, D_x , over the element Ω^e , etc. The above is a system of four equations with four unknowns as the nodal values of solution Φ_x^e , and thus can be solved for Φ_{xj}^e s for a given optical property map $(\mu_{axi}^e, \mu_{axf}^e, D_x^e)$. Alternatively, Eq. (2.27) can be written as:

$$\sum_{j=1}^4 (\mathbf{K}_x^e)_{ij} \Phi_{xj}^e = (\mathbf{S}_x^e)_i, \quad i = 1, 2, 3, 4 \quad (2.28)$$

or simply represented as matrix multiplication:

$$\mathbf{K}_x^e \Phi_x^e = \mathbf{S}_x^e, \quad (2.29)$$

such that

$$\begin{aligned} (\mathbf{K}_x^e)_{ij} = & \int_{\Omega^e} \left(D_x^e \nabla \psi_i^e \cdot \left(\sum_{j=1}^4 \Phi_{xj}^e \nabla \psi_j^e \right) + \left[\frac{i\omega}{c} + \mu_{axi}^e + \mu_{axf}^e \right] \psi_i^e \sum_{j=1}^4 \Phi_{xj}^e \psi_j^e \right) d\Omega^e \\ & - \oint_{\Gamma^e} D_x^e (\psi_i^e \nabla \Phi_x^e) \cdot \hat{\mathbf{n}} d\Gamma^e, \end{aligned} \quad (2.30)$$

$$(\mathbf{S}_x^e)_i = \int_{\Omega^e} S \psi_i^e d\Omega^e. \quad (2.31)$$

In the above expression, \mathbf{K}_x^e is called the *overall elemental stiffness* matrix; and \mathbf{S}_x^e the *local source* matrix.

Step 5: Imposing the boundary conditions

As described in Section 2.1.1, a Robin type boundary condition is employed.

Accordingly, the Eq. (2.10) for the excitation wavelength can be written as:

$$2D_x^e \frac{\partial \Phi_x^e}{\partial n} + \gamma \Phi_x^e = 0, \quad (2.32)$$

which can be rearranged to give:

$$D_x^e \frac{\partial \Phi_x^e}{\partial n} = D_x^e \nabla \Phi_x^e \cdot \hat{\mathbf{n}} = -\frac{\gamma}{2} \Phi_x^e. \quad (2.33)$$

Equation (2.33) is used in Eq. (2.30) to impose the boundary conditions and the elemental stiffness (\mathbf{K}_x^e) and local source (\mathbf{S}_x^e) matrices for all the constituent elements of the domain is evaluated.

Step 6: Assembling global matrices

After performing the matrix evaluations for each individual element, a global stiffness matrix, \mathbf{K}_x , and a global source matrix, \mathbf{S}_x , is assembled by combining elemental stiffness matrices, \mathbf{K}_x^e , and local source matrices, \mathbf{S}_x^e , of all the constituent elements of the domain. As a result, the forward problem of solving Eq. (2.5) for excitation fluence, Φ_x , reduces to solving the following system of equations:

$$\mathbf{K}_x \Phi_x = \mathbf{S}_x. \quad (2.34)$$

The system of equations similar to the Eq. (2.34) is also assembled for the emission wave diffusion equation in Eq. (2.6). The procedure described in the above steps is followed for the forward problem of solving Eq. (2.6) for emission fluence, Φ_m , and the following system of equations is obtained:

$$\mathbf{K}_m \Phi_m = \mathbf{B}_{x \rightarrow m} \Phi_x, \quad (2.35)$$

where \mathbf{K}_m has same expression as \mathbf{K}_x but with all subscripts 'x' replaced by 'm' to represent emission wavelength. $\mathbf{B}_{x \rightarrow m}$ is the coupling matrix due to the coupling term, $\phi\mu_{axf}/(1+i\omega\tau)$, in Eq. (2.6) and its elemental counterpart is given by:

$$(\mathbf{B}_{x \rightarrow m}^e)_{ij} = \int_{\Omega^e} \left(\frac{\phi\mu_{axf}^e}{1+i\omega\tau} \psi_i^e \psi_j^e \right) d\Omega^e. \quad (2.36)$$

Step 7: Solving the system of equations

In order to get the solutions of forward problem using finite elements, the system of linear equations in (2.34) and (2.35) are solved for vectors Φ_x and Φ_m containing the nodal values of the excitation and emission fluence, respectively. A Gaussian elimination method is followed in this work to solve the system of equations.

As illustrated in steps 1 thorough 7, the Galerkin method converts a differential equation to a linear system of equations by restricting the possible solutions and weight functions to a smaller finite space. This is the central idea of the Galerkin method and it inherently seeks an approximation of the real solution; the approximation being more acceptable, the higher the level of discretization. In this work, we have used reasonable meshing size to generate satisfactory solutions to the coupled diffusion equations.

2.2.2 Image reconstruction (inverse problem)

In the context of our research, the inverse problem involves the estimation of the fluorophore activity inside the 3D medium from the photon density wave measurements made at the surface. Therefore, the absorption coefficient due to the fluorophores, $\mu_{ax,mf}$, is the unknown to be estimated spatially inside the 3D medium using the image reconstruction techniques.

The tomographic problem of estimating spatial map of $\mu_{ax,mf}$ is formulated in an optimization framework where the spatial distribution of the optical property, $\mu_{ax,mf}$, corresponding to the minimum difference between the experimental boundary

measurements and the measurements predicted by the forward solver is found. The boundary measurements can be Φ_x , Φ_m , or both, depending upon the imaging system requirements. The formulation of optimization problem for Φ_m as the boundary measurements and μ_{axf} as the unknown optical property is described in this section. A similar methodology is adopted to solve the inverse problem for systems involving different boundary measurements.

The tomography problem can be represented as:

$$\min_{\mu_{axf}} E_{\Phi_m}, \quad (2.37)$$

where E_{Φ_m} is the error (mismatch) between the experimentally *measured* fluence, Φ_m^{meas} , and the one *calculated* using forward problem, Φ_m^{calc} . It is to be noted that Φ_m^{meas} and Φ_m^{calc} are the vectors containing the fluence values at only the detector points of the surface where the measurements are made. If $[r]$ is the residual vector defined as:

$$[r] = \Phi_m^{calc} - \Phi_m^{meas}, \quad (2.38)$$

then E_{Φ_m} can be written as:

$$E_{\Phi_m} = \frac{1}{2} [r]^* [r], \quad (2.39)$$

where superscript * denotes the conjugate transpose of the vector. Equations (2.37) and (2.39) signify that the tomographic problem is reduced to the problem of minimization in a least-square sense. Optimization methods to solve the minimization problem in Eq. (2.37) are discussed in the following sections.

2.2.2.1 Newton method

In all iterative optimization schemes, an initial guess of the optimization variables (μ_{axf}) is made. At each subsequent iteration, an objective function (E_{Φ_m}) is evaluated and the next set of optimization variable values is constructed according to the optimization algorithm. This process stops when a specific optimization stopping criterion is met.

In the Newton method, the error function E_{Φ_m} is first approximated using Taylor's series expansion in μ_{axf} truncated after the quadratic term:

$$\begin{aligned} E_{\Phi_m}(\mu_{axf} + h) &\cong E_{\Phi_m}(\mu_{axf}) + \nabla E_{\Phi_m}(\mu_{axf})h + \frac{1}{2}h \nabla^2 E_{\Phi_m}(\mu_{axf})h^* \\ &= E_{\Phi_m}(\mu_{axf}) + \mathbf{J}_{E_{\Phi_m}} h + \frac{1}{2}h \mathbf{H}_{E_{\Phi_m}} h^*, \end{aligned} \quad (2.40)$$

where $\mathbf{J}_{E_{\Phi_m}}$ is the Jacobian matrix of the error function; and $\mathbf{H}_{E_{\Phi_m}}$ is the Hessian matrix of the error function. In order to minimize the error function in Eq. (2.40), the first order necessary condition of a null gradient is then applied,

$$\begin{aligned} \frac{\partial E_{\Phi_m}(\mu_{axf} + h)}{\partial h} &= \mathbf{J}_{E_{\Phi_m}} + \mathbf{H}_{E_{\Phi_m}} h = \mathbf{0} \\ \Rightarrow h &= -(\mathbf{H}_{E_{\Phi_m}})^{-1} \mathbf{J}_{E_{\Phi_m}}. \end{aligned} \quad (2.41)$$

Here h provides a descent direction for the subsequent Newton step. So the iterative optimization scheme for Newton method is

$$(\mu_{axf})_{k+1} = (\mu_{axf})_k - (\mathbf{H}_{E_{\Phi_m}})^{-1} \mathbf{J}_{E_{\Phi_m}}, \quad (2.42)$$

where the subscript k denotes the iteration number; and the matrices $\mathbf{J}_{E_{\Phi_m}}$ and $\mathbf{H}_{E_{\Phi_m}}$ are evaluated with $(\mu_{axf})_k$. The Hessian matrix in Eq. (2.42) is not explicitly inverted, instead the system of linear equations

$$\mathbf{H}_{E_{\Phi_m}} d_k = -\mathbf{J}_{E_{\Phi_m}}, \quad (2.43)$$

is solved for d_k and the next iterate is taken as

$$(\mu_{axf})_{k+1} = (\mu_{axf})_k + d_k. \quad (2.44)$$

The system of equations in Eq. (2.43) is called Newton equations; and the above Eq. (2.44) is the Newton iterative scheme, where the iterations are stopped when the value of the error function, E_{Φ_m} , reduces to less than a certain tolerance value.

In most cases, the Hessian matrix, $\mathbf{H}_{E_{\Phi_m}}$, is ill-conditioned, and thus its direct inversion in solving the Newton equations given in Eq. (2.43) using row reduction techniques such as Gauss elimination method should be avoided because they are susceptible to round off errors. Therefore, *Conjugate gradient* (CG) method is generally used to solve Newton equations because it does not require second derivatives and it has low storage requirements. Accordingly, the minimization problem:

$$\min_d \left\| \mathbf{H}_{E_{\Phi_m}} d + \mathbf{J}_{E_{\Phi_m}} \right\| \quad (2.45)$$

is solved for the Newton search direction, d . Here $\|...\|$ denotes the L_2 norm (see Appendix A). The CG algorithm to solve the above Eq. (2.45) is given as:

$d^0 = \text{initial guess}$
 $g^0 = \nabla \left\| \mathbf{H}_{E_{\Phi_m}} d^0 + \mathbf{J}_{E_{\Phi_m}} \right\|$
 $s^0 = -g^0$
for $k = 0, 1, 2, \dots$
 Choose α^k *to minimize* $\left\| \mathbf{H}_{E_{\Phi_m}} (d^k + \alpha^k s^k) + \mathbf{J}_{E_{\Phi_m}} \right\|$
 $d^{k+1} = d^k + \alpha^k s^k$
 $g^{k+1} = \nabla \left\| \mathbf{H}_{E_{\Phi_m}} d^{k+1} + \mathbf{J}_{E_{\Phi_m}} \right\|$
 $\beta^{k+1} = \frac{(g^{k+1})^* g^{k+1}}{(g^k)^* g^k}$ *Fletcher - Reeves*
 or
 $\beta^{k+1} = \frac{(g^{k+1} - g^k)^* g^{k+1}}{(g^k)^* g^k}$ *Polak - Ribiere*
 $s^{k+1} = -g^{k+1} + \beta^{k+1} s^k$
end

Both Polak-Ribiere and Fletcher-Reeves algorithms are popularly used. Some workers³⁷ have also used a modification of Polak-Ribiere algorithm in the optical tomography problem.

Generally, the Newton method is unreliable unless started close enough to the solution. When started far from the solution, line search should be performed along the Newton search direction, d_k , to make method more robust (damped Newton). But, once iterations near solution, then the unit step length works fine for subsequent iterations. In addition, the calculation of Hessian matrices at each iteration is computationally intensive and is usually not feasible. For these reasons, the Newton method is usually modified in one way or the other, and the resulting methods are called *modified Newton*

method. In the following sections, we describe modified Newton approaches that have been utilized in our image reconstruction techniques.

2.2.2.2 Gauss-Newton method

In the description of Newton's method, we showed that the Jacobian of error function is given by $\mathbf{J}_{E_{\Phi_m}} = \nabla E_{\Phi_m}(\mu_{axf})$, which can alternatively be written as

$$\mathbf{J}_{E_{\Phi_m}} = \nabla \left(\frac{1}{2} [r]^* [r] \right) = \mathbf{J}_{[r]}^* [r] = \mathbf{J}_{\Phi_m^{calc}}^* [r], \quad (2.46)$$

where $\mathbf{J}_{[r]} = \mathbf{J}_{\Phi_m^{calc}}$ follows from Eq. (2.38) since Φ_m^{meas} are boundary measurements and do not depend upon the optimization variable μ_{axf} . Similarly the Hessian of the error function, $\mathbf{H}_{E_{\Phi_m}} = \nabla^2 E_{\Phi_m}(\mu_{axf})$, can be expressed as

$$\mathbf{H}_{E_{\Phi_m}} = \nabla^2 \left(\frac{1}{2} [r]^* [r] \right) = \mathbf{J}_{\Phi_m^{calc}}^* \mathbf{J}_{\Phi_m^{calc}} + \sum_{i=1}^m [r]_i \mathbf{H}_{[r]_i}, \quad (2.47)$$

where m is the length of residual vector, $[r]$. The above Eq. (2.47) shows that for each Newton step of Eq. (2.42), m Hessian matrices need to be calculated. This is usually inconvenient and highly computationally intensive. This motivates Gauss-Newton (GN) method for non-linear least square problems as in Eq. (2.37).

In GN method, the second term from Eq. (2.47) is dropped and the Hessian is approximated as:

$$\mathbf{H}_{E_{\Phi_m}} = \mathbf{J}_{\Phi_m^{calc}}^* \mathbf{J}_{\Phi_m^{calc}}, \quad (2.48)$$

and, thus, the system of linear equations

$$\mathbf{J}_{\Phi_m^{calc}}^* \mathbf{J}_{\Phi_m^{calc}} d_k = -\mathbf{J}_{\Phi_m^{calc}}^* [r], \quad (2.49)$$

is solved for approximate Newton step d_k at each iteration. Hence, the GN iterative scheme can be written as:

$$(\mu_{axf})_{k+1} = (\mu_{axf})_k - (\mathbf{J}_{\Phi_m^{calc}}^* \mathbf{J}_{\Phi_m^{calc}})^{-1} \mathbf{J}_{\Phi_m^{calc}}^* [r]. \quad (2.50)$$

In fluorescence-enhanced tomography problems, the GN Hessian matrix, $\mathbf{J}_{\Phi_m^{calc}}^* \mathbf{J}_{\Phi_m^{calc}}$, is generally ill-conditioned since the number of boundary measurements are usually less than the unknowns that are to be estimated. In addition, the general nonlinear relation between fluence and the optical properties adds to the ill-conditioning of the Jacobian matrix, $\mathbf{J}_{\Phi_m^{calc}}$. For this reason, the system of equations such as in Eq. (2.49) is solved in a least square sense:

$$\min_{d_k} \left\| \mathbf{J}_{\Phi_m^{calc}}^* \mathbf{J}_{\Phi_m^{calc}} d_k + \mathbf{J}_{\Phi_m^{calc}}^* [r] \right\|, \quad (2.51)$$

for the GN search directions, d_k . In this work, we have used conjugate gradient method, as described in the previous sections, to solve Eq. (2.51) for the GN search directions, d_k .

2.2.2.3 Truncated Newton method

In large-scale optimization problems, finding the solutions of Newton equations in Eq. (2.43) is expensive, and so Dembo and Steinhaug³⁸ introduced the idea of finding only the approximate solutions of the Newton equations. They argued that, when far from the minimum, Newton equations need not be solved accurately; instead they suggested solving the equations by CG method where the iterations are truncated before an

accurate solution is reached. Dembo and Steinhaug suggested using the size of the relative residual as the stopping criterion, such that if the relative residual,

$$\frac{\|\mathbf{H}_{E_{\Phi_m}} d^k + \mathbf{J}_{E_{\Phi_m}}\|^2}{(g^k)^* g^k} \leq \min\left(\frac{0.1}{k^2}, (g^k)^* g^k\right), \quad (2.52)$$

then the CG iteration is truncated and d^k is used as the search direction for the next step of the minimization problem. Thus d^k is set to be d_j , the search direction for the next step of the truncated Newton (TN) iterative scheme:

$$(\mu_{axf})_{j+1} = (\mu_{axf})_j + d_j. \quad (2.53)$$

In addition, the full Hessian matrix, $\mathbf{H}_{E_{\Phi_m}}$, is not calculated since only the product $\mathbf{H}_{E_{\Phi_m}} d$ is required. This product is calculated using the finite difference formula given as

$$\mathbf{H}_{E_{\Phi_m}}(\mu_{axf}) \cdot d = \frac{\mathbf{J}_{E_{\Phi_m}}(\mu_{axf} + \sigma d) - \mathbf{J}_{E_{\Phi_m}}(\mu_{axf})}{\sigma}, \quad (2.54)$$

where σ is taken to be as $\sqrt{\text{machine precision}} / \|d\|$.

2.2.2.4 Trust region methods

Similar to Newton method, TN method to update optimization variables in Eq. (2.53) also needs line search along the TN step direction, d_j , if started far from the solution. Line search methods need an “exact” or “close approximation” to the Jacobian matrix for efficient performance, which is often computationally intensive. An alternative to line search is *trust region* method, in which approximate solution is constrained to lie

within a specific region where the quadratic model of the objective function is sufficiently accurate. Previous researchers in our lab³⁹ have incorporated a TN based algorithm with trust regions to solve the fluorescence tomography problem. They have validated this algorithm to reconstruct interior absorption optical property map from synthetic measurements of fluorescence emission light performed on a 2D geometry.⁴⁰

2.2.2.5 Constrained optimization

The optimization strategies discussed in the above Section 2.2.2.1 through 2.2.2.4 are unconstrained methods, meaning that there is no check on the value the optimization variable might assume during the optimization process. One obvious place where this might be problematic is fluorescence imaging. In fluorescence imaging the physical parameters which are needed to be estimated as an outcome to the optimization process can not be a negative value. Using unconstrained methods, there is no control over what value an optimization variable should assume, and this necessitates the use of constrained optimization methods.

In our lab, Roy and Sevick-Muraca⁴¹ have developed an active constraint truncated Newton method using simple bounds suitable for fluorescence optical tomography. A detailed discussion of the simple bound constraints can be found in literature.^{42, 43}

2.3 Object models

In Section 1, we have reported that previous tomographic studies of detectability were done with target superimposed upon a spatially uniform background. In this work, however, the spatial inhomogeneity of exogenous and endogenous optical properties of the background is one of our primary concerns. The increase in complexity owing to the variability in the background can be achieved in several ways, but only those models are considered which lead to a description that is mathematically tractable. Two models are considered to simulate the normal background anatomy as a representation of the non-specific distribution of the fluorescent agent as well as the natural heterogeneity of the endogenous tissue optical properties. The first model, the lumpy-object model, is described in the following section and has been used in this work. The second model, the clustered lumpy-object model, is also described here and is the focus of our future studies involving the heterogeneous backgrounds.

2.3.1 Lumpy-object model

The lumpy-object model was developed by Rolland and Barrett⁴⁴ with the assumption that the background is a wide-sense stationary process (see Appendix A). The lumpy backgrounds consist of a random number of single structures or “blobs” located at random locations in the field of view (FOV). Mathematically these structures can be represented as:

$$b(\mathbf{r}) = b_0 + \sum_{n=1}^{N_p} lump(\mathbf{r} - \mathbf{r}_n | l_0, w), \quad (2.55)$$

where $b(\mathbf{r})$ is the lumpy background; b_0 is the spatial mean of the lumpy background; N_p is the Poisson-distributed number of lumps comprising the lumpy background; and \mathbf{r}_n is the uniformly distributed location of n th lump. The function *lump* has the following form:

$$lump(\mathbf{r} - \mathbf{r}_n | l_0, w) = l_0 \exp\left(\frac{-|\mathbf{r} - \mathbf{r}_n|^2}{2w^2}\right) - \frac{1}{V(\Omega)} \int_{\Omega} l_0 \exp\left(\frac{-|\mathbf{r} - \mathbf{r}_n|^2}{2w^2}\right) d^3\mathbf{r}, \quad (2.56)$$

where l_0 is the lump strength, w is the lump width, Ω is the domain, and $V(\Omega)$ is the volume of the domain. The second term⁴⁵ in this expression satisfies the requirement that the mean of the lumpy background is equivalent to b_0 , i.e. $\langle b(\mathbf{r}) \rangle = b_0$. This can be deduced by noticing that the mean of function *lump* in Eq. (2.56) is equal to zero.

2.3.2 Clustered lumpy-object model

In order to synthesize more complicated and realistic objects, Bochud *et al.*⁴⁶ extended the lumpy object model in 2D. Their model is known as clustered lumpy-object model and it basically clusters the lumps (similar to the lumpy objects described previously) around certain cluster centers which are uniformly distributed within the FOV. The mathematical form of the clustered lumpy objects is:

$$clb(\mathbf{r}) = \sum_{n=1}^{N_{cl}} \sum_{k=1}^{K_n} \Lambda([R_{\phi_n}](\mathbf{r} - \mathbf{r}_k - \mathbf{r}_{nk}) | l_0, w), \quad (2.57)$$

where N_{cl} is the number of clusters; K_n is the number of lumps defined by function Λ in the n th cluster; \mathbf{r}_k is the center of n th cluster; \mathbf{r}_{nk} is the center of the k th lump function in the n th cluster; and l_0 and w are the parameters that characterize the shape of the lumps

as described below. The rotation of the lumps is represented by rotation matrix R_{ϕ_n} . The quantities N_{cl} and K_n are both Poisson distributed. The center of a cluster \mathbf{r}_k is uniformly distributed over the FOV, and the locations of lumps \mathbf{r}_{nk} within a cluster are Gaussian distributed around \mathbf{r}_k . The lump function Λ is given by:

$$\Lambda([R_{\phi_n}](\mathbf{r} - \mathbf{r}_k - \mathbf{r}_{nk})|l_0, w) = l_0 \exp\left(\frac{-|\mathbf{r} - \mathbf{r}_k - \mathbf{r}_{nk}|^2}{2w^2}\right) \quad (2.58)$$

Bochud *et al.* generated these lumps in 2D, so the angle ϕ_n was uniformly distributed between 0 and 2π . For a 3D geometry, the various lumps inside a cluster are rotated by a solid angle uniformly distributed between 0 and 4π .

2.4 Objective assessment of image quality (OAIQ)

Any image assessment method is acceptable if it objectively quantifies the usefulness of the images for performing some specified task. Figures of merit for such task-based measures of image quality must be computable and scalar, so that its use in the optimization of the imaging system and the assessment of observer performance is not subject to misinterpretation. The following four elements are the key to the objective assessment of the image quality:⁴⁴

1. *Specification of a task*: Almost all medical imaging systems are designed with a task in mind. This task might be *detecting* a tumor inside a human breast or it might be *estimating* the exact size and location of the tumor.
2. *Description of the data*: Most of the researchers in the field of image science assess the quality of their images by comparing them with the ones produced by

some previously established method. Based upon the comparisons, they conclude that their method has some advantages. This method is not objective because the authors pick a single or in some cases a few images for the purpose of comparison. In contrast, OAIQ considers a number of images of some specific type for a data acquisition system and the statistics of the ensemble is studied. The ensemble incorporates both the variations coming from the measurement noise as well as the objects (patients).

3. *Description of the observer*: Once the task and the set of objects have been specified, there needs to be an observer or the strategy to acquire the information from the data set. Despite the anthropomorphic implication of the term *observer*, often times computer algorithms or mathematical observer models serve this purpose for human beings. A special type of observer, known as ideal observer, which utilizes all the available statistical information of the task to maximize the task performance will be discussed in the following sections.
4. *Figure of merit*: Figures of merit are a way of reporting how well the observer performs the task at hand. Some popular figures of merit for detection tasks include signal-to-noise ratio (SNR) and area under the curve (AUC) of receiver operating characteristic (ROC) curve.⁴⁷⁻⁴⁹

OAIQ incorporates these four elements to obtain quantitative measures of the image quality. The nomenclature convention of Barrett and Myers⁴⁴ has been followed in this section.

2.4.1 System model

The imaging system can be modeled using the *imaging equation*:

$$\mathbf{g} = \mathbf{H}(\mathbf{f}) + \mathbf{n}, \quad (2.59)$$

where \mathbf{f} is the object being imaged, \mathbf{H} is an operator that describes how the imaging system maps the object being imaged to the discrete vector of measurements \mathbf{g} , and \mathbf{n} is the noise in the measurement system (which may or may not depend on \mathbf{f}). So \mathbf{g} is actually the noisy image data returned by the imaging system. For example in fluorescence-enhanced optical imaging, the imaging operator \mathbf{H} is provided by the coupled diffusion equations (2.5) and (2.6); and \mathbf{g} can be a vector containing the excitation and/or emission fluence values (Φ_x/Φ_m), which is characterized by the amplitude and phase values of the photon density waves. In some cases, the measurement noise may be described by a Gaussian or Poisson distribution. The imaging operator \mathbf{H} is a nonlinear operator in \mathbf{f} in case the objects being imaged are the absorption optical parameters ($\mu_{ax,mi}, \mu_{ax,mf}$) or the lifetime of the fluorophore (τ), respectively known as absorption imaging and lifetime imaging. After the data \mathbf{g} have been acquired, they can be used in an imaging reconstruction algorithm \mathbf{O} , as described in Section 2.2.2, to determine or “reconstruct” an *estimate*, $\hat{\mathbf{f}}$, of the original object \mathbf{f} :

$$\hat{\mathbf{f}} = \mathbf{O}(\mathbf{g}). \quad (2.60)$$

For detection tasks to be described in the following sections, both operators \mathbf{H} and \mathbf{O} can be used for the image quality assessment purposes. Observer studies on \mathbf{H} are known as *hardware design*, while on \mathbf{O} are known as *software optimization*.⁴⁴

2.4.2 Detection tasks

In this work we restrict our discussion to the binary detection tasks, where two possible hypotheses are known as signal-present hypothesis (H_1) and signal-absent hypothesis (H_0). For example, in breast cancer detection, the H_1 hypothesis is that the image data is taken from a patient who has a tumor in the FOV, while the H_0 is that the data are from a patient who does not have a tumor.

$$\begin{aligned} H_1 : \quad & \mathbf{g} = \mathbf{H}(\mathbf{f} + \mathbf{t}) + \mathbf{n} \\ H_0 : \quad & \mathbf{g} = \mathbf{H}(\mathbf{f}) + \mathbf{n} \end{aligned} \tag{2.61}$$

Here \mathbf{f} represents the normal, non-tumor portion of the anatomy, while \mathbf{t} represents the tumor portion (signal) of the object. Both \mathbf{f} and \mathbf{t} are stochastic and vary from patient to patient. The observer performance is limited by the randomness in \mathbf{f} and the noise in the system.¹² To simulate the normal background anatomy, both lumpy-object and clustered lumpy-object models can be used to represent the non-specific distribution of the fluorescent contrast agent ($\mu_{ax,mf}$) and the natural heterogeneity of the endogenous tissue optical properties ($\mu_{ax,mi}$, and $\mu_{sx,m}$).

In detection problems, an observer uses an imaging data vector \mathbf{g} to infer which of the above described hypotheses was the source of the detected imaging data. Two restrictions are imposed on the manner the observer makes a decision. First, decisions are nonrandom meaning that repeated observations of the same data \mathbf{g} must result in same decision. Second, every observation results in an unequivocal decision. With these assumptions, the detection problem is essentially partitioning the imaging data space into distinct regions. In binary detection problems, the above is accomplished by

defining a *test statistic*, t , and then comparing it to a decision threshold, t_c , in order to make decisions. The test statistic is related to the imaging data through a *discriminating function* $T(\mathbf{g}) = t$.

For linear observers, $T(\mathbf{g})$ is a linear function of the imaging data, \mathbf{g} :

$$T(\mathbf{g}) = \mathbf{w}^T \mathbf{g}, \quad (2.62)$$

where superscript T denotes the transpose; and \mathbf{w} is a vector of same length as \mathbf{g} (say M). In case \mathbf{g} is complex, superscript T denotes the conjugate transpose and t is taken as the real part of the outcome of Eq. (2.62). The decision boundary based on t is an isocontour of this function $\mathbf{w}^T \mathbf{g}$, which is a hyperplane in M -dimensional space. Note that the test statistic can be a nonlinear function of the imaging data, but discussions are restricted to the linear observers in this work. Still, irrespective of its functional dependence, the test statistic t is a random variable through its dependence on \mathbf{g} . As a result, the probability density functions (PDF) on t can be defined. The PDFs on t depend on the underlying hypothesis, and are denoted as $pr(t | H_j)$ for hypothesis H_j . In general detection problems, the degree of overlap of the density functions of the test statistic determines the separability of the two hypotheses. This overlap determines the detectability of the target; the more the overlap the less detectable the target is. A measure of this overlap is given by the signal-to-noise ratio associated with t :

$$SNR_t = \frac{\langle t \rangle_1 - \langle t \rangle_0}{\sqrt{(\sigma_1^2 + \sigma_0^2)/2}}, \quad (2.63)$$

where subscripts denote the corresponding hypotheses; σ_j is the standard deviation of t under H_j hypothesis; and $\langle t \rangle_j$ denotes the mean of t under hypothesis H_j . It is to be noted that Eq. (2.63) assumes that the test statistic is normally distributed under both hypotheses.

In order to find an optimal linear observer, the expression for a linear discriminant that maximizes the measure of separability as given in Eq. (2.63) is generally needed. Barrett and Myers⁴⁴ show that the linear discriminant that maximizes the SNR takes the form:

$$\mathbf{w}_{opt\ lin} = \mathbf{K}_g^{-1} \Delta \bar{\mathbf{g}} \quad (2.64)$$

when the imaging data \mathbf{g} have equal covariance \mathbf{K}_g under each hypothesis. The resulting SNR is then given by

$$SNR_{opt\ lin}^2 = \Delta \bar{\mathbf{g}}^T \mathbf{K}_g^{-1} \Delta \bar{\mathbf{g}}, \quad (2.65)$$

where $\Delta \bar{\mathbf{g}}$ is the difference in the means of the data under the H_1 and H_0 hypotheses, averaged over all sources of variability.

An expression very similar to Eq. (2.65) was first given by Hotelling⁵⁰ for sample means and covariances (see Appendix B), so $\mathbf{w}_{opt\ lin}$ is called *Hotelling discriminant* and the observer who implements the optimal linear observer is called *Hotelling observer*. To adopt this terminology, the subscript *opt lin* is replaced with *Hot* henceforth.

In order to demonstrate that the Hotelling observer is indeed optimal in an SNR sense, it should be established that it achieves equal or better SNR than that achieved by

an arbitrary discriminant \mathbf{w} . An arbitrary discriminant has an SNR according to Eq. (2.63) of

$$SNR_{\mathbf{w}}^2 = \frac{(\mathbf{w}^T \Delta \bar{\mathbf{g}})^2}{\mathbf{w}^T \mathbf{K}_g \mathbf{w}}. \quad (2.66)$$

Thus it must be shown that

$$\begin{aligned} \frac{(\mathbf{w}^T \Delta \bar{\mathbf{g}})^2}{\mathbf{w}^T \mathbf{K}_g \mathbf{w}} &\leq \Delta \bar{\mathbf{g}}^T \mathbf{K}_g^{-1} \Delta \bar{\mathbf{g}} \\ \text{or } (\mathbf{w}^T \Delta \bar{\mathbf{g}})^2 &\leq (\mathbf{w}^T \mathbf{K}_g \mathbf{w})(\Delta \bar{\mathbf{g}}^T \mathbf{K}_g^{-1} \Delta \bar{\mathbf{g}}), \end{aligned} \quad (2.67)$$

since $\mathbf{w}^T \mathbf{K}_g \mathbf{w}$ is always positive. To show that Eq. (2.67) holds, start with its left-hand side and use triangle equality to get

$$(\mathbf{w}^T \Delta \bar{\mathbf{g}})^2 = [\mathbf{w}^T \mathbf{K}_g^{1/2} \mathbf{K}_g^{-1/2} \Delta \bar{\mathbf{g}}]^2 \leq \|\mathbf{w}^T \mathbf{K}_g^{1/2}\|^2 \|\mathbf{K}_g^{-1/2} \Delta \bar{\mathbf{g}}\|^2. \quad (2.68)$$

Writing the norms of the vectors as inner products yields

$$(\mathbf{w}^T \Delta \bar{\mathbf{g}})^2 \leq (\mathbf{K}_g^{1/2} \mathbf{w})^T (\mathbf{K}_g^{1/2} \mathbf{w}) (\mathbf{K}_g^{-1/2} \Delta \bar{\mathbf{g}})^T (\mathbf{K}_g^{-1/2} \Delta \bar{\mathbf{g}}) = (\mathbf{w}^T \mathbf{K}_g \mathbf{w})(\Delta \bar{\mathbf{g}}^T \mathbf{K}_g^{-1} \Delta \bar{\mathbf{g}}). \quad (2.69)$$

This proves the inequality in Eq. (2.67), which shows that SNR in Eq. (2.65) is that of an optimal linear observer which performs equal to or better than any other arbitrary linear observer in an SNR sense. Consequently, we have used the Hotelling observer in this work to assess the hardware of our imaging system.

2.4.3 Hardware design

The design of an imaging system should enable the observer to optimally perform the intended tasks. It is not feasible to optimize the system parameters after the system has been built. Thus, it is necessary to accurately model the imaging system and assess the

quality of the data from the simulated imaging systems. A mathematically ideal observer should be employed to optimize the hardware parameters for a specific task.

Since the ideal Bayesian observer requires complete knowledge of the statistics of the image data under both hypotheses, the use of its performance as a figure of merit is limited.⁴⁴ In fluorescence-enhanced optical imaging the high computation time of the forward problem prohibits the use of ideal Bayesian observer. As an example, the fixed mesh forward solver takes approximately 20 seconds for a domain with ~ 7000 nodes on a LINUX workstation with AMD Opteron 250 (2.4 GHz) and 4.0 GB RAM, which does not include the time for generation of the lumps. For ideal Bayesian observer performance studies, the forward solver has to be run at least one hundred thousand times, which would take roughly about 20×10^5 seconds ≈ 23 days, and thus is not computationally feasible. Similarly, the Bayesian observer performance studies on the inverse imaging algorithm using the above mentioned domain would require more than 4 years. Therefore, a far more computationally feasible ideal linear observer, *the Hotelling observer*, needs to be employed.^{44, 51}

As described in the above Section 2.4.2, the Hotelling observer requires estimates on the first and second order statistics on the data \mathbf{g} . It computes the confidence level using only the linear manipulations on the data \mathbf{g} and maximizes the SNR of the test statistics. The Hotelling observer's test statistic is given by the equation:

$$\chi_{Hot}(\mathbf{g}) = \Delta \bar{\mathbf{g}}^T \mathbf{K}_g^{-1} \mathbf{g}. \quad (2.70)$$

Where $\Delta\bar{\mathbf{g}}$ is the difference in the means of the data under the H_1 and H_0 hypotheses, averaged over all sources of variability; and \mathbf{K}_g is the average covariance of the data \mathbf{g} . Mathematically,

$$\Delta\bar{\mathbf{g}} = \langle \mathbf{g}(\mathbf{f} + \mathbf{t}) \rangle - \langle \mathbf{g}(\mathbf{f}) \rangle. \quad (2.71)$$

Note that since the fluorescence-enhanced optical imaging system is nonlinear, $\langle \mathbf{g}(\mathbf{t}) \rangle \neq \langle \mathbf{g}(\mathbf{f} + \mathbf{t}) \rangle - \langle \mathbf{g}(\mathbf{f}) \rangle$. The SNR of the Hotelling test statistic as a figure of merit^{44, 45} is given by Eq. (2.65), which can be written as:

$$SNR_{Hot}^2 = \Delta\bar{\mathbf{g}}^T \mathbf{K}_g^{-1} \Delta\bar{\mathbf{g}} \quad (2.72)$$

In Eq. (2.72), the calculation of the inverse of the covariance matrix, \mathbf{K}_g^{-1} , is a computationally intensive step. Two sources of randomness in fluorescence imaging are the objects \mathbf{f} and noise \mathbf{n} in the measurement data. Since statistical properties of noise \mathbf{n} may depend on \mathbf{f} , two types of averages are defined:

$$\bar{\mathbf{g}}_f = \langle \mathbf{g} \rangle_{n|f}, \quad (2.73)$$

$$\bar{\bar{\mathbf{g}}} = \langle \bar{\mathbf{g}}_f \rangle_f. \quad (2.74)$$

The first average is the conditional average over all the realizations of \mathbf{n} for a fixed \mathbf{f} . The second average is over both the noise as well as object variations.

The overall covariance matrix, \mathbf{K}_g , is given by the following expression:

$$\mathbf{K}_g = \langle (\mathbf{g} - \bar{\bar{\mathbf{g}}})(\mathbf{g} - \bar{\bar{\mathbf{g}}})^T \rangle_{n,f}. \quad (2.75)$$

Using the laws of conditional expectations, the above expression can be written:

$$\begin{aligned}
\mathbf{K}_g &= \left\langle \left\langle (\mathbf{g} - \bar{\mathbf{g}})(\mathbf{g} - \bar{\mathbf{g}})^T \right\rangle_{n|f} \right\rangle_f \\
&= \left\langle \left\langle (\mathbf{g} - \bar{\mathbf{g}}_f + \bar{\mathbf{g}}_f - \bar{\mathbf{g}})(\mathbf{g} - \bar{\mathbf{g}}_f + \bar{\mathbf{g}}_f - \bar{\mathbf{g}})^T \right\rangle_{n|f} \right\rangle_f \\
&= \left\langle \left\langle (\mathbf{g} - \bar{\mathbf{g}}_f)(\mathbf{g} - \bar{\mathbf{g}}_f)^T + (\bar{\mathbf{g}}_f - \bar{\mathbf{g}})(\bar{\mathbf{g}}_f - \bar{\mathbf{g}})^T + (\mathbf{g} - \bar{\mathbf{g}}_f)(\bar{\mathbf{g}}_f - \bar{\mathbf{g}})^T + (\bar{\mathbf{g}}_f - \bar{\mathbf{g}})(\mathbf{g} - \bar{\mathbf{g}}_f)^T \right\rangle_{n|f} \right\rangle_f \\
&= \left\langle \left\langle (\mathbf{g} - \bar{\mathbf{g}}_f)(\mathbf{g} - \bar{\mathbf{g}}_f)^T \right\rangle_{n|f} \right\rangle_f + \left\langle \left\langle (\bar{\mathbf{g}}_f - \bar{\mathbf{g}})(\bar{\mathbf{g}}_f - \bar{\mathbf{g}})^T \right\rangle_{n|f} \right\rangle_f + \left\langle \left\langle (\mathbf{g} - \bar{\mathbf{g}}_f)(\bar{\mathbf{g}}_f - \bar{\mathbf{g}})^T \right\rangle_{n|f} \right\rangle_f \\
&\quad + \left\langle \left\langle (\bar{\mathbf{g}}_f - \bar{\mathbf{g}})(\mathbf{g} - \bar{\mathbf{g}}_f)^T \right\rangle_{n|f} \right\rangle_f \\
&= \left\langle \left\langle (\mathbf{g} - \bar{\mathbf{g}}_f)(\mathbf{g} - \bar{\mathbf{g}}_f)^T \right\rangle_{n|f} \right\rangle_f + \left\langle \left\langle (\bar{\mathbf{g}}_f - \bar{\mathbf{g}})(\bar{\mathbf{g}}_f - \bar{\mathbf{g}})^T \right\rangle_{n|f} \right\rangle_f + \mathbf{0} + \mathbf{0}. \quad (\text{since } \langle \mathbf{g} \rangle_{n|f} = \bar{\mathbf{g}}_f)
\end{aligned}$$

This shows that \mathbf{K}_g is a sum of two different covariance matrices:

$$\mathbf{K}_g = \bar{\mathbf{K}}_n + \mathbf{K}_{\bar{g}}, \quad (2.76)$$

such that

$$\bar{\mathbf{K}}_n = \left\langle \left\langle (\mathbf{g} - \bar{\mathbf{g}}_f)(\mathbf{g} - \bar{\mathbf{g}}_f)^T \right\rangle_{n|f} \right\rangle_f \quad (2.77)$$

is the average noise-covariance matrix; and

$$\mathbf{K}_{\bar{g}} = \left\langle \left\langle (\bar{\mathbf{g}}_f - \bar{\mathbf{g}})(\bar{\mathbf{g}}_f - \bar{\mathbf{g}})^T \right\rangle_{n|f} \right\rangle_f \quad (2.78)$$

is the average-data covariance matrix. Since $\mathbf{g} = \mathbf{H}(\mathbf{f}) + \mathbf{n}$, Eq. (2.73) can be simplified

as:

$$\begin{aligned}
\bar{\mathbf{g}}_f &= \langle \mathbf{g} \rangle_{n|f} \\
&= \langle \mathbf{H}(\mathbf{f}) + \mathbf{n} \rangle_{n|f} \\
&= \langle \mathbf{H}(\mathbf{f}) \rangle_{n|f} + \langle \mathbf{n} \rangle_{n|f} \\
&= \langle \mathbf{H}(\mathbf{f}) \rangle_{n|f}. \quad (\text{since } \langle \mathbf{n} \rangle_{n|f} = \mathbf{0})
\end{aligned}$$

Using the above expression for $\bar{\mathbf{g}}_f$ into Eq. (2.77) yields:

$$\begin{aligned}
\bar{\mathbf{K}}_n &= \left\langle \left\langle (\mathbf{g} - \bar{\mathbf{g}}_f)(\mathbf{g} - \bar{\mathbf{g}}_f)^T \right\rangle_{n|f} \right\rangle_f \\
&= \left\langle \left\langle (\mathbf{H}(\mathbf{f}) + \mathbf{n} - \mathbf{H}(\mathbf{f}))(\mathbf{H}(\mathbf{f}) + \mathbf{n} - \mathbf{H}(\mathbf{f}))^T \right\rangle_{n|f} \right\rangle_f \\
&= \left\langle \left\langle \mathbf{nn}^T \right\rangle_{n|f} \right\rangle_f, \tag{2.79}
\end{aligned}$$

where \mathbf{nn}^T is the tensor product of \mathbf{n} with itself. The values of $\mathbf{K}_{\bar{g}}$ and $\bar{\mathbf{K}}_n$ obtained from Eq. (2.78) and (2.79) are substituted in Eq. (2.76) to estimate the covariance matrix \mathbf{K}_g , which, when substituted in Eq. (2.72), gives the estimate of the SNR of the Hotelling observer (the *Hotelling SNR*).

As an example, the CPU time required for the assessment of the tumor detection task using a domain with ~ 7000 nodes would roughly be one minute times the number of optical property maps used, which is computationally more feasible than to use a Bayesian observer.

3. EVALUATION OF ANATOMICAL STRUCTURE AND NON- UNIFORM DISTRIBUTION OF IMAGING AGENT IN NEAR- INFRARED FLUORESCENCE-ENHANCED OPTICAL TOMOGRAPHY*

3.1 Introduction

Fluorescence-enhanced optical imaging may hold promise for diagnostic cancer imaging with molecularly targeting fluorescent agents. Currently, the “gold-standards” for clinical molecular imaging are the nuclear techniques of gamma scintigraphy, positron emission tomography (PET), and single photon emission computed tomography (SPECT).^{5, 6} Since radiotracers have a finite half-life and cannot be “re-activated” *in vivo*, the signal to noise available for planar imaging or tomographic reconstruction can be limiting. A similar scenario exists for bioluminescence imaging which can also be starved for signal since the generation of light is governed by the diffusional encounter of an enzyme and its consumable substrate. In contrast, fluorescence imaging may (i) have higher signal to noise ratio owing to the ability of a fluorophore to undergo repeated activation and radiative relaxation; (ii) result in enhanced target-to-background ratio (TBR) values since imaging can be delayed without concern of agent half-life or availability of substrate; but (iii) may suffer greater penetration losses at increasing

* Reprinted with permission from “Evaluation of anatomical structure and non-uniform distribution of imaging agent in near-infrared fluorescence-enhanced optical tomography,” by A. K. Sahu, R. Roy, A. Joshi and E. M. Sevick-Muraca, *Optics Express* **13**, 10182-10199 (2005). ©2005 by Optical Society of America.

tissue depths than nuclear imaging approaches.⁷ The opportunity to conjugate fluorophores to targeting peptides, antibodies, and enzyme substrates has already been well demonstrated in several laboratories using small animal imaging.

When fluorophore excitation and emission occurs in the near-infrared range (750-900 nm) and light is multiply scattered as it travels a centimeter or more in tissues, image formation can be achieved from inversion of time-dependent measurements made at the tissue surface using the coupled diffusion equations.^{7, 10, 52-54} When used in small volumes, tomographic imaging requires the use of the time-dependent radiative transport equations (RTE),⁵⁵ although some investigators have employed diffusion based tomography with time-invariant measurements.⁵⁶ In addition, while diffusion-based tomography is performed across large volumes with measurements between points of illumination and collection on the tissue boundary, 3-D image reconstruction has also been developed for area illumination and collection.^{57, 58} Herein, we will focus on diffusion-based tomographic imaging from time-dependent measurements conducted in the frequency-domain between points of illumination and collection in the presence of natural anatomical heterogeneity and heterogeneous distribution of fluorescent agent in the geometry typical of human breast. We chose this geometry owing to our past experimental studies involving a breast-shaped phantom⁵⁹ and employ optical property values that are similar to those reported in the literature⁶⁰⁻⁷⁰ [13-23] and summarized in Table 3.1.

Table 3.1 Experimental breast optical property values reported in literature.

Authors	λ (nm)	μ_a (cm ⁻¹)	μ_s' (cm ⁻¹)	Experimental method
1989, Marchesini <i>et al.</i> ⁶⁰	635	≤ 0.2	395 \pm 35*	Absorbance was measured by an integrating sphere; extinction coefficient by goniophotometry; scattering coefficient by taking the average of the differences between the above two
1990, Peters <i>et al.</i> ⁶¹	550	200-300	300-900†	Standard integrating sphere techniques to measure diffuse reflectance and transmittance; Monte Carlo simulations to derive the values of optical properties
	1100	50-100	100-500†	
1993, Kang <i>et al.</i> ⁶²	670	0.01-0.025	3-17	NIR Time Resolved Spectroscopy
1996, Suzuki <i>et al.</i> ⁶³	753	0.035-0.08	7-10.75	Time Resolved Spectroscopy in the transmission geometry
		0.0225-0.05	6.25-10.50	
1996, Troy <i>et al.</i> ⁶⁴	749	0.0763-0.2592	0.6148-1.3106	Double integrating sphere techniques
	789	0.0163-0.0818	0.5088-1.2205	
	836	0.0235-0.1077	0.4776-1.0458	
1997, Tromberg <i>et al.</i> ⁶⁵	674	0.035-0.04	8.5-11.0	(normal breast)
		0.055-0.07	7.9-9.1	(tumor-containing breast)
		0.085-0.1	6.7-9.7	(normal breast)
	956	0.012-0.0165	6.7-7.9	(tumor-containing breast)

Table 3.1 Continued

Authors	λ (nm)	μ_a (cm ⁻¹)	μ_s' (cm ⁻¹)		Experimental method
1999, Grosenick <i>et al.</i> ⁶⁶	785	0.082-0.12	9.4-11.6	(breast tumor tissue)	Time-domain optical mammography
		0.042	9.0-10.8	(surrounding tissue)	
2001, Shah <i>et al.</i> ⁶⁷	‡	0.048-0.15	8.3-11.0	(premenopausal)	Frequency Domain Photon Migration
		0.016-0.064	6.7-8.3	(postmenopausal)	
2002, Durduran <i>et al.</i> ⁶⁸	750	0.046±0.024	8.7±2.2		Employed a diffuse optical imager in the compressed breast geometry
	786	0.041±0.025	8.5±2.1		
	830	0.046±0.027	8.3±2.0		
2003, Culver <i>et al.</i> ⁶⁹	690	0.024	10.8		Diffuse Optical Spectroscopy based on Frequency Domain Photon Migration technique
	750	0.0425	10.0		
	786	0.039	9.75		
	830	0.05	9.9		
2004, Shah <i>et al.</i> ⁷⁰	674	-	9.2-10.4	(premenopausal)	Diffuse Optical Spectroscopy based on Frequency Domain Photon Migration technique
		-	8.8-9.6	(postmenopausal)	

* Value of μ_s (value of anisotropy coefficient, g , not reported).

† Value of μ_s with $g=0.945-0.985$.

‡ Average value of four wavelengths of 674, 803, 849, and 956 nm.

The outline of this section is as follows: In Section 3.2, we present (i) the forward model and finite element mesh for predicting boundary measurements of frequency-domain photon migration (FDPM) measurements between points of illumination and collection in the presence of optical property heterogeneity, and (ii) a brief description of the inversion scheme used to provide reconstructed images. In Section 3.3, we provide example reconstructed images at varying levels of optical property heterogeneity to show the insensitivity to endogenous optical properties in fluorescence-enhanced optical imaging. Our results also indicate the sensitivity of tomographic imaging to uneven distribution of molecularly targeted agents in normal tissues. The results provide the framework for OAIQ.

3.2 Methods

Time-dependent, frequency-domain measurements consist of launching intensity modulated excitation light (typically modulated at 100 MHz) from a single point on the tissue boundary. The intensity modulated excitation light propagates as a photon density wave through the tissue, activating fluorophores and generating intensity modulated emission light. The generated emission photon density wave is phase-shifted and amplitude attenuated relative to its activating excitation light due to the decay kinetics of the fluorophore. The emission photon density wave propagates to the tissue boundary where it is collected for evaluation of its amplitude and phase delay for input into the image reconstruction algorithm.

3.2.1 Forward model and finite element solver

Near-infrared light propagation in tissues can be modeled by the diffusion approximation of the radiative transport equation. In the frequency domain the photon diffusion equation is generally written as:

$$\frac{i\omega}{c}\Phi(\mathbf{r},\omega) - \nabla \cdot [D(\mathbf{r})\nabla\Phi(\mathbf{r},\omega)] + \mu_a(\mathbf{r})\Phi(\mathbf{r},\omega) = S(\mathbf{r},\omega). \quad (3.1)$$

Here ω is the modulation frequency of the NIR source (rad/s); $\Phi(\mathbf{r},\omega)$ is the photon fluence rate ($photons/(cm^2s)$) at position \mathbf{r} ; D is the photon diffusion coefficient (cm); μ_a is the absorption coefficient (cm^{-1}); $S(\mathbf{r},\omega)$ is the photon source strength ($photons/(cm^3s)$) at position \mathbf{r} ; c is the speed of light in the medium (cm/s). The generation and propagation of the fluorescence diffuse photon density wave can be described by the following coupled diffusion equations:

$$-\nabla \cdot [D_x(\mathbf{r})\nabla\Phi_x(\mathbf{r},\omega)] + \left[\frac{i\omega}{c} + \mu_{axi}(\mathbf{r}) + \mu_{axf}(\mathbf{r}) \right] \Phi_x(\mathbf{r},\omega) = S(\mathbf{r},\omega), \quad (3.2)$$

$$-\nabla \cdot [D_m(\mathbf{r})\nabla\Phi_m(\mathbf{r},\omega)] + \left[\frac{i\omega}{c} + \mu_{ami}(\mathbf{r}) + \mu_{amf}(\mathbf{r}) \right] \Phi_m(\mathbf{r},\omega) = \phi\mu_{axf}(\mathbf{r}) \frac{1+i\omega\tau}{1+[\omega\tau]^2} \Phi_x(\mathbf{r},\omega), \quad (3.3)$$

where the subscript x denotes excitation and m denotes emission. The term $\mu_{ax,mi}$ denotes the absorption due to endogenous chromophores; $\mu_{ax,mf}$ denotes the absorption due to the exogenous fluorophores; ϕ is fluorescent quantum; and τ is fluorescent lifetime (s). The diffusion coefficient is given by:

$$D_{x,m} = \frac{1}{3(\mu_{ax,mi} + \mu_{ax,mf} + \mu_{sx,m}(1-g))}, \quad (3.4)$$

where $\mu_{sx,m}$ denotes the scattering coefficients at excitation and emission wavelength; and g is the coefficient of anisotropy of the medium. We solve these equations with the Robin type boundary conditions:

$$2D_{x,m} \frac{\partial \Phi_{x,m}}{\partial n} + \gamma \Phi_{x,m} = 0, \quad (3.5)$$

where n denotes the outward normal to the surface and γ is the constant depending upon the optical refractive index mismatch at the boundary. Eq. (3.2) through (3.5) can be solved numerically to yield,

$$\Phi_{x,m}(\mathbf{r}, \omega) = I_{AC_{x,m}} \exp(-i\theta_{x,m}(\mathbf{r}, \omega)). \quad (3.6)$$

Here $\Phi_{x,m}$ is a complex number, and $\theta_{x,m}$ is the measured phase lag and $I_{AC_{x,m}}$ is the measured amplitude of the photon density wave at excitation and emission wavelengths.

Unlike finite difference methods, finite element methods can solve coupled diffusion equations (3.2) and (3.3) over complex domains. We employ a Galerkin scheme for solution of these equations over a breast-shaped geometry described in Fig. 3.1 and used in prior experimental studies in our laboratory.⁹

3.2.2 Endogenous and exogenous optical property heterogeneity

We consider the lumpy-object model developed by Rolland and Barrett¹² to simulate the normal background anatomy as a representation of the non-specific distribution of the

fluorescent agent as well as the natural heterogeneity of the endogenous tissue optical properties. The lumpy backgrounds consist of a random number of single structures or “blobs” located at random locations. Mathematically these structures can be represented as:

$$b(\mathbf{r}) = b_0 + \sum_{n=1}^{N_p} lump(\mathbf{r} - \mathbf{r}_n), \quad (3.7)$$

where $b(\mathbf{r})$ is lumpy background; b_0 is the spatial mean of the background; N_p is the Poisson-distributed number of lumps; and \mathbf{r}_n is the uniformly distributed location of n th lump. The function $lump$ has the following form:

$$lump(\mathbf{r} - \mathbf{r}_n) = l_0 \exp\left(\frac{-\|\mathbf{r} - \mathbf{r}_n\|^2}{2w^2}\right) - \frac{1}{V(\Omega)} \int_{\Omega} l_0 \exp\left(\frac{-\|\mathbf{r} - \mathbf{r}_n\|^2}{2w^2}\right) d^3\mathbf{r}, \quad (3.8)$$

where l_0 is the lump strength, w is the lump width, Ω is the domain, and $V(\Omega)$ is the volume of the domain. The second term in this expression satisfies the requirement that the mean of the lumpy background is equivalent to b_0 , i.e., $\langle b(\mathbf{r}) \rangle = b_0$.⁴⁵

Lumpy backgrounds have the advantage of being mathematically/statistically tractable and stationary.⁴⁴ This facilitates an organized manner for implementing OAIQ tools for image analysis. These lumpy backgrounds are represented in the uniform mesh of the FEM forward model of generated image data sets which are used to compute the tomographic reconstruction images.

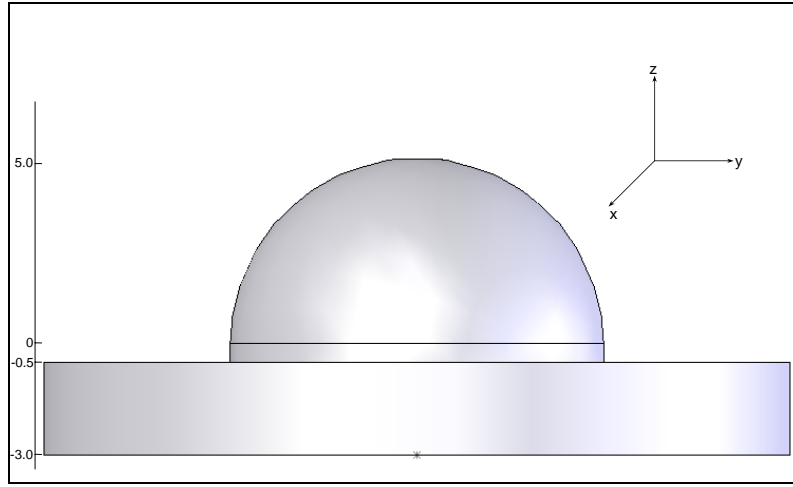


Fig. 3.1 The geometry of the breast-shaped phantom. The dimensions are in centimeters. The bigger cylindrical volume has a circular base of diameter 20 cm. The hemisphere has a radius of 5 cm.

The breast geometry (shown in Fig. 3.1) consisted of two cylinders of radii 10 cm and 5 cm with heights of 2.5 cm and 0.5 cm respectively, and a hemisphere of radius 5 cm. A total of 6956 nodes and 34413 tetrahedral elements were used to discretize the domain. The lump strength, l_0 , was set to be a prescribed percentage ranging from 0 to 100% of the mean background value b_0 ; and the lump spread, w , and number of lumps, N_p , were set to be 5 mm and 100 respectively. As an example, 5% lumpy background of the endogenous or exogenous properties meant that the strength of lump, l_0 , was 0.05 times the average background value (b_0) of the optical property. Due to the large volume and surface illumination of excitation light on the hemispherical portion, the intensity of the excitation light was found to be low outside the hemispherical portion of the simulated phantom. As a consequence, simulated heterogeneity present in the cylindrical portions did not have an effect on the tomographic reconstruction. Therefore heterogeneities were simulated only in the hemispherical portion of the breast-shaped

geometry. Therefore, in the breast geometry, Ω corresponds to the hemispherical portion and $V(\Omega)$ corresponds to its volume (see Eq. (3.8)). In order to position the lumps, a random number between 0 and +5 assigned the z-position of the center of the lump, and two random numbers between -5 and +5 assigned its x and y-position. Only if the resulting center of the lump (x, y, z) resided within the hemisphere, was the heterogeneity counted as one of N lumps, where the value of N was fixed to 100.

Lumps were generated for all endogenous (μ_{axi} , μ_{ami} , μ_{sx} , and μ_{sm}) and exogenous (μ_{axf} and μ_{amf}) optical parameters. Lumps were first *independently* generated at prescribed percentages for endogenous properties of μ_{axi} and μ_{sx} , and the exogenous property of μ_{axf} . The lump strengths in the optical parameters of μ_{ami} and μ_{amf} were taken to be a factor of that in μ_{axi} and μ_{axf} respectively. The factor essentially reflects the wavelength-dependent absorption owing to tissue chromophores and can be thought of as the ratio of bulk extinction coefficients of tissue at excitation and emission wavelengths.

Similarly the lump strength in the optical parameter of μ_{sm} was taken to be a factor of that in μ_{sx} . The factor effectively represents the ratio of bulk wavelength dependent scattering efficiency at excitation and emission wavelengths. In this study, we simulated indocyanine green (ICG) as the contrast agent. Thus, the multiplication factors were taken considering the absorption and emission spectra of ICG at 780 nm (excitation) and at 830 nm (emission) wavelengths, respectively. The factors for relating lumps in optical properties at the emission wavelength to those independently generated

for lumps in optical properties at the excitation wavelength are given in Table 3.2. For example, in order to generate lumps in the absorption coefficients due to endogenous chromophores, the spatial distribution and strength of lumps in μ_{axi} were first calculated using Eq. (3.7), and the strength of these lumps were then multiplied by the corresponding factor from Table 3.2 to obtain lumps in μ_{ami} . For endogenous lumpy object models, the forward solution was solved in the presence of lumps in (μ_{axi} , μ_{ami} , μ_{sx} , and μ_{sm}) as well as in the presence of a prescribed fluorescent target. For exogenous lumpy object models, the forward solution was solved in the presence of lumps in (μ_{axi} , μ_{ami} , μ_{sx} , and μ_{sm}) and (μ_{axf} and μ_{amf}) as well as in the presence of a fluorescent target.

Table 3.2 Constant factors to obtain lumps at emission wavelength from the generated lumps at excitation wavelength.

Lumps in	μ_{ami}	μ_{sm}	μ_{axf}
Multiplication factor	1.2968	0.9030	0.1692

The fluorescent target was taken to be a spherical volume of 1 cm³ centered at spatial coordinates (0.5599, -2.4707, 2.4968) with higher contrast than the background.

Generation of the optical property heterogeneity map and solution of the forward solution was conducted on a workstation with Intel Pentium IV 2.80 GHz and 1.0 GB RAM. The calculation of the volume integral in Eq. (3.8) was a computationally time

consuming step and has been performed using a Simpson quadrature method for numerical integration provided in MATLAB[®].

The background tissue optical properties are provided in Table 3.3. The target was assumed to have the same optical properties as the background except for the values of μ_{axf} and μ_{amf} . The values of μ_{axf} and μ_{amf} for the target were 100, 50 and 25 times more than that of the average background values, and are presented as three different case studies in this work. While actual TBR values may be ten-fold or greater, we employ these ratios assuming molecular targeting of agents. Twenty five point sources and 128 detectors on the hemispherical surface were employed to obtain the synthetic measurements, as shown in Fig. 3.2.

Table 3.3 Average background optical properties. Also given are the parameters used in equations (3.2) through (3.4). The optical properties used in the simulations are similar to breast tissue optical properties reported in literature (see Table 3.1).

wavelength↓	μ_{ai} ,	μ_s ,	μ_{af} ,	ω ,	c ,	g ,	ϕ ,	τ ,
	[cm ⁻¹]	[cm ⁻¹]	[cm ⁻¹]	[rad/s]	[cm/s]	[]	[]	[s]
excitation (780 nm)	0.02483	108.792	0.00299	6.28e8	2.25e10	0.9	.016	0.56e-9
emission (830 nm)	0.0322	98.241	0.000506					

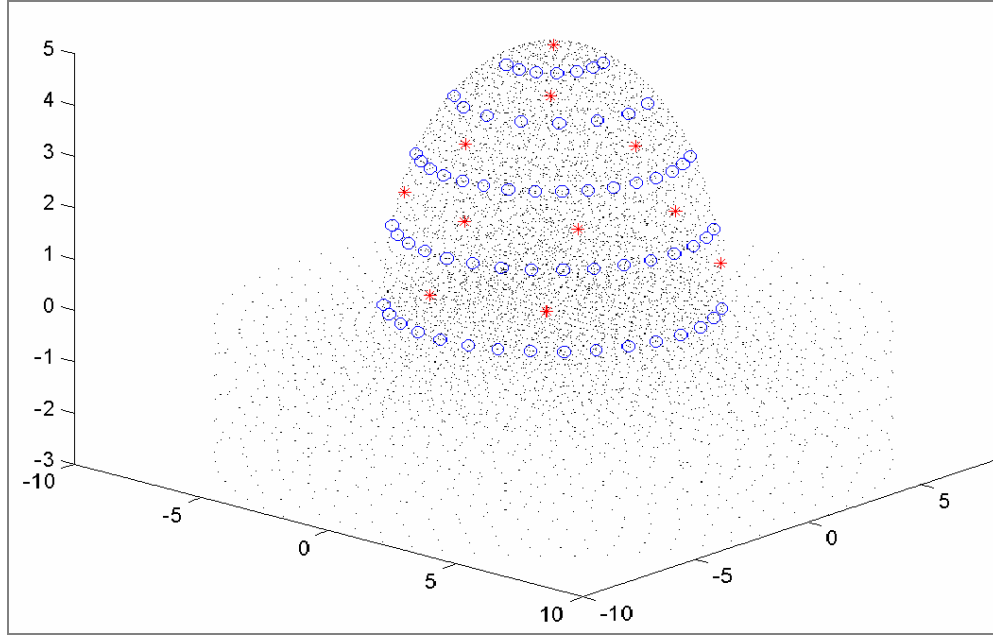


Fig. 3.2 The positions of laser sources and detectors on the breast phantom. The stars are the positions of the sources and the circles are the positions of the detectors.

3.2.3 Inverse imaging algorithm

As described in Section 2.2.2, the starting point for formulating the reconstruction as an optimization problem begins with defining the error function, $E(\mu_{axf})$:

$$E(\mu_{axf}) = \frac{1}{2} \sum_{p=1}^{N_B} \left[\left(\log(Z_p)_{cal} - \log(Z_p)_{mea} \right) \left(\log(Z_p)_{cal}^* - \log(Z_p)_{mea}^* \right) \right], \quad (3.9)$$

subject to the constraint $\{l \leq \mu_{axf} \leq u\}$, where l is the lower and u is the upper bound of μ_{axf} . For optical tomography problems, a range, i.e., the lower and upper bounds, is specified for the optimization variables based on physical consideration. In above equation cal denotes the value calculated by the forward problem; mea denotes the synthetic measured values and N_B is the number of detectors. The superscript $*$ denotes

the complex conjugate of the complex number Z_p . Z_p is comprised of the referenced fluorescent amplitude, I_{ACref_p} , and the referenced phase shift θ_{ref_p} measured at boundary point, p , in response to point illumination. Specifically, the referenced measurement at boundary point p can be given by:

$$Z_p = I_{ACref_p} \exp(-i\theta_{ref_p}). \quad (3.10)$$

The reference scheme was used in the synthetic data to remove the influence of the unknown source strength.⁷¹ In this scheme, the emission fluence, Φ_m , from multiple collection fiber locations were referenced with respect to the excitation fluence data from the same fiber as given in the following equation:

$$\frac{(\Phi_m)_p}{(\Phi_x)_p} \quad p=1,\dots,N_B \quad (3.11)$$

where p is the position of collection on the surface of the phantom. Thus, the relative phase shift and AC ratio were calculated from the difference in phase [i.e.,

$$(\Delta\theta_m)_p = (\theta_m)_p - (\theta_x)_p] \quad \text{and} \quad \text{the ratios of amplitude [i.e.,}$$

$$(\Delta I_{ACm})_p = (I_{ACm})_p / (I_{ACx})_p].$$

The penalty modified barrier function method with simple bounds constrained optimization technique PMBF/CONTN was used for reconstruction and is presented in detail elsewhere.⁵⁷ In the PMBF/CONTN method, the modified barrier penalty function,

M (termed hereafter as the barrier function), is used to incorporate the constraints directly within the optimization variable:

$$\min_{\mu_{axf}} M(\mu_{axf}, \lambda, \eta) = E(\mu_{axf}) - \eta \sum_{i=1}^N \left\{ \lambda_i^l f(\mu_{axf_i} - l) + \lambda_i^u f(u - \mu_{axf_i}) \right\}, \quad (3.12)$$

where η is a penalty/barrier term; f is a logarithmic function; N is the number of nodal points; λ^l and λ^u are vectors of Lagrange multipliers for the bound constraints of the lower and the upper bounds, respectively. From Eq. (3.12) one can see that the simple bounds are included in the barrier function M .

The PMBF/CONTN method is performed in two stages within an inner and an outer iteration. The outer iteration updates the Lagrange multiplier λ and the barrier parameter η using the formulations presented elsewhere.⁵⁷ Using the calculated values of the parameters λ and f , the constrained truncated Newton with trust region method is applied to minimize the penalty barrier function described in Eq. (3.12). Once satisfactory convergence within the inner iteration is reached or a specified number of inner iterations has been exceeded, the variables describing PMBF convergence and fractional change in the outer iteration are recalculated to check for convergence. If unsatisfactory, the Lagrange multipliers, λ , and the barrier parameter, η , are updated and another constrained optimization is started within the inner iteration. Herein we use the modified method of Breitfeld and Shanno⁷² for initializing the Lagrange multipliers without a priori information. This approach effectively removes the need to choose an appropriate initial value of the Lagrange multipliers based upon ground truth, which, in actual patient imaging, may or may not be available. This algorithm is novel in the

sense that the constrained have been included within the optimization variable and no *a priori* information is required for the regularization parameters. The algorithm has been validated from experimental data employing planar and point illumination/collection geometries.⁵⁷

The image reconstruction computations were performed on a LINUX workstation with AMD Opteron 250, 2.4 GHz and 4.0 GB RAM. For image reconstruction, synthetic measurements of emission photon density wave amplitude and phase delay were obtained by solving the forward problem in the presence of the fluorescent target and various lumpy optical backgrounds. These synthetic measurements were input into the PMBF/CONTN inverse algorithm to recover the exogenous optical property (μ_{axf}) distribution for tumor detection task. In this initial study for detecting the target in the reconstructed tissues, we use the optical property map of the reconstructed μ_{axf} and the *a priori* knowledge about the location of the actual target. If the reconstructed map shows a single structure whose centroid lies within 1 cm radius of the actual target's centroid, then we look for any other structures present in the domain. If no other structures are present, then it is deemed that the target was detected successfully. If other structures are present, but they are located outside a 2 cm radius of the centroid of the actual target, then successful detection of the target is accomplished in the presence of artifacts. However, if no structure is present within 1 cm radius of the actual target's centroid, then the reconstruction algorithm has failed to detect the target. Another case of failure occurs when a structure is reconstructed near the actual target's location but is less than half of the actual target's volume. In all of

these cases further investigation is recommended to define the criteria for the detection tasks.

3.2.4 Figures of merit for image analysis

In order to assess the performance of the PMBF/CONTN algorithm for the detection tasks, both qualitative (visual) and quantitative (centroid of the reconstructed target and RMSE) measures were used. The general mesh viewer, GMV, software was used to plot the reconstructed images.

The centroid of the reconstructed target, \mathbf{r}_c , was calculated using the following expression:

$$\mathbf{r}_c = \frac{\sum_{i=1}^{N_T} \mu_{axf_i} \mathbf{r}_i}{\sum_{i=1}^{N_T} \mu_{axf_i}}, \quad (3.13)$$

where index i represents the nodes present in the reconstructed target. The term N_T denotes total nodes present and \mathbf{r}_i denotes the coordinates of the i th node in the reconstructed target. The centroids of the reconstructed targets can be compared with the centroid of the actual target to assess the detection accuracy of the algorithm.

Similarly, the RMSE values were calculated using the expression:

$$RMSE = \sum_{i=1}^N \left\{ \frac{1}{N} \left(\mu_{axf}^{calc} - \mu_{axf}^{actual} \right)_i^2 \right\}, \quad (3.14)$$

where N is total number of nodes in the domain. Superscript *calc* denotes the values obtained using reconstruction algorithms; and *actual* denotes the actual distribution of

μ_{axf} which was used to generate the synthetic image data sets. RMSE values of the reconstructed target are used to assess the relative accuracy of the algorithm for different lump strengths and TBR.

3.3 Results and discussion

3.3.1 Generation of lumpy backgrounds

The generation of lumpy backgrounds required ~40 min of CPU time for each independent optical property parameter (with a predefined lump strength value). Figures 3.3(a) through 3.3(c) illustrate movies of cross sections of an example distribution of μ_{axi} , μ_{sx} , and μ_{axf} for the 25% endogenous and exogenous lumpy background model in the absence of a fluorescent target.

3.3.2 Tomographic image reconstruction

The “ground truth” target position defined by TBR of 100:1 absorption (μ_{axf}) in the phantom is shown in Fig. 3.4.

Figure 3.5 illustrates the PMBF/CONTN recovery of absorption coefficient owing to fluorophore from synthetic data with lumpy endogenous background (*i.e.* lumps in μ_{axi} , μ_{ami} , μ_{sx} , and μ_{sm}) of 1% lump strength. Reconstructed images for other lump strengths are not shown here for brevity, but the fluorescent target was recovered for lump strength up to 100%. We found that reconstructed images show the insensitivity to the various lump strength values and can be easily reconstructed for 1%-100% lumps in the background. Each image reconstructed with PMBF/CONTN required

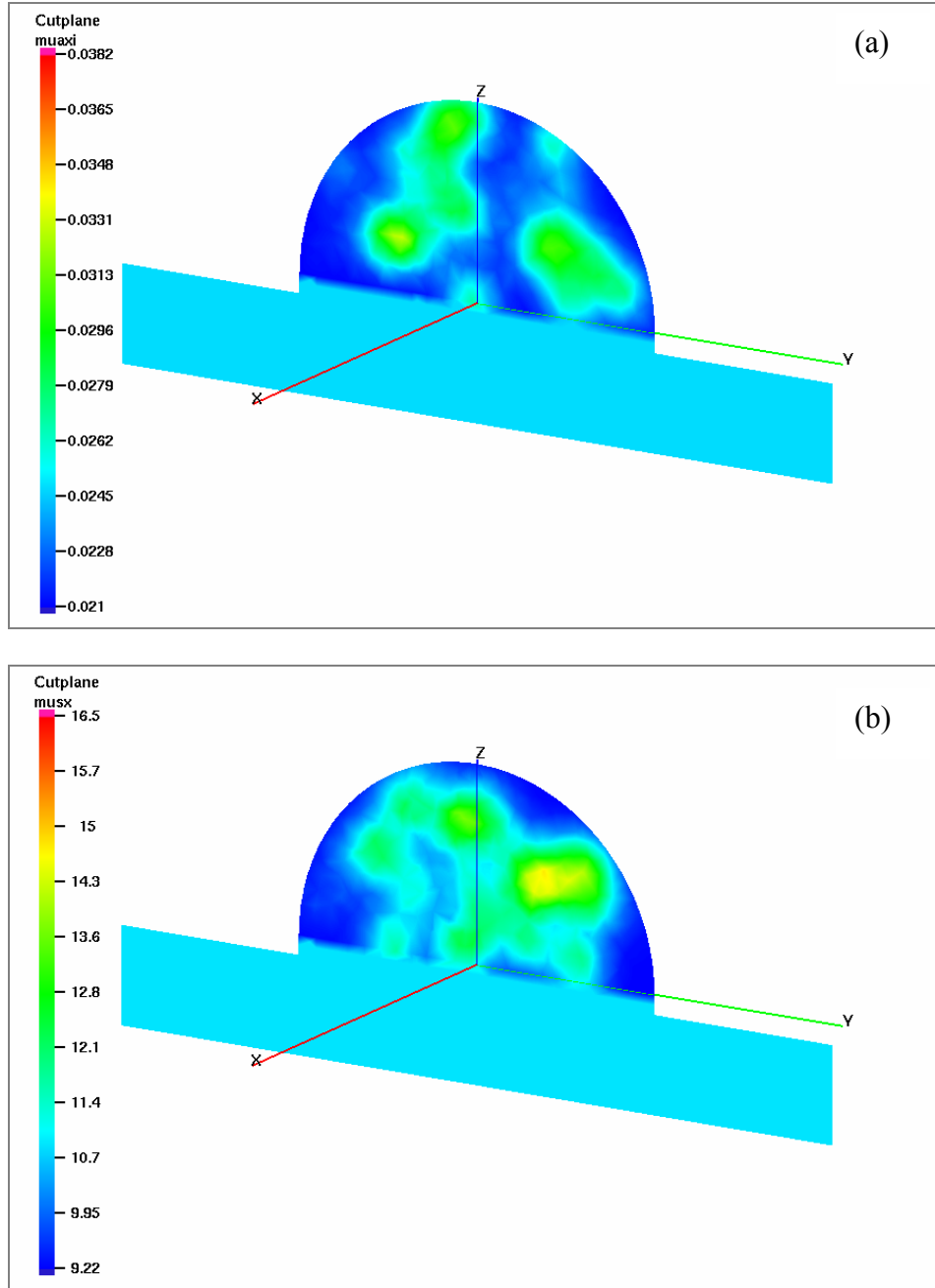


Fig. 3.3 Figures of the lumps in endogenous and exogenous optical properties using Lumpy object model. The lumps in μ_{axi} (a), μ_{sx} (b), and μ_{axf} (c) are shown as the cutplanes to the breast geometry (Fig. 3.1) parallel to yz -plane and passing through $x=0.20$ cm. The spread of the lumps are 5mm and there are 100 lumps uniformly generated in the hemispherical volume. The lumps have the strength values of 25% of the average background values of μ_{axi} , μ_{sx} , and μ_{axf} given in Table 3.3.

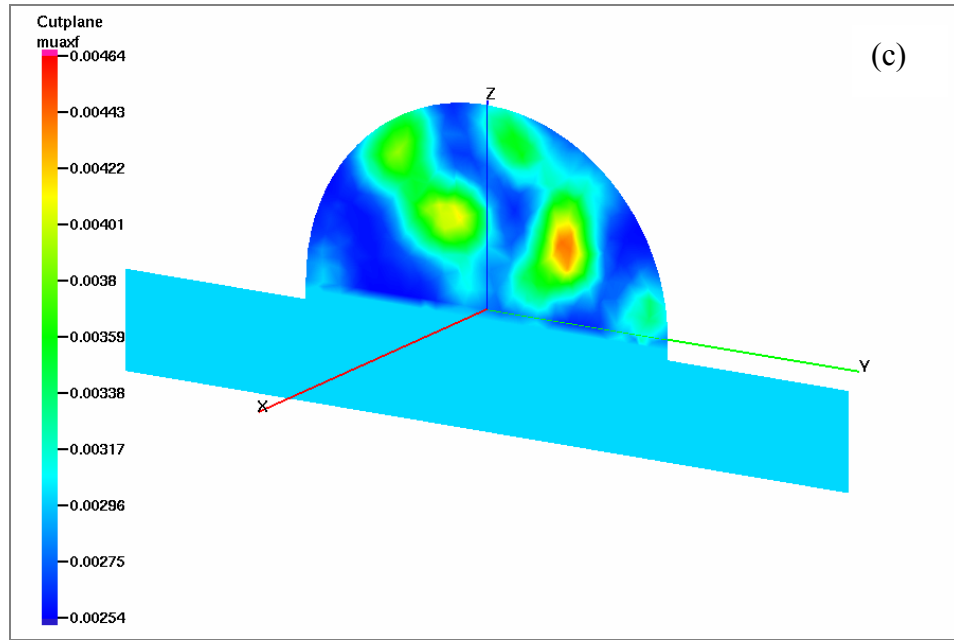


Fig. 3.3 Continued

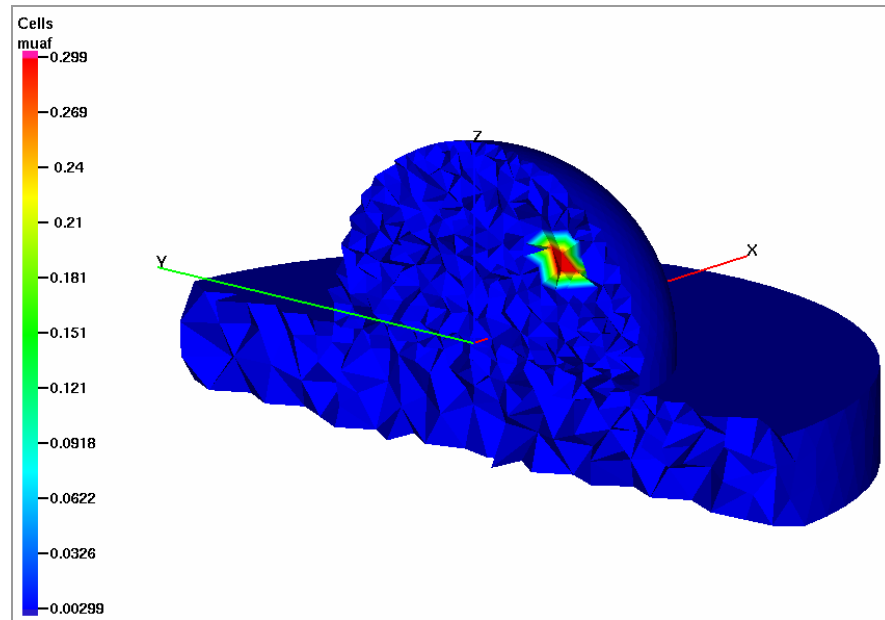


Fig. 3.4 Actual distribution of exogenous optical property of the target inside the breast phantom. The colorbar shows the values of μ_{af} in cm^{-1} . The target has μ_{af} value 100 times more than that of the background. The Fig. shown is a cut plane parallel to yz-plane and passing through point $x=0.5$. The lumps in the background are not shown here.

~3 hr of CPU time. The centroid and the mean displacement of the reconstructed targets are given in Tables 3.4 and 3.5, respectively, and show that the reconstructed target locations have little error, indicating good detection capability of the PMBF/CONTN in the presence of endogenous lumps.

The RMSE values as a function of endogenous lump strength for the targets reconstructed are shown in Fig. 3.6. The figure shows that the changes in RMSE values are small for different lump strengths. However, the small change in RMSE is consistent with the modest change in boundary measurements owing to change of endogenous optical property.^{64, 73} It should be noted that the RMSE values for different lump strengths are used to compare the relative error in the image reconstruction task.

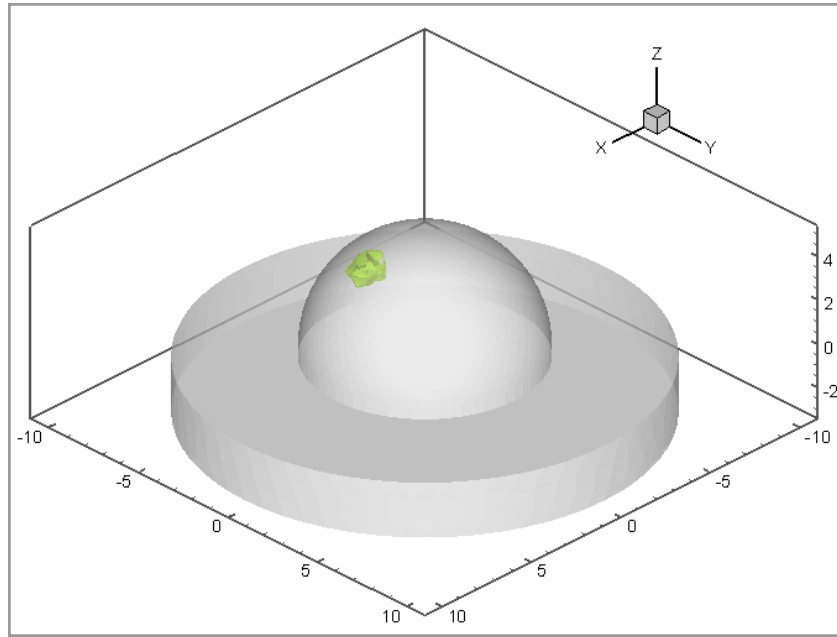


Fig. 3.5 Figure showing the recovered distribution of exogenous optical property in the presence of 1% lumps in endogenous optical properties using the PMBF/CONTN inverse algorithm. The figure shows the isosurface corresponding to the 70% of the maximum value of the reconstructed

μ_{axf} .

Table 3.4 Centroid of the reconstructed targets with varying lump intensities. The coordinate dimensions are in centimeters.

Lump strength	Endogenous lumps only	Endogenous as well as exogenous lumps		
	100:1	100:1	50:1	25:1
1%	(0.5173, -2.7055, 2.5588)	(0.5173, -2.7054, 2.5588)	(0.4017, -2.7209, 2.5800)	(0.4380, -2.6519, 2.5980)
5%	(0.5172, -2.7054, 2.5591)	(0.5431, -2.6830, 2.5688)	(0.3803, -2.6922, 2.5791)	(0.4082, -2.6914, 2.5983)
10%	(0.5437, -2.6826, 2.5680)	(0.5436, -2.6832, 2.5680)	(0.4302, -2.7235, 2.5706)	(0.4059, -2.7416, 2.5339)
25%	(0.3821, -2.6616, 2.5925)	(0.5097, -2.6809, 2.6371)	(0.3969, -2.6314, 2.6429)	(0.7496, -2.6415, 2.8959) ^d
50%	(0.3071, -2.6685, 2.5565)	(0.3334, -2.6102, 2.5604)	(0.3405, -2.6317, 2.5568)	(0.3908, -2.4834, 2.5743) ^e
100%	(0.1791, -2.6538, 2.6027) ^a	(0.2750, -2.5631, 2.6173) ^b	* ^c	* ^f

* could not reconstruct the target

^a one artifact at (-4.0357, 0.1921, 2.9389)

^b one artifact at (-4.0356, 0.1927, 2.9389)

^c couple of artifacts at (0.9162, -2.9192, 2.652) and (-4.0355, 0.1945, 2.9389)

^d one artifact at (-3.3784, 0.1012, 3.2824)

^e one artifact at (-3.3784, 0.1012, 3.2824)

^f one artifact at (-3.8683, 0.2660, 2.9282)

Table 3.5 The mean displacement of the reconstructed targets with respect to the actual target's centroid. The dimension is in centimeters.

Lump strength	Endogenous lumps only	Endogenous as well as exogenous lumps		
	100:1	100:1	50:1	25:1
1%	0.2466	0.2465	0.3075	0.2407
5%	0.2466	0.2248	0.2968	0.2864
10%	0.2241	0.2247	0.2936	0.3138
25%	0.2779	0.2577	0.2715	0.4738
50%	0.3265	0.2735	0.2787	0.1864
100%	0.4356	0.3228	*	*

* could not reconstruct the target

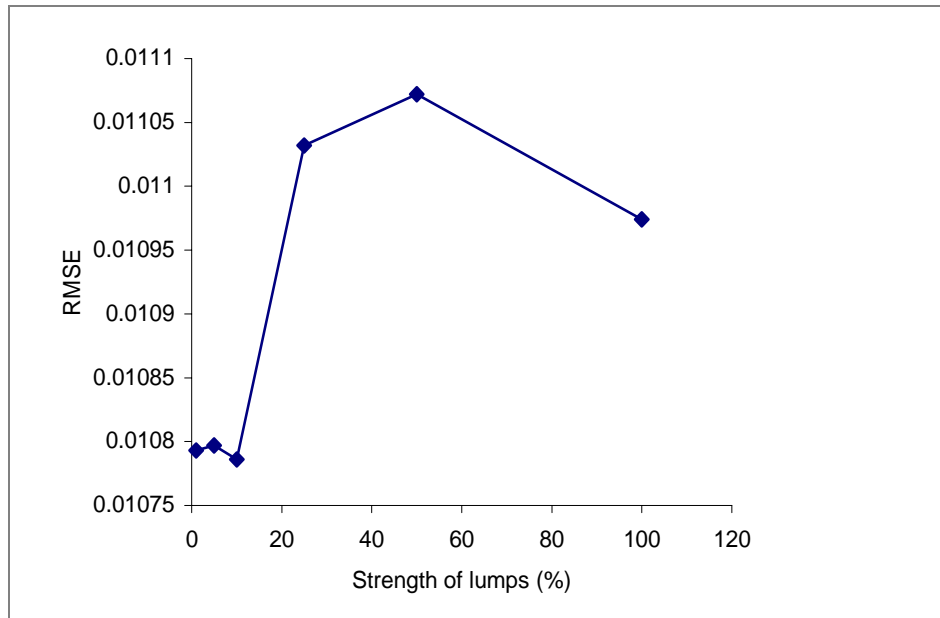


Fig. 3.6 The root mean square error (RMSE) values of the reconstructed images in the presence of endogenous lumps in the background. The target-to-background ratio (TBR) is 100:1 and the RMSE is calculated with respect to the actual distribution of the fluorophore shown in Fig. 3.4.

In contrast to the case of endogenous optical property heterogeneity, as the lump strength of exogenous contrast becomes comparable to that of the target, the task of discriminating the target from the background becomes more difficult. Except for the

case where TBR contrast ratio was 100:1, we could not reconstruct the target in a background containing exogenous and endogenous lump strengths up to 100% as shown for endogenous lumps alone. The target could not be reconstructed for lump strength values exceeding 50% in the case of TBR of 50:1 and 25:1. It should be noted that in case of 50:1 TBR with 100% lumps in the background, we did see a reconstructed volume at the position of actual target, but since its volume was less than that of the actual target's volume, our criteria did not enable definitive identification.

Fig. 3.7 shows the PMBF/CONTN recovery of absorption coefficient in the presence of 1% endogenous and exogenous lumps in the background for the three cases of TBR of 100:1, 50:1, and 25:1. Figures illustrating recovery at other lump strengths are not shown here for brevity. The centroid and the mean displacement of the reconstructed targets are given in Tables 3.4 and 3.5, respectively, for all the three cases of TBR values (100:1, 50:1 and 25:1).

The RMSE values were calculated as a function of TBR and are plotted in Fig. 3.8 for each case of endogenous and exogenous lump strength ranging from 1% to 50%. The general trend is that the RMSE value increases as the contrast decreases for each lump strength. This can be explained by the fact that as the contrast decreases the target has lower fluorophore concentration and thus the background lumps in exogenous optical properties are more pronounced with respect to the target. Thus, the inverse algorithm becomes more prone to fail, which it does at lump strength values exceeding 50% in the case of 50:1 and 25:1 TBR values.

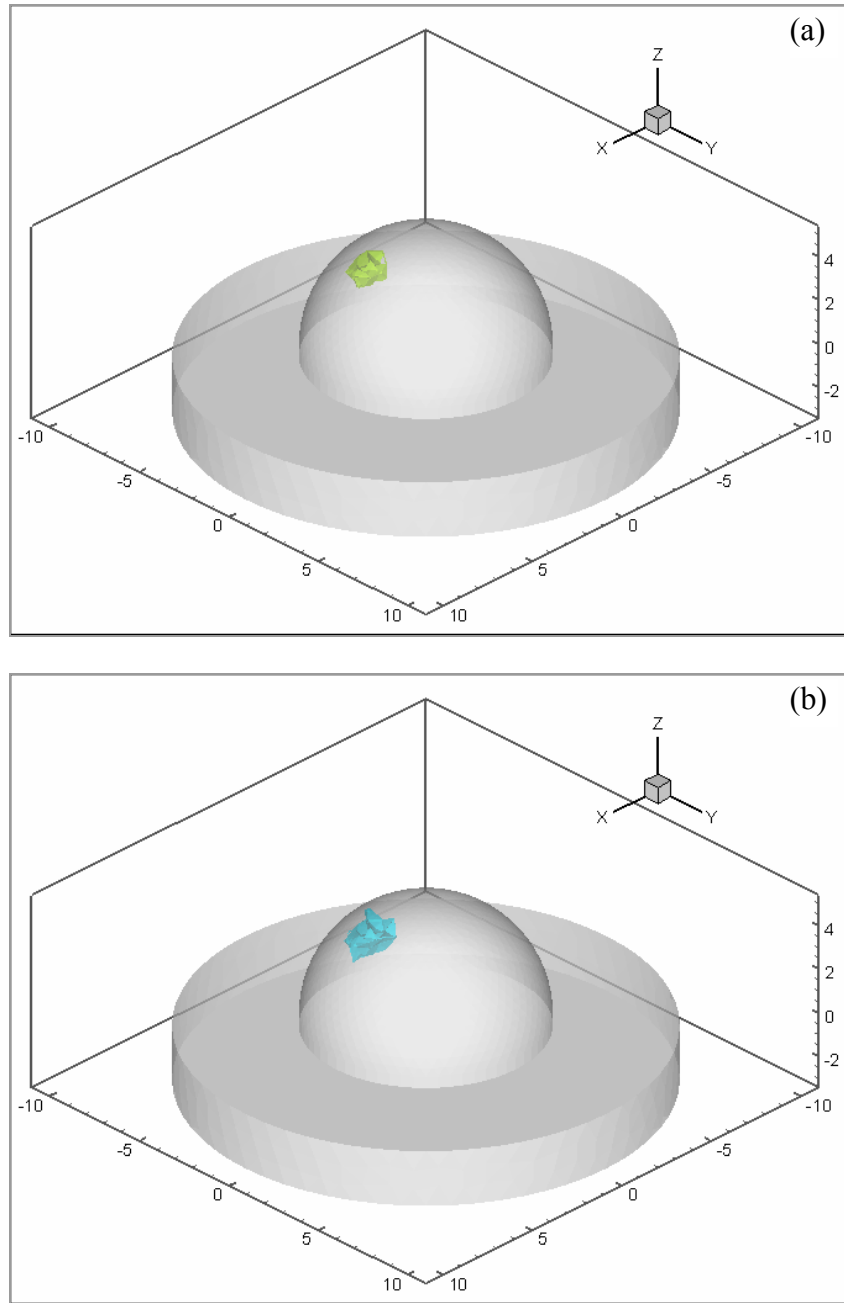


Fig. 3.7 The recovered distribution of exogenous optical property in the presence of 1% lumps in endogenous as well as exogenous optical properties using the PMBF/CONTN inverse algorithm. Figures (a), (b), and (c) are respectively for TBR values of 100:1, 50:1, and 25:1. The figures show the isosurfaces corresponding to the 70% of the maximum value of the reconstructed μ_{axf} .

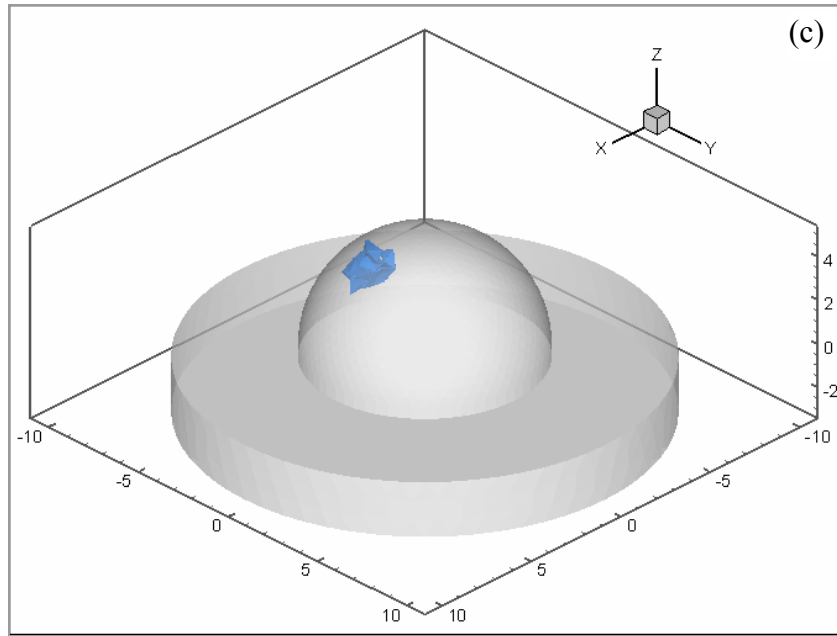


Fig. 3.7 Continued

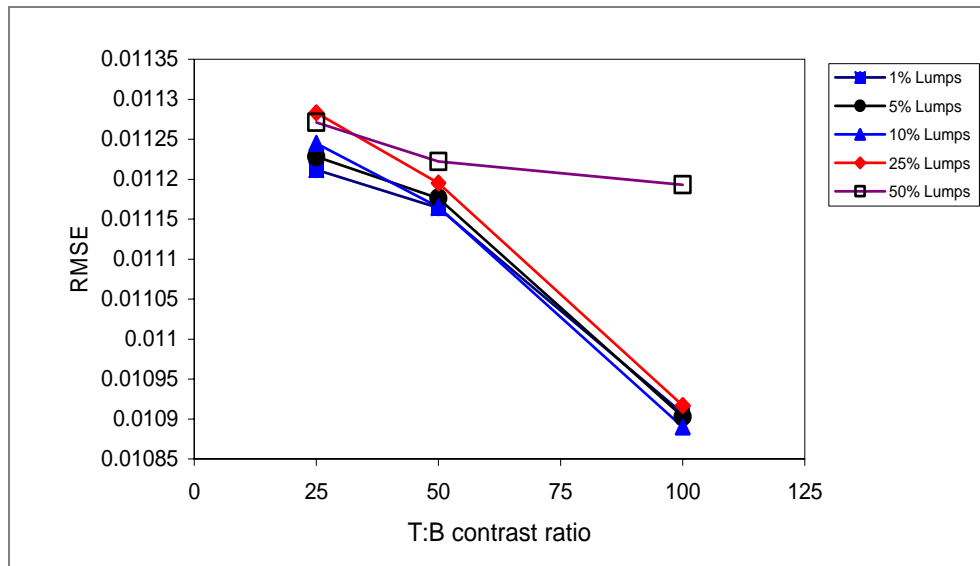


Fig. 3.8 The root mean square error (RMSE) values of the reconstructed images in the presence of endogenous as well as exogenous lumps in the background. The plots for all the three cases of TBR values are shown and the RMSE is calculated with respect to the actual distribution of the fluorophore including the target distribution shown in Fig. 3.4 and the exogenous lumps in the background. The values for 100% are not shown here since we could not reconstruct the target for the TBR values of 50 and 25.

It is important to note that in all of the above reconstruction tasks, the inverse algorithm had no prior knowledge about the lumps. In fact, the inverse algorithm was provided with only the average background values of the optical properties. This is also practically significant because in the real world nothing will be known about the spatial distribution of the optical properties of the tissue to be imaged. Since the approximate average values of the optical properties can be assessed through FDPM spectroscopy measurements, the average background values may be an appropriate input into the inverse imaging algorithm.

Finally, the results contained herein represent single cases of tomographically reconstructed targets in a background of lumps. In order to perform OAIQ for target detection and estimation tasks, random generation of background lumps across hundreds or thousands of cases need to be simulated in order to generate a statistical number of reconstructed images. As a result, we will be able to generate RMSE for lumpy backgrounds with varying lump strengths in order to ascertain error bars in each of these strength value points. This will be helpful in determining the error bars on Fig. 3.6 in order to better understand its behavior. In this work, we demonstrate the feasibility of generating images from lumpy backgrounds without *a priori* information. With the ability to reconstruct targets in the presence of lumpy backgrounds, we can now engage in OAIQ for fluorescence-enhanced optical tomography. Accordingly, the assessment of our imaging system using OAIQ tools is the main focus of the next two sections in this dissertation.

3.4 Conclusions

In fluorescence-enhanced optical tomography, the natural anatomical background is one source of randomness in the task of detecting a molecularly targeting fluorescent agent. Another source will be the lower level expression of disease markers throughout normal tissue which will be responsible for a “background” heterogeneity that also may impact image quality. Computer algorithms for analysis of task performance of fluorescence imaging require a method of simulating natural anatomical background of endogenous optical properties and the heterogeneous background expression of disease markers; as well as a robust image recovery program which does not require the use of *a priori* information. Herein, we provide a preliminary assessment of the image reconstruction algorithms and lumpy background model as method to establish the feasibility for using OAIQ tools for assessing image performance.

4. ASSESSMENT OF A FLUORESCENCE-ENHANCED OPTICAL IMAGING SYSTEM USING THE HOTELLING OBSERVER*

4.1 Introduction

Recently, numerous investigations have demonstrated the use of fluorescently labeled agents for molecularly-targeted imaging in small animal studies. Despite the potential advantages of non-radioactive and non-mutagenic imaging, to date, there have been no optical imaging studies of fluorescently labeled agents for molecular imaging in the clinic. While there has been demonstration of fluorescence-enhanced optical tomography in phantoms of clinically relevant volumes and homogeneous optical properties,^{10, 57} there has been no systematic study predicting potential performance in detection tasks for the relevant case of non-uniform distribution of fluorescent contrast agents or heterogeneity of endogenous optical properties owing to normal anatomical tissue structure.

In this contribution, a lumpy-object model developed by Rolland and Barrett¹² is used to simulate the anatomical structure as well as the heterogeneous background expression of disease markers that lead to non-uniform background distribution of fluorescent imaging agent. The lumpy-object model has been utilized by previous researchers in (i) the simulation studies to incorporate variability present in the reconstructed images of clinical positron emission tomography (PET) and single photon

* Reprinted with permission from “Assessment of a fluorescence-enhanced optical imaging system using the Hotelling observer,” by A. K. Sahu, A. Joshi, M. A. Kupinski, and E. M. Sevick-Muraca, *Optics Express* **14**, 7642-7660 (2006). ©2006 by Optical Society of America.

emission computed tomography (SPECT);¹³ (ii) the generation of synthetic mammograms;⁷⁴ as well as (iii) the observer studies involving digital radiography.⁷⁵ Pineda *et al.*²¹ have used lumpy-object model to explore the impact of normal anatomical tissue structure upon absorption imaging using time-dependent measurements of light propagation in the time-domain. We have employed lumpy-object model to demonstrate the ability to tomographically image fluorescent targets in the breast from frequency-domain measurements of fluorescence.⁷⁶ In fluorescence-enhanced optical imaging using frequency-domain techniques, intensity modulated NIR light is launched onto the tissue surface, wherein it propagates within the tissue, encounters a fluorophore, and generates emission light. Both emission and excitation light travel throughout the medium and the amplitude attenuation and phase delay of the emitted fluorescent light relative to the incident excitation light are detected at the surface. In order to tomographically image fluorescent targets deep inside the tissue, the boundary measurements are used within an optimization framework to determine interior distributions of the optical properties.^{10, 57}

In this study, the Hotelling observer is used to assess the detection of a fluorescent target from boundary frequency-domain measurements. The Hotelling observer's signal-to-noise ratio (SNR_{Hot}) is a measure of the task performance and has been widely used to evaluate the imaging hardware for tumor detection task in imaging modalities such as PET,^{77, 78} SPECT,^{79, 80} digital mammography,^{81, 82} and optical coherence tomography.⁸³ Evaluation of imaging system for target detection tasks using the Hotelling observer requires a large number of imaging data sets and, thus, is not

easily performed using patient image or experimentally obtained phantom data. However, the use of lumpy-objects to simulate heterogeneous distribution of optical properties that may be typical of human tissue allows generation of sizeable imaging data sets from computer simulation. Consequently, we simulate measurement data and incorporate expected systematic measurement error and noise of a fluorescence imaging system in order to use the Hotelling observer to assess performance in detection tasks. To our knowledge, this is the first time that an observer model is used to statistically assess the detection performance of a fluorescence-enhanced optical imaging system through analyzing the statistics of the imaging data sets.

In the following Section 4.1, we present (i) the imaging equation describing the propagation of modulated excitation and emission light in the tissue-like medium and the generation of emission light that is collected as measurements at the tissue boundary; (ii) a model to simulate the heterogeneous distribution of optical properties of biological tissues; (iii) the description of systematic measurement errors and noise; and (iv) an ideal linear observer and its figure of merit used to quantify the detection performance. Section 4.2 reports how the detection capability of the imaging system, as quantified by Hotelling observer's SNR, is affected by: (i) perturbations in endogenous and exogenous optical properties; (ii) target depth; and (iii) excitation light leakage through rejection filters.

4.2 Methods

In the objective quality assessment of imaging systems, an imaging model is specified, an evaluation criterion is defined, and the observer evaluating the system is described. These basic components of the image quality assessment are described in this section for fluorescence-enhanced optical imaging.

4.2.1 The imaging equation

As described in Section 2.1, the time-dependent generation and propagation of photon density waves diffusely transiting a highly scattering medium are described by the coupled diffusion equations, which are presented for the frequency-domain measurements as:³⁰

$$-\nabla \cdot [D_x(\mathbf{r})\nabla\Phi_x(\mathbf{r},\omega)] + \left[\frac{i\omega}{c} + \mu_{axi}(\mathbf{r}) + \mu_{axf}(\mathbf{r}) \right] \Phi_x(\mathbf{r},\omega) = S(\mathbf{r},\omega) \quad (4.1)$$

$$\begin{aligned} -\nabla \cdot [D_m(\mathbf{r})\nabla\Phi_m(\mathbf{r},\omega)] + \left[\frac{i\omega}{c} + \mu_{ami}(\mathbf{r}) + \mu_{amf}(\mathbf{r}) \right] \Phi_m(\mathbf{r},\omega) \\ = \phi\mu_{axf}(\mathbf{r}) \frac{1+i\omega\tau}{1+[\omega\tau]^2} \Phi_x(\mathbf{r},\omega). \end{aligned} \quad (4.2)$$

Equation (4.1) describes the propagation of excitation light (subscript ‘x’) inside the tissue medium, whereas Eq. (4.2) describes the generation as well as the propagation of the emission light (subscript ‘m’). Here ω is the modulation frequency of the NIR source (rad/s); $D_{x,m}$ is the photon diffusion coefficient (cm) at excitation/emission wavelengths at position \mathbf{r} ; c is the speed of light in the medium (cm/s); $\Phi_{x,m}(\mathbf{r},\omega)$ is the complex excitation/emission fluence rate ($photons/(cm^2s)$) at position \mathbf{r} ; $S(\mathbf{r},\omega)$ is the

photon source strength ($photons/(cm^3s)$) at position \mathbf{r} ; ϕ is fluorescence quantum; and τ is fluorescence lifetime (s). Symbol $\mu_{ax,mi}$ denotes the absorption due to endogenous chromophores in the tissue; and $\mu_{ax,mf}$ denotes the absorption due to the exogenous fluorophores, which represent the only source of emission light from tissue. The diffusion coefficient is given by:

$$D_{x,m} = \frac{1}{3(\mu_{ax,mi} + \mu_{ax,mf} + \mu_{sx,m}(1-g))}, \quad (4.3)$$

where $\mu_{sx,m}$ denotes the scattering coefficients at excitation/emission wavelength; and g is the coefficient of anisotropy of the medium. Collectively, the terms μ_{axi} , μ_{ami} , μ_{sx} , and μ_{sm} are referred to as *endogenous optical properties*; and, μ_{axf} and μ_{amf} as *exogenous optical properties*. The coupled diffusion equations are solved with the Robin type boundary conditions:⁸⁴

$$2D_{x,m} \frac{\partial \Phi_{x,m}}{\partial \perp} + \gamma \Phi_{x,m} = 0, \quad (4.4)$$

where \perp denotes the normal direction outward to the surface, and γ is a constant depending upon the optical refractive index mismatch at the boundary. Equation (4.1), (4.2), and (4.4) can be solved numerically to yield,

$$\Phi_{x,m} = I_{AC_{x,m}} e^{-i\theta_{x,m}}, \quad (4.5)$$

where $\theta_{x,m}$ is the measured phase lag and $I_{AC_{x,m}}$ is the measured amplitude of the photon density wave at the excitation/emission wavelengths. The background tissue optical properties and values of the other parameters involved in Eq. (4.1) through (4.4) are

listed in Table 4.1, and are similar to those used in Section 3. Herein, we chose the excitation and emission wavelengths to correspond to Cardio-Green as a typical fluorophore used in imaging agent development.

For notational convenience, the process of imaging is often represented by the *imaging equation*

$$\mathbf{g} = \mathbf{H}(\mathbf{f}) + \mathbf{n}, \quad (4.6)$$

where \mathbf{f} is the object being imaged; \mathbf{H} is the imaging operator that describes how the imaging system maps the object into a vector of discrete measurements \mathbf{g} ; and \mathbf{n} is the vector of noise in the measurement system. A Galerkin-type finite element method (FEM) is employed to solve Eq. (1), (2), and (4) over a breast-shaped geometry described in Fig. 4.1 and used in the prior experimental work in our laboratory.¹⁰ The formulations in Eq. (1) through (5) are discretized for FEM representation and can be represented by Eq. (6). Accordingly, the nonlinear operator \mathbf{H} is provided by the finite element representation of coupled diffusion equations described in Eq. (1) and (2); \mathbf{f} is a vector containing the spatial values of the optical parameters to be imaged (in our case, the absorption coefficient owing to exogenous fluorophore, $\mu_{ax,mf}$) at each discrete point within the domain of breast geometry; and \mathbf{g} is a vector containing the measurements of light intensity (I_{AC}) and phase lag (θ) at the specified boundary locations (denoted as detector points in Fig. 4.2). The only source of fluorescence is due to the exogenous fluorophore. From Eq. (4.6), one can see that vector \mathbf{g} is the “noisy” image data returned by the imaging system. In this simulation study, the vector \mathbf{g} is obtained by adding the FEM solution of the coupled diffusion equations to the noise modeled from experimental

errors and considerations. The various noise considered in the imaging system is described in Section 4.2.3.2.

Table 4.1 Average background optical properties. The parameters used to solve the coupled diffusion equations are also tabulated.

wavelength↓	μ_{ai} ,	μ_s ,	μ_{af} ,	ω ,	c ,	g ,	ϕ ,	τ ,
	[cm ⁻¹]	[cm ⁻¹]	[cm ⁻¹]	[rad/s]	[cm/s]	[]	[]	[s]
excitation (780 nm)	0.02483	108.792	0.00299	6.28e8	2.25e10	0.9	.016	0.56e-9
emission (830 nm)	0.0322	98.241	0.000506					

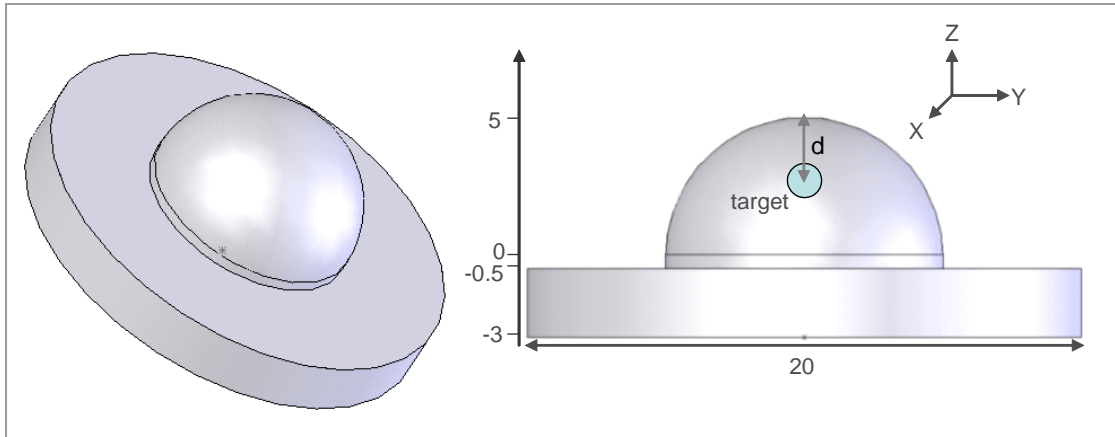


Fig. 4.1 The breast-shaped geometry consisting of a 10 cm diameter hemispherical top to simulate a human breast. The bottom cylindrical base has 20 cm diameter and is 2.5 cm high. Also shown is 1 cm³ target at a depth d. All dimensions are in centimeters.

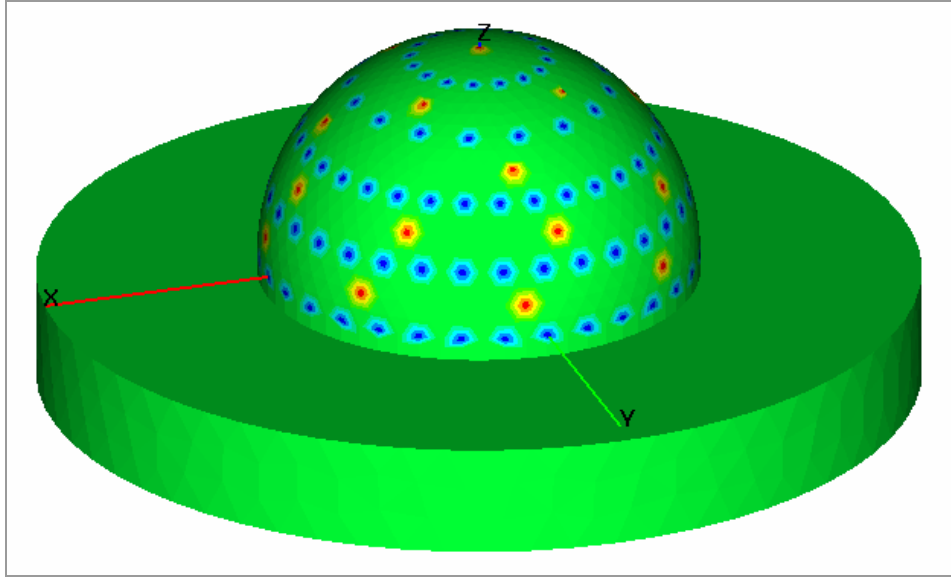


Fig. 4.2 The locations of the point sources and detectors on the breast-shaped geometry. The red points denote the sources and the blue points denote the detectors.

4.2.2 Simulated background heterogeneity

The lumpy-object model¹² is employed to simulate the non-specific distribution of the fluorescent agent as well as the heterogeneity of the endogenous tissue optical properties due to the natural anatomical structure. Lumpy backgrounds consist of single structures or “blobs” located randomly within the domain. Mathematically, these structures are represented by:

$$b(\mathbf{r}) = b_0 + \sum_{n=1}^{N_p} \text{lump}(\mathbf{r} - \mathbf{r}_n | l_0, w), \quad (4.7)$$

where $b(\mathbf{r})$ is the lumpy background; b_0 is the spatial mean of the lumpy background; N_p is the number of lumps; and \mathbf{r}_n is the uniformly distributed location of n th lump. The function *lump* has the following form:

$$lump(\mathbf{r} - \mathbf{r}_n) = l_0 \exp\left(\frac{-\|\mathbf{r} - \mathbf{r}_n\|^2}{2w^2}\right) - \frac{1}{V(\Omega)} \int_{\Omega} l_0 \exp\left(\frac{-\|\mathbf{r} - \mathbf{r}_n\|^2}{2w^2}\right) d^3\mathbf{r}. \quad (4.8)$$

In this expression, l_0 is the lump strength; w is the lump width; Ω is the domain; and $V(\Omega)$ is the volume of the domain. The volume integral term in Eq. (4.8) is designed such that the mean of function *lump* is zero; making the mean of the lumpy background equal to b_0 .⁴⁵ This makes lumpy-object model useful for fluorescence imaging, because it enables user to specify an average value of any optical property and then introduce perturbations in that optical property using lumpy-objects to simulate the behavior of the natural biological tissue. This is also relevant because the average optical properties of human breast tissues are widely reported in the literature (see for review Table 3.1 in Section 3).

In Section 3, the evaluation of the volume integral term in Eq. (4.8) was performed using Simpson's quadrature based numerical integration technique and required ~40 min of CPU time for each lumpy background. This approach is not feasible for the present study and hence we have used a far less time consuming approach based on the trapezoidal rule to evaluate the volume integral term in this section.

In order to implement lumpy backgrounds and to solve the coupled diffusion equations using FEM, the breast geometry is discretized into 34413 regular tetrahedral elements comprising a total of 6956 nodes. The lump strength, l_0 , is set to be a prescribed percentage of the mean background value b_0 . The lump spread, w , and the number of lumps, N_p , are set to be 5 mm and 100 respectively. While other works have

used a Poisson distribution of lumps to represent non-uniform distribution of nuclear imaging agents,^{85, 86} we chose a fixed number of lumps owing to our rationale to mimic heterogeneous tissue structure. The domain Ω in Eq. (8) is taken to be the hemispherical portion of the breast geometry shown in Fig. 4.1. For instance, 5% lumpy background of the scattering coefficient, μ_{sx} , indicates that 100 lumps are placed at locations uniformly distributed within the hemispherical portion of the breast geometry each having a strength 0.05 times the spatial average of μ_{sx} and a spatial spread of 5 mm. The process of generating lumpy background in an optical property at one wavelength and how it relates to the values at another wavelength is detailed in Section 3 and has been followed in this section. It is noteworthy that lump strengths that are less than or equal to 100% were assigned, thereby removing the possibility of negative optical property values. While there are other models, like clustered lumpy-object model which can describe anatomical heterogeneity,⁸⁵ in this first work, we examine the simplest, which is the lumpy-object model. Anatomical tissue structure representation using the clustered lumpy-object model is one of the motivations of our future research work.

The generation of the optical property heterogeneity map and the solution of the coupled diffusion equations were performed on a LINUX workstation with AMD Opteron 250 (2.4 GHz) and 4.0 GB RAM. Twenty five points for illumination and 128 points for collection are employed on the breast geometry to generate the complex solution of the coupled diffusion equations. Figure 4.2 illustrates one view of the illumination and collection points on the breast geometry.

4.2.3 Experimental conditions

This section describes the systematic errors and noise associated with the instrumentation of a fluorescence-enhanced optical imaging system.

4.2.3.1 Excitation light leakage

Figure 4.3 describes a typical experimental setup used in our laboratory for imaging studies on phantoms mimicking the shape and average optical properties of the human breast.^{10, 87} It includes: (1) a gain-modulated image intensifier; (2) a 16-bit cooled charged-coupled device (CCD) camera; and (3) a modulated laser diode. The phantom is illuminated by the modulated excitation light delivered at discrete points on the surface by fiber optics and the emission light is collected from fiber optics and delivered to the intensified CCD camera for measurement. The collected light at the phantom surface is a mixture of both emission as well as excitation light. Since only the emission light is desired, a scheme to reject the excitation light is often employed. For this purpose in our laboratory, an 830-nm band-pass filter and a holographic filter are used to reject 785-nm excitation light and to selectively pass 830-nm emission light. The performance of a filter is quantified by the optical density (OD),

$$OD_{\lambda} = -\log_{10} T = \log_{10} \left(\frac{I}{I_0} \right). \quad (4.9)$$

Subscript λ denotes the dependence of OD on the wavelength of the light; T is the transmittance; I_0 is the intensity of the incident light; and I is the intensity of the transmitted light. Equation (4.9) shows that the higher the OD, the lower the

transmittance. The performance of the filters decreases when the angle of incidence of light deviates from zero. The filter specifications and OD values as a function of incident angle for emission and excitation light are given elsewhere.⁸⁷

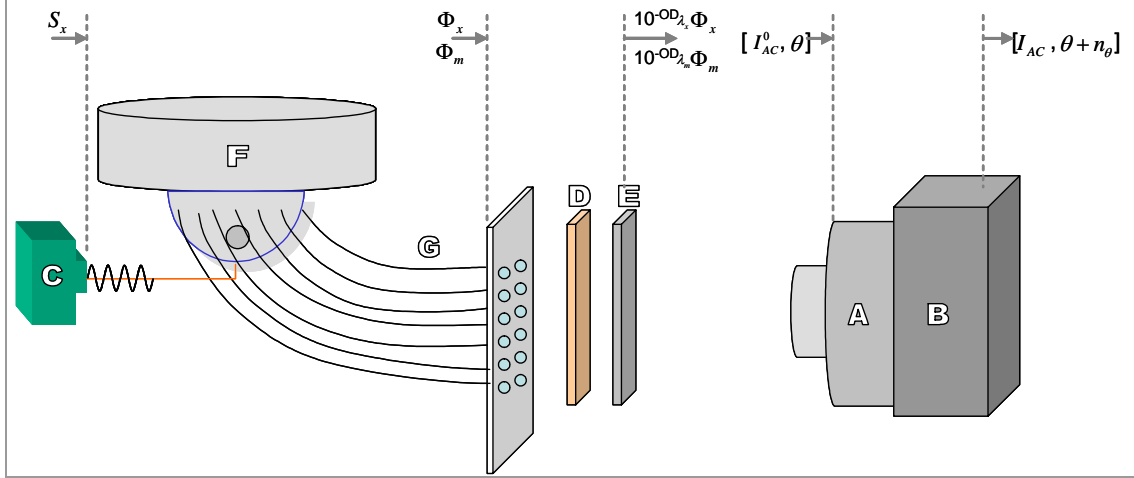


Fig. 4.3 Schematic of the experimental setup. The various components are labeled to describe: (A) a gain-modulated image intensifier, (B) a 16-bit cooled CCD camera, (C) a modulated laser diode used as a light source, (D) an 830-nm band pass filter, (E) a holographic notch filter, (F) the breast shaped phantom, and (G) the detector fibers leading to an interfacing plate. The Figure is not to scale.

It is noteworthy that the complete elimination of the excitation light from measurement of emission at the tissue boundary is not possible. The presence of a small amount of excitation light in the detected light is termed as excitation light leakage, and is a source of *error* in the imaging data set. Therefore the detected light is a mixture of the emission light and the excitation light which “leaks” through the filters. The overall intensity and phase of the detected light is thus affected by the excitation light leakage, and is obtained by adding the transmitted emission and excitation photon density waves, *i.e.* Φ_x and Φ_m . Accordingly, if the emission and excitation photon density waves at

the collection points are given by $y_m = I_m \sin(\omega t + \theta_m)$, and $y_x = I_x \sin(\omega t + \theta_x)$, respectively, then the overall photon density wave transmitted through filters is given by

$$y = 10^{-OD_{\lambda_m}} y_m + 10^{-OD_{\lambda_x}} y_x = I \sin(\omega t + \theta), \quad (4.10)$$

where

$$I = \left(10^{-2OD_{\lambda_m}} I_m^2 + 10^{-2OD_{\lambda_x}} I_x^2 + 2 \times 10^{-(OD_{\lambda_m} + OD_{\lambda_x})} I_m I_x \cos(\theta_m - \theta_x) \right)^{1/2} \quad (4.11)$$

$$\theta = \arctan \left(\frac{10^{-OD_{\lambda_m}} I_m \sin \theta_m + 10^{-OD_{\lambda_x}} I_x \sin \theta_x}{10^{-OD_{\lambda_m}} I_m \cos \theta_m + 10^{-OD_{\lambda_x}} I_x \cos \theta_x} \right). \quad (4.12)$$

Here OD_{λ_m} and OD_{λ_x} are the OD values of the filters for emission and excitation wavelengths, respectively.

The OD values of 0.3009 for emission light and 5.8470 for excitation light are taken for 830-nm band pass filter; whereas an OD value of 6 for the excitation light is taken for holographic filter.⁸⁷ The angle of incidence is assumed to be 0° while determining the above OD values. Zero degree incident angles can be achieved by allowing the fiber delivered light to pass through a GRIN lens before it arrives at the filters,⁸⁸ or collimating the imaged plane before passing through the image quality filters.⁸⁷

In this study, the effect of using different filter efficiencies on the detection performance of the imaging system is studied. For this purpose, we simulated excitation light rejection with OD values varying from 3 to 7, simulating the range of ODs used in studies found in the literature and the potential deterioration of filter performance owing to the non-normal incidence of collected light.

4.2.3.2 Noise

In optical imaging systems, two main types of fundamental noise[†] are *thermal* and *quantum* noise. The thermal noise is a result of the random fluctuations in the current due to the thermal (Brownian) motion of charge carriers in any conductor. This is also known as *dark current*. An example of dark current in the CCD system occurs when the thermal fluctuations in the CCD material releases electrons, which contribute to the overall number of photoelectrons. Similarly, the randomness incurring in the optical image measurements due to the counting of random arrival of photons is responsible for quantum noise. Both types of noise follow Poisson distribution and are often non-additive.^{44, 89}

Amplification and *quantization* noise are the specific types of non-fundamental noise[‡] in an optical imaging system. In any intensified CCD detector system, the random conversion of electrons to light gives rise to amplification noise. Quantization noise, however, is an inherent noise in the amplitude quantization process and occurs due to the finite resolution of the analog-to-digital converters (ADC). Both types of noise are additive and, in particular, amplification noise has a Gaussian distribution.⁴⁴

Imaging systems typically consist of many components which individually give rise to the noise in the measurement. Thus the resulting noise becomes too complex to be described by a single form of distribution. In most cases, researchers are forced to choose between one of these assumptions: (1) the noise from one particular component is dominant over that of other sources, and thus can be neglected; or (2) the noise

[†] Referring to the corpuscular nature of light

[‡] Arising from the instrumentation of the system

associated with different components of the imaging system are additive, in which case the overall noise becomes Gaussian due to the central limit theorem. Therefore, the actual experimental setup (see Fig. 4.3) and the noise associated with its various components are analyzed to make proper assumption about the distribution of the overall noise. The CCD camera used in our laboratory has a regulated temperature control that keeps the chip temperature to as low as -41°C . At such low temperature, the typical dark current of the CCD is in the order of 0.1 electrons per pixel per second (e/p/s) of the exposure time. An exposure time of 400 ms further ensures that the dark current noise in the measurements is negligible. Hence the noise of the detector system is mainly governed by the image intensifier.^{90, 91} The image intensifier contains a wavelength specific photocathode, a micro channel plate (MCP), and a phosphor screen. The random striking of photons to the photocathode is the source of quantum noise. As this occurs before the amplification process, the noise becomes amplified in the MCP. In addition, the multiplication (gain) of electrons in the MCP introduces amplification error. These two noises are assumed to be additive, so that the cumulative noise of the image intensifier is Gaussian due to the central limit theorem. Since the quantum noise is dependent upon signal*, the overall noise is also assumed to be signal-dependent. Thus the standard Gaussian noise with variance dependent upon the intensity of the light is used. Specifically, we add 5% Gaussian noise to the detected light (coming through the filters), so that final measured intensity is given by:

* In this context, the word “signal” means “the object being measured”, unlike “the object being detected” in the target detection tasks.

$$I_{AC} = I_{AC}^0 (1.0 + 0.05 \times \mathbb{N}(0,1)), \quad (4.13)$$

where I_{AC}^0 is the intensity of the light before it enters the image intensifier; and $\mathbb{N}(0,1)$ denotes a Gaussian distribution with zero mean and unit variance.

In contrast, a model to describe the noise in the phase measurements is not as simple. Therefore a typical experiment in our laboratory has been compared with the simulation, which shows that the noise in phase measurements follows approximately a uniform random distribution. Consequently, a random value in the interval $(-2^\circ, +2^\circ)$ has been considered as the conservative noise estimate in the phase measurements. Mathematically, this noise can be described by:

$$n_\theta = 4^\circ \times (\xi - 0.5), \quad (4.14)$$

where ξ is a uniformly distributed random number in $[0, 1]$. The noise, n_θ , is added to the phase of detected light, which is a mixture of both emission and excitation photon density waves, to obtain the noisy estimate of phase measurements.

4.2.4 Detection tasks

For detection tasks, there are two mutually exclusive hypotheses possible: (i) the signal-present hypothesis (H_1) where the measurements are made from a patient/phantom with a target (\mathbf{t}); and (ii) the signal-absent hypothesis (H_0) where patient/phantom contains no target.

$$H_1 : \quad \mathbf{g} = \mathbf{H}(\mathbf{f} + \mathbf{t}) + \mathbf{n} \quad (4.15)$$

$$H_0 : \quad \mathbf{g} = \mathbf{H}(\mathbf{f}) + \mathbf{n}. \quad (4.16)$$

Here $\mathbf{g} = I_{AC} \exp(-i\theta)$ as described in Eq. (4.5); \mathbf{f} represents the normal, non-target portion of the anatomy, while \mathbf{t} represents the target (signal) portion. Both \mathbf{f} and \mathbf{t} are stochastic in real situations and vary from patient to patient. In the case of fluorescence imaging, the stochastic nature in \mathbf{f} arises from both the non-specific fluorophore deposition as well as the heterogeneity of the endogenous tissue optical properties due to the natural anatomical structure. The stochastic nature of \mathbf{f} is modeled using lumpy-objects as described in the previous section. This study involves “signal-known exactly” (SKE) cases wherein the size and location of target is known, and so the stochastic nature of \mathbf{t} is not considered.

The target is taken to be a spherical volume of 1 cm^3 centered in z-axis of the geometry shown in Fig. 4.1. The fluorescent uptake of the target is considered to be 10 times higher than the average background uptake, which means that its μ_{axf} and μ_{amf} values are 10 times greater than the corresponding average background values. Five locations of the target are considered at depths varying from 1 cm to 5 cm . The depth of the target is measured as the distance between the tip of the hemispherical portion of the breast geometry (coordinates: 0, 0, 5) and the center of the spherical target volume.

4.2.4.1 Hotelling observer

The Hotelling observer is a linear discriminant that computes the confidence level using only the linear manipulations on the measurement data.⁴⁴ Its test statistic is given by the equation:

$$\chi_{Hot}(\mathbf{g}) = \Delta \bar{\mathbf{g}}^T \mathbf{K}_g^{-1} \mathbf{g}, \quad (4.17)$$

where $\Delta\bar{\mathbf{g}}$ is the vector difference in the means of the vectors of discrete measurements under the H_1 and H_0 hypotheses; \mathbf{K}_g is the average covariance of the vector \mathbf{g} (assumed to be the same under each hypothesis); and superscript T denotes the transpose of the matrix. Mathematically, $\mathbf{K}_g = \left\langle (\mathbf{g} - \langle \mathbf{g} \rangle_{n,f})(\mathbf{g} - \langle \mathbf{g} \rangle_{n,f})^T \right\rangle_{n,f}$, where $\langle \dots \rangle_{n,f}$ denotes average over all noise, \mathbf{n} , and object variations, \mathbf{f} . While the covariance matrix maybe different under H_1 and H_0 hypotheses, we assume that for a weak fluorescent signal, it is the same.⁴⁴

The Hotelling observer is called an *optimal* linear observer because it maximizes a measure of separability between the two hypotheses, namely the target-present (H_1) and target-absent (H_0). The degree of overlap of the density functions of the Hotelling test statistic, $\chi_{Hot}(\mathbf{g})$, determines the separability of the two hypotheses. As the degree of the overlap increases, the detectability of the target decreases. The SNR associated with the Hotelling test statistic is a measure of this overlap, and is given by the following expression:

$$SNR_{Hot}^2 = \Delta\bar{\mathbf{g}}^T \mathbf{K}_g^{-1} \Delta\bar{\mathbf{g}}. \quad (4.18)$$

Thus, the higher the value of the SNR_{Hot} , the higher the separability between the two hypotheses, and the lower the overlap of the density functions of $\chi_{Hot}(\mathbf{g})$ under the two hypotheses. A higher value of the SNR_{Hot} corresponds to improved detectability of the target.

In both Eq. (4.17) and (4.18), the calculation of the average covariance matrix, \mathbf{K}_g , is dependent upon the size of the measurement data sample. Sample size should be

large enough to ensure a well conditioned covariance matrix, so that the inverse of the matrix, \mathbf{K}_g^{-1} , is stable.⁹² Decomposition of \mathbf{K}_g into two terms, one representing the stochastic nature of \mathbf{f} and the other the noise in the system,¹⁴ improves its conditioning even when large numbers of \mathbf{g} are not available. The decomposition approach is used to estimate the overall covariance matrix, \mathbf{K}_g , as

$$\mathbf{K}_g = \mathbf{K}_{\bar{g}} + \bar{\mathbf{K}}_n \quad (4.19)$$

The first term, $\mathbf{K}_{\bar{g}}$, is average-data covariance matrix, and the second term, $\bar{\mathbf{K}}_n$, is average noise-covariance matrix. The two matrices are respectively given by $\mathbf{K}_{\bar{g}} = \left\langle \left(\langle \mathbf{g} \rangle_{n|f} - \langle \mathbf{g} \rangle_{n,f} \right) \left(\langle \mathbf{g} \rangle_{n|f} - \langle \mathbf{g} \rangle_{n,f} \right)^T \right\rangle$, and $\bar{\mathbf{K}}_n = \langle \mathbf{nn}^T \rangle_{n,f}$, where \mathbf{nn}^T denotes the tensor product of \mathbf{n} with itself. The advantage of this decomposition is that $\bar{\mathbf{K}}_n$ is usually diagonal and thus improves the conditioning of the overall covariance matrix, \mathbf{K}_g .

4.2.5 Simulated measurements

As shown in Fig. 4.2, twenty five illumination and 128 collection points are used to obtain the boundary measurements of excitation/emission photon density wave amplitude ($I_{AC_{x,m}}$) and phase delay ($\theta_{x,m}$) by solving the coupled diffusion equations. The vector \mathbf{g} has a dimension of 3200×1 for both intensity and phase measurements. The overall covariance matrix, \mathbf{K}_g , has a dimension of 3200×3200 . In order to obtain a reasonable estimate of \mathbf{K}_g , 7000 measurement data sets (see Appendix C) were generated under both hypotheses (target-present and target-absent) using the lumpy backgrounds as described in Section 4.2.2. Noise computed by Eq. (4.13) and (4.14) were then added to

\mathbf{g} to evaluate the influence of noise. A Gaussian elimination method was used to compute the inverse of matrix $\mathbf{K}_{\mathbf{g}}$. It should be noted that $\mathbf{K}_{\mathbf{g}}$ for a homogeneous background case becomes a null matrix, so we only considered $\bar{\mathbf{K}}_{\mathbf{n}}$ when calculating $\mathbf{K}_{\mathbf{g}}$ for such cases.

The calculations of SNR_{Hot} values were performed on a LINUX workstation with AMD Opteron 285 (2.6 GHz) and 8.0 GB RAM. The SNR_{Hot} was then used to quantify the detection capability of the imaging system and to assess how target detection task is affected by (i) strength of lumpy backgrounds, (ii) target depth, and (iii) filter performance in rejecting excitation light.

4.3 Results

The 7000 imaging data vectors, \mathbf{g} , required ~ 94 hrs of CPU time to simulate target-present and target-absent cases. Additionally, the algorithm to compute the SNR_{Hot} value required ~ 2 hrs of CPU time.

An example distribution of μ_{axi} , μ_{sx} , and μ_{axf} for the hundred percent endogenous and exogenous lumps in the background is illustrated in Fig. 4.4(a) through 4.4(c). The lumpy backgrounds for other lump strengths are not shown here for brevity.

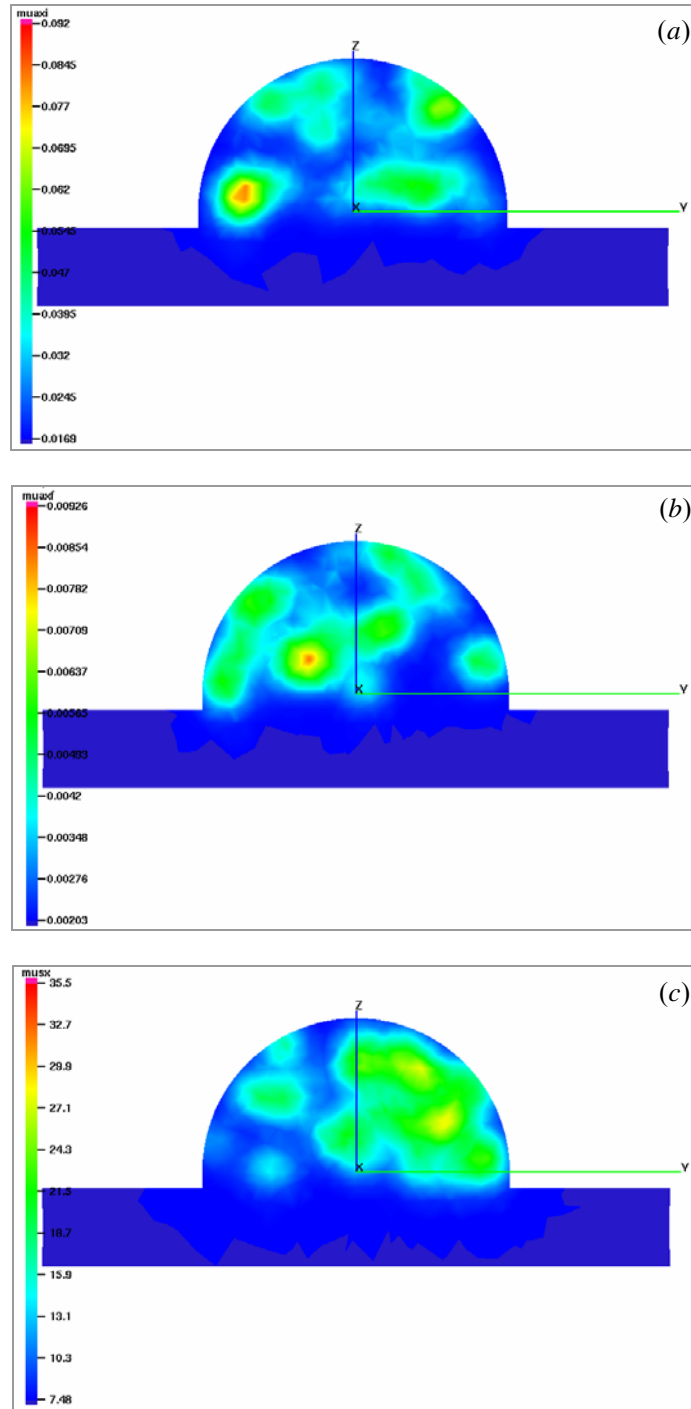


Fig. 4.4 Lumpy backgrounds of endogenous and exogenous optical properties using Lumpy object model. The lumps in μ_{axi} , μ_{sx} , and μ_{axf} are shown as cutplanes to the breast geometry (Fig. 4.1) parallel to yz-plane and passing through $x=-1$ cm. In each case, one hundred lumps are uniformly generated in the hemispherical volume with spatial spreads of 5 mm and strength values equal to hundred percent of the average background values of optical properties as given in Table 4.1.

4.3.1 Influence of lump strength

The detectability (SNR_{Hot}) of the fluorescent target superimposed in the lumpy backgrounds of endogenous and exogenous optical properties at a depth of 1 *cm* was first examined as a function of lump strength. Figure 4.5 illustrates how SNR_{Hot} of intensity (I_{AC}) and phase (θ) measurements wanes as a function of the lump strength of (a) endogenous optical properties, and (b) endogenous as well as exogenous optical properties. Both Figures show that the majority of the information is contained by intensity measurements, portrayed by the higher SNR_{Hot} values of intensity measurements than phase measurements. In both Figures, the SNR_{Hot} of intensity and phase measurements decrease as the lump strength increases. The decrease in SNR_{Hot} with increasing endogenous lump strengths indicates that endogenous lumps do affect the detectability of the target. This partially answers our concern in Section 3 we showed single cases of tomographically reconstructed images and advocated the need to use sufficiently large imaging data in order to better understand the effect of lumpy backgrounds on target detection tasks. Eppstein *et al.*⁷³ have also reported difficulty in detecting a target when background variations in endogenous optical properties exceed a specific range. Similarly, the overall decrease in the information of both intensity and phase measurements as endogenous-and-exogenous lump strength increases is consistent with our previous study regarding the sensitivity of the detection performance on uneven distribution of disease markers in the background (see Section 3). Indeed, when lumpy backgrounds in exogenous properties are added to an already heterogeneous background in endogenous properties, the information content is expectedly reduced. Nonetheless,

in both cases of a heterogeneous anatomical backgrounds alone and of the addition of non-uniform background distribution of fluorescent contrast agent in a heterogeneous anatomical background, a large sample of reconstructed images may provide further insight into the effect of lumpy backgrounds on detection tasks

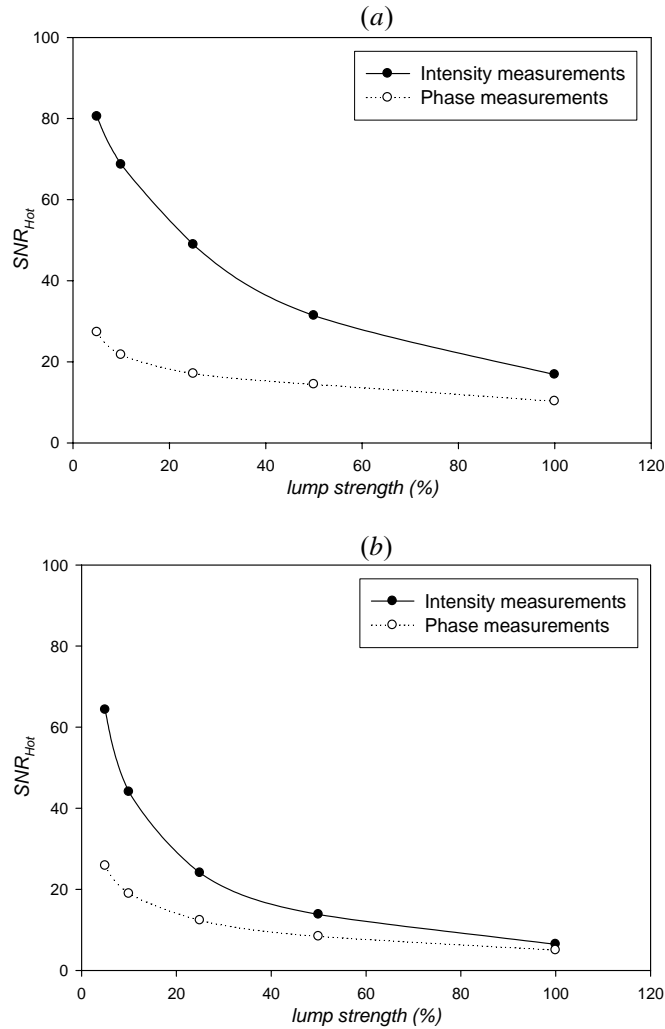


Fig. 4.5 SNR_{Hot} computed from simulated measurements of light intensity (filled circles) and phase (open circles) as a function of strength of lumps in (a) the endogenous optical properties, and (b) endogenous as well as exogenous optical properties vs. the strength of lumps. The target is a 1 cm^3 spherical volume at a depth of 1 cm and contrasted from its surroundings by 10:1. The centroid of the target is at $(0, 0, 4)$ inside the breast geometry (Fig. 4.1).

4.3.2 Influence of target depth

Figure 4.6 illustrates the plots of SNR_{Hot} with target depths varying from 1 *cm* to 5 *cm* in homogeneous backgrounds of the optical properties (*i.e.* the background optical properties have no spatial variations and are equal to the average values given in Table 4.1). The plots show that the SNR_{Hot} for both intensity and phase measurements decreases as the target depth increases with intensity measurements providing more information as evident from higher SNR_{Hot} . However, the SNR_{Hot} does not follow this trend in the presence of heterogeneous backgrounds as shown in Fig. 4.7 which illustrates SNR_{Hot} versus target depth in the presence of lumpy backgrounds of endogenous as well as exogenous optical properties with hundred percent lump strengths. Figure 4.7 shows that the phase measurements contain more information (*i.e.* higher values of SNR_{Hot}) than the intensity measurements when depth is greater than ~ 1.5 *cm*. This indicates the importance of phase measurements in the fluorescence-enhanced imaging when the target is embedded deep within the tissue. However, it is not our intention to establish a general statement based exclusively on this result, and further investigations, including experimental validation, are needed. We have verified that the increase in SNR_{Hot} illustrated in Fig. 4.7 as the target depth increases from 4 to 5 *cm* is not due to mesh discretization levels, but more likely due to the increased signal from more detectors as the target is probed by more detectors in the hemispherical geometry. The increase in SNR_{Hot} of amplitude and phase measurements with target depth is consistent in our studies (see below in Fig. 4.8).

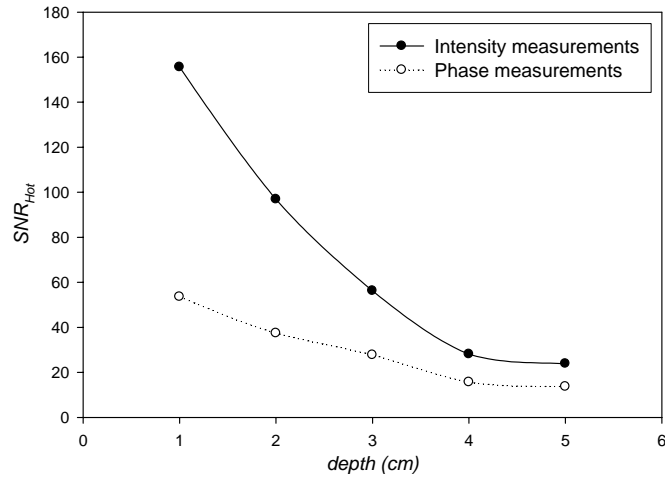


Fig. 4.6 SNR_{Hot} computed from simulated measurements of light intensity (filled circles) and phase (open circles) in homogeneous background of optical properties vs. the depth of 1 cm^3 spherical target contrasted from its surroundings by 10:1. The centroid of the target lies in the z-axis of breast geometry (Fig. 4.1). The target depth is measured as the distance from its centroid to the point (0, 0, 5) in breast geometry.

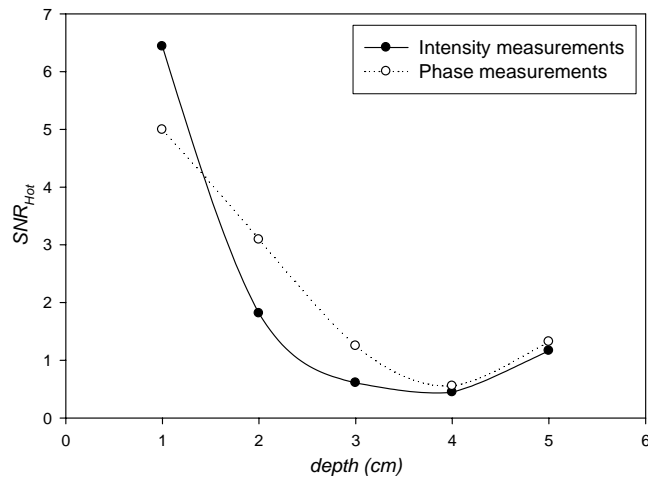


Fig. 4.7 SNR_{Hot} computed from simulated measurements of light intensity (filled circles) and phase (open circles) in hundred percent lumpy backgrounds of endogenous (μ_{axi} , μ_{ami} , μ_{ax} , and μ_{am}) as well as exogenous (μ_{axf} , and μ_{amf}) optical properties vs. the depth of 1 cm^3 spherical target contrasted from its surroundings by 10:1. The centroid of the target lies in the z-axis of breast geometry (Fig. 4.1). The target depth is measured as the distance from its centroid to the point (0, 0, 5) in breast geometry.

4.3.3 Influence of excitation light rejection efficiency

Figure 4.8 illustrates the changes in the SNR_{Hot} of (a) intensity and (b) phase measurements with varying target depths for increasing OD values. The target is present in lumpy backgrounds of both endogenous and exogenous optical properties with one hundred percent lump strengths. As anticipated, the SNR_{Hot} improves for all target depths as the OD value increases, a result of more efficient excitation light rejection. Surprisingly, the SNR_{Hot} becomes insensitive to OD when $OD \geq 5$ at all target depths. This result maybe reasonable when the emission fluence is greater than the excitation fluence so that the ‘leakage’ is not the dominant noise factor in heterogeneous backgrounds. However, as the background heterogeneity decreases, we might expect higher SNR_{Hot} with increased filter performance. Overall, the Hotelling analysis provides an important tool to optimize quality of the filters used in the imaging system under realistic situations.

4.4 Discussion

Most imaging modalities typically involve phantom studies as the first step before the clinical trials.⁹³⁻⁹⁵ Phantom studies are used as a verification for the validity of the imaging method. In fluorescence-enhanced optical imaging, phantom studies that incorporate optical properties variations representative of heterogeneous tissue structure is a difficult task given that the anatomical structure of one patient is randomly different from another. Specifically, the optical properties of a tissue medium are characterized by the absorption and scattering coefficients. The absorption coefficient is a measure of

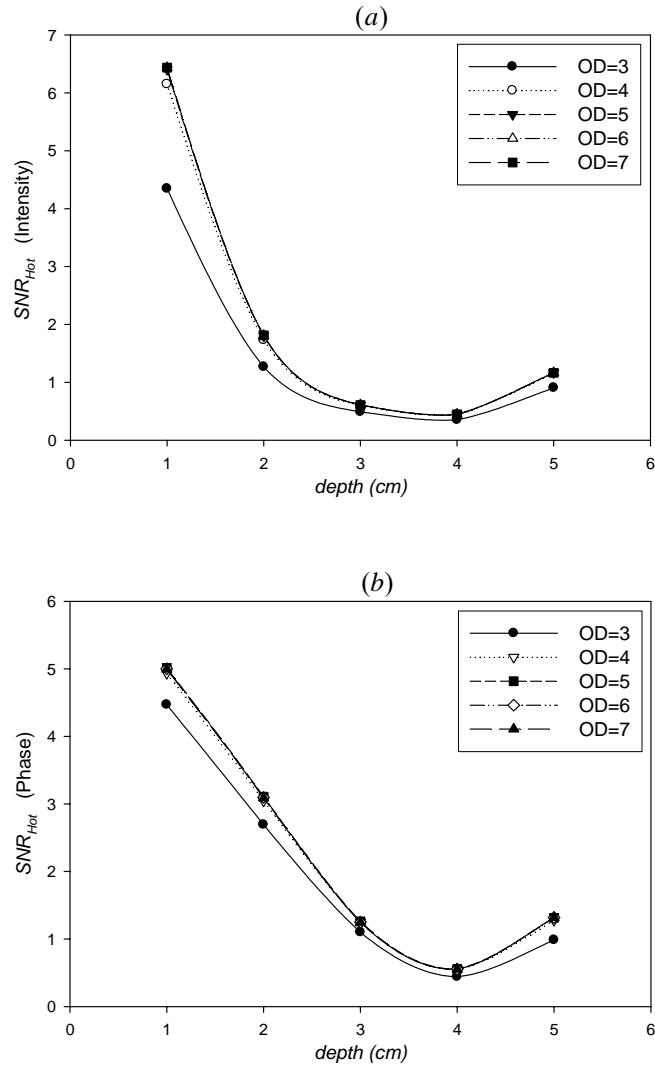


Fig 4.8 SNR_{Hot} computed from simulated measurements of (a) intensity, I_{AC} , and (b) phase, θ , in one hundred percent lumpy backgrounds of endogenous as well as exogenous optical properties vs. the depth of 1 cm^3 spherical target contrasted from its surroundings by 10:1. The centroid of the target lies in the z-axis and the target depth is measured as the distance from its centroid to the point (0, 0, 5) in breast geometry (Fig. 4.1). The various plots show the affect of varying optical densities (OD) of the excitation light rejection filter.

the amount of light *absorbed* by: (i) oxy- and deoxy-hemoglobin in the blood flowing through blood capillaries, (ii) water retained in the tissue, and (iii) lipids present in the cell membrane.⁶⁵ The scattering coefficient is a measure of the amount of light *scattered* due to the refractive index mismatch between the extracellular and intracellular compartments in a tissue. These tissue properties affect the absorption and scattering of light in a tissue and vary spatially. The same may be said about the distribution of molecularly targeting, NIR fluorescent contrast agents. Heterogeneous distribution of imaging agent will depend upon the level of expression of the marker not only in the diseased target tissue, but also in the surrounding normal tissue.

The performance of an imaging system can be characterized by how an observer fares in the task of detecting a diseased target tissue. An observer, either a human or a computer algorithm, which performs the task of target detection, is specified; and the figures of merit to quantify the task performance are established.¹⁴⁻¹⁶ Human observers can be assessed using psychophysical studies and receiver operating characteristic (ROC) curve analysis,⁹⁶ but such studies do not separate the hardware from the reconstruction algorithms.⁵¹ Thus, to directly assess the quality of an imaging system, mathematical observers that employ only the raw measurements are used.⁹⁷ This technique has been successfully used in PET and SPECT imaging and allows the imaging hardware to be optimized independently while still using task performance as the guide. The next step in this process is to assess human performance using reconstructed images (see Section 5).

4.5 Conclusions

In brief, we have presented and demonstrated a method of evaluating fluorescence-enhanced optical imaging systems using task-based methods. Specifically, we have investigated the SKE cases where the location, shape and contrast of the target are assumed to be known. We employed the Hotelling observer to directly assess the target-detection-based information content of the imaging measurements. This analysis has led to quantitative comparisons of the performance of our imaging system at varying target depths, light-rejection filter properties, and background strengths. In addition, fluorescence-enhanced optical imaging has typically been evaluated using a target in a homogeneous background of optical properties. We have used the lumpy-object model to simulate patient variability which is known to adversely affect task performance in other modalities and, thus, should be accounted for in fluorescence-enhanced optical imaging. Description of the image-reconstruction algorithms is not within the scope of this paper. However, upon assuming the Hotelling observer is a reasonable surrogate for the Bayesian observer, we have shown that we can assess and potentially optimize our imaging hardware independently from the reconstruction algorithm.

Specifically, the Hotelling observer study demonstrates that the detectability of the target decreases substantially when the lumpy backgrounds are considered to simulate the anatomical structure and/or the heterogeneous distribution of the disease markers that may be targeted by fluorescent contrast agents. We have demonstrated the importance of phase-information when detecting targets that are deep within the tissue. Finally the performance of the Hotelling observer provides an important tool to optimize

the quality of the filters used in the imaging system. As a natural progression in the OAIQ, the next section addresses the performance of human observers using reconstructed images.

5. PSYCHOPHYSICAL ANALYSIS OF THE RECONSTRUCTED IMAGES BASED ON A GAUSS-NEWTON ALGORITHM*

5.1 Introduction

Due to the lack of sufficient clinical trials involving fluorescence-enhanced optical imaging modality, the classification studies using psychophysical tools and receiver operating characteristic (ROC) curves are not widely reported in the literature. The psychophysical studies of human observers for the task of non-invasive detection of a malignant lesion inside biological tissues is almost always established before a specific imaging modality is deemed task efficient and safe for clinical usage. For example, the diagnostic mammography method holds a vast amount of psychophysical data analyzing how radiologists perform the task of detecting a suspicious region using clinical x-ray images.⁹⁸⁻¹⁰⁴ Moreover, these analyses are often adduced in order to establish the validity of x-ray mammography as an efficient imaging modality for breast cancer diagnostics.¹⁰⁵⁻¹⁰⁸ Although x-ray mammography is a “clean” and robust imaging method, it is not capable of performing functional imaging, a key aspect of the newer developments in molecular imaging. Mammography is mainly capable of detecting calcification and masses, and thus it alone is usually unable to prove that an abnormal area is cancerous. Therefore, if mammography raises significant suspicion of cancer, then additional breast imaging or biopsy is often suggested before making final

* Parts of this section are adapted from the manuscript “Assessment of a fluorescence-enhanced optical imaging system through psychophysical analysis of simulated patient data” to be submitted to Optics Express (2006).

decisions. Fluorescence-enhanced optical imaging, on the other hand, has the functional imaging ability besides being a robust imaging modality suitable for breast imaging.¹⁰⁹⁻

¹¹¹ Functional imaging is a means of simultaneously quantifying the structural and functional aspects of a biological system, and hence it enables fluorescence imaging modality not only to detect the structural anomalies in breast tissues but also to understand the biological processes that led to such malignancies in the tissue. Thus, fluorescence imaging as a functional imaging modality provides experimental tools that address physiological questions of interest in a relatively noninvasive manner.

In the absence of clinical data, the present study employs a simulated approach to obtain breast imaging data corresponding to clinical patients, enabling assessment of fluorescence imaging via psychophysical tools. In this work, clinical conditions involved in imaging a patient's breast are accounted for in the simulation. A lumpy-object model¹² is used to simulate the anatomical structure associated with mammarian tissues, as well as the heterogeneous background expression of disease markers, and a human observer's performance in detecting a fluorescently labeled malignant lesion is analyzed in a "double-blinded" manner typical of clinical trials. A Gauss-Newton (GN) based tomographic imaging algorithm is used to obtain 3D images of the simulated patients' breast based on the boundary measurements of fluorescence emission.

The feasibility of image reconstruction in the presence of heterogeneous backgrounds represented by lumpy-object model was established in Section 3 through successful reconstruction of targets using a PMBF/CONTN algorithm. Our motivation in Section 3 was to examine whether a target superimposed in heterogeneous

backgrounds can at all be reconstructed, so that a decision about the applicability of OAIQ tools in our system could be arrived at. This is the reason why we examined only the single cases of reconstructed target in varying lumpy backgrounds. However, with the ability to reconstruct targets in heterogeneous backgrounds, we have investigated a large number of cases in this section so that the human observer performing target detection task can be analyzed using psychophysical tools. The GN based algorithm is utilized in this study as a replacement to the PMBF/CONTN algorithm so that a large number of reconstructions can be performed in feasible amount of time.

In the following Section 5.2, we present (i) a brief description of the image reconstruction algorithm used to make decisions about the presence of a fluorescent target; (ii) tools to perform psychophysical analysis for a fluorescence-enhanced optical imaging system; (iii) a description of how to obtain simulated data sets similar to the clinical breast imaging. In Section 5.3, we report how a human observer's performance is affected due to the variations in the tissue type and the non-uniform distribution of the disease markers in the background.

5.2 Methods

The assessment of an imaging system requires: (i) an imaging model describing how the measurements are obtained; (ii) a methodology to interpret imaging measurements vis-à-vis the observer detection task; and (iii) the OAIQ tools for observer performance evaluation. These components comprising the framework of image quality assessment are described in this section apropos of the fluorescence-enhanced optical imaging.

5.2.1 The imaging model and the reconstruction algorithm

As described in Section 2.2, the fluorescence imaging problem is typically solved in two steps: (i) a photon transport model is used to obtain *predicted* boundary fluorescence measurements for a given fluorescence absorption map (*the forward problem*); and (ii) an iterative scheme is used to successively generate the fluorescence absorption maps until the predicted boundary fluorescence measurements are within a specific tolerance when compared to the *actual* boundary fluorescence measurements (*the inverse problem*). As described in previous sections, the coupled diffusion equations accurately model the photon transport in large scattering media, such as biological tissues, and are mathematically represented by:

$$-\nabla \cdot [D_x \nabla \Phi_x] + \left[\frac{i\omega}{c} + \mu_{axi} + \mu_{axf} \right] \Phi_x = S_x \quad (5.1)$$

$$-\nabla \cdot [D_m \nabla \Phi_m] + \left[\frac{i\omega}{c} + \mu_{ami} + \mu_{amf} \right] \Phi_m = \phi \mu_{axf} \frac{1 + i\omega\tau}{1 + [\omega\tau]^2} \Phi_x, \quad (5.2)$$

Equation (5.1) describes the propagation of excitation light (subscript ‘x’), whereas Eq. (5.2) describes the generation as well as the propagation of the emission light (subscript ‘m’). Here ω is the modulation frequency of the NIR source; $D_{x,m}$ is the photon diffusion coefficient at excitation/emission wavelengths; c is the speed of light in the medium; $\Phi_{x,m}$ is the complex excitation/emission fluence rate; S_x is the excitation light source strength (*photons/(cm³s)*); ϕ is fluorescence quantum; and τ is fluorescence lifetime. Parameter $\mu_{ax,mi}$ denotes the absorption due to endogenous chromophores in the tissue; and $\mu_{ax,mf}$ denotes the absorption due to the exogenous fluorophores. The

diffusion coefficient is given by $D_{x,m} = 1/3(\mu_{ax,mi} + \mu_{ax,mf} + \mu_{sx,m}(1-g))$, where $\mu_{sx,m}$ denotes the scattering coefficients at excitation/emission wavelength and g is the coefficient of anisotropy of the medium. Collectively, the terms μ_{axi} , μ_{ami} , μ_{sx} , and μ_{sm} are referred to as *endogenous optical properties*; and, μ_{axf} and μ_{amf} as *exogenous optical properties*. The coupled diffusion equations are solved with the Robin type boundary conditions:⁸⁴

$$2D_{x,m} \frac{\partial \Phi_{x,m}}{\partial \perp} + \gamma \Phi_{x,m} = 0, \quad (5.3)$$

where \perp denotes the normal direction outward to the surface, and γ is a constant depending upon the optical refractive index mismatch at the boundary.

As previously described in Section 2.2.1, solving the coupled diffusion equations in (5.1) and (5.2) in a finite element framework is equivalent to solving the following system of linear equations simultaneously:

$$\underline{\mathbf{K}}_x \underline{\Phi}_x = \underline{\mathbf{S}}_x, \quad (5.4)$$

$$\underline{\mathbf{K}}_m \underline{\Phi}_m = \underline{\mathbf{B}}_{x \rightarrow m} \underline{\Phi}_x. \quad (5.5)$$

Here $\underline{\mathbf{K}}_x$ and $\underline{\mathbf{K}}_m$ are the elemental stiffness matrices; $\underline{\mathbf{S}}_x$ is the excitation source matrix; $\underline{\mathbf{B}}_{x \rightarrow m}$ is the coupling matrix. $\underline{\Phi}_x$ and $\underline{\Phi}_m$ are the vectors containing the nodal values of excitation and emission fluence, and so are $N \times 1$ vectors, N being the number of nodal points in the discretized solution domain. The goal of the fluorescence imaging problem is to reconstruct μ_{axf} from the boundary measurements of Φ_m . We use a Gauss-Newton based optimization method to solve the inverse problem. Along these

lines, the fluorescence image reconstruction is posed as an optimization problem wherein an L_2 norm based error between the experimentally *measured* fluence ($\underline{\Phi}_m^{meas}$) and the forward solver *calculated* fluence ($\underline{\Phi}_m^{calc}$) is sought to be minimized with respect to the optimization variable, μ_{axf} . The image reconstruction problem is written as:

$$\min_{\mu_{axf}} E_{\Phi_m} = \frac{1}{2} (\underline{\Phi}_m^{calc} - \underline{\Phi}_m^{meas})^* (\underline{\Phi}_m^{calc} - \underline{\Phi}_m^{meas}), \quad (5.6)$$

where superscript $*$ denotes the conjugate transpose of a vector; $\underline{\Phi}_m^{calc}$ and $\underline{\Phi}_m^{meas}$ are vectors of size M , the total number of boundary measurements. As previously described in Section 2.2.2, the iterative optimization scheme for a GN based algorithm is given by:

$$(\mu_{axf})_{k+1} = (\mu_{axf})_k - (\mathbf{J}_{E_{\Phi_m}}^* \mathbf{J}_{E_{\Phi_m}})^{-1} \mathbf{J}_{E_{\Phi_m}}, \quad (5.7)$$

where the subscript k denotes the iteration number; and the matrix $\mathbf{J}_{E_{\Phi_m}}$ is evaluated with the value of μ_{axf} at the k th iteration. In Eq. (5.7), matrix $\mathbf{J}_{E_{\Phi_m}}$ represents the Jacobian sensitivity matrix of the error function, E_{Φ_m} , and can be calculated as follows:

$$\begin{aligned} \mathbf{J}_{E_{\Phi_m}} &= \nabla_{\mu_{axf}} E_{\Phi_m} \\ &= \frac{\partial}{\partial \mu_{axf}} \left[\frac{1}{2} (\underline{\Phi}_m^{calc} - \underline{\Phi}_m^{meas})^* (\underline{\Phi}_m^{calc} - \underline{\Phi}_m^{meas}) \right] \\ &= \frac{\partial \underline{\Phi}_m^{calc}}{\partial \mu_{axf}} [\underline{\Phi}_m^{calc} - \underline{\Phi}_m^{meas}]. \end{aligned} \quad (5.8)$$

In Eq. (5.8), $\partial \underline{\Phi}_m^{calc} / \partial \mu_{axf}$ is calculated using the system of equations represented by Eq. (5.4) and (5.5), which constitute the forward problem. Taking the derivatives of both sides of Eq. (5.4) and (5.5) with respect to μ_{axf} yields

$$\frac{\partial \underline{\mathbf{K}}_x}{\partial \mu_{axf}} \underline{\Phi}_x + \underline{\mathbf{K}}_x \frac{\partial \underline{\Phi}_x}{\partial \mu_{axf}} = \mathbf{0}, \quad (5.9)$$

$$\frac{\partial \underline{\mathbf{K}}_m}{\partial \mu_{axf}} \underline{\Phi}_m + \underline{\mathbf{K}}_m \frac{\partial \underline{\Phi}_m}{\partial \mu_{axf}} = \frac{\partial \underline{\mathbf{B}}_{x \rightarrow m}}{\partial \mu_{axf}} \underline{\Phi}_x + \underline{\mathbf{B}}_{x \rightarrow m} \frac{\partial \underline{\Phi}_x}{\partial \mu_{axf}}. \quad (5.10)$$

The above Eq. (5.9) and (5.10) are combined to give

$$\frac{\partial \underline{\Phi}_m}{\partial \mu_{axf}} = \underline{\mathbf{K}}_m^{-1} \frac{\partial \underline{\mathbf{B}}_{x \rightarrow m}}{\partial \mu_{axf}} \underline{\Phi}_x - \underline{\mathbf{K}}_m^{-1} \underline{\mathbf{B}}_{x \rightarrow m} \underline{\mathbf{K}}_x^{-1} \frac{\partial \underline{\mathbf{K}}_x}{\partial \mu_{axf}} \underline{\Phi}_x - \underline{\mathbf{K}}_m^{-1} \frac{\partial \underline{\mathbf{K}}_m}{\partial \mu_{axf}} \underline{\Phi}_m. \quad (5.11)$$

Equations (5.4), (5.5) and (5.11) show that $\partial \underline{\Phi}_m / \partial \mu_{axf}$ in Eq. (5.11) is an $N \times N$ matrix, whereas $\partial \underline{\Phi}_m^{calc} / \partial \mu_{axf}$ required for the calculation of the Jacobian is an $M \times N$ describing the sensitivity of only the *boundary* measurements with respect to the nodal values of μ_{axf} . Accordingly, $\partial \underline{\Phi}_m^{calc} / \partial \mu_{axf}$ in Eq. (5.8) is obtained by taking inner product between a Dirac matrix and $\partial \underline{\Phi}_m / \partial \mu_{axf}$. The Dirac matrix, D , is an $N \times M$ matrix in which each column is unity at nodes corresponding to the boundary detector location and zero elsewhere. Thus

$$\begin{aligned} \frac{\partial \underline{\Phi}_m^{calc}}{\partial \mu_{axf}} &= \left\langle D, \frac{\partial \underline{\Phi}_m}{\partial \mu_{axf}} \right\rangle \\ &= \left\langle D, \underline{\mathbf{K}}_m^{-1} \frac{\partial \underline{\mathbf{B}}_{x \rightarrow m}}{\partial \mu_{axf}} \underline{\Phi}_x - \underline{\mathbf{K}}_m^{-1} \underline{\mathbf{B}}_{x \rightarrow m} \underline{\mathbf{K}}_x^{-1} \frac{\partial \underline{\mathbf{K}}_x}{\partial \mu_{axf}} \underline{\Phi}_x - \underline{\mathbf{K}}_m^{-1} \frac{\partial \underline{\mathbf{K}}_m}{\partial \mu_{axf}} \underline{\Phi}_m \right\rangle \end{aligned} \quad (5.12)$$

where $\langle \cdot, \cdot \rangle$ denotes the standard inner product of vectors. To reduce the computational cost, the adjoint theorem (see Appendix A3) is applied in Eq. (5.12). Hence

$$\frac{\partial \underline{\Phi}_m^{calc}}{\partial \mu_{axf}} = \left\langle (\underline{\mathbf{K}}_m^{-1})^* D, \frac{\partial \underline{\mathbf{B}}_{x \rightarrow m}}{\partial \mu_{axf}} \underline{\Phi}_x \right\rangle - \left\langle (\underline{\mathbf{K}}_m^{-1} \underline{\mathbf{B}}_{x \rightarrow m} \underline{\mathbf{K}}_x^{-1})^* D, \frac{\partial \underline{\mathbf{K}}_x}{\partial \mu_{axf}} \underline{\Phi}_x \right\rangle$$

$$-\left\langle (\mathbf{K}_m^{-1})^* D, \frac{\partial \mathbf{K}_m}{\partial \mu_{axf}} \Phi_m \right\rangle, \quad (5.13)$$

which when used in Eq. (5.8) yields the Jacobian sensitivity matrix, $\mathbf{J}_{E_{\Phi_m}}$.

In Eq. (5.7), the matrix $\mathbf{J}_{E_{\Phi_m}}^* \mathbf{J}_{E_{\Phi_m}}$ is not explicitly inverted, rather the system of linear equations

$$\mathbf{J}_{E_{\Phi_m}}^* \mathbf{J}_{E_{\Phi_m}} d_k = -\mathbf{J}_{E_{\Phi_m}}, \quad (5.14)$$

is solved for d_k and the next iterate is taken as

$$(\mu_{axf})_{k+1} = (\mu_{axf})_k + d_k. \quad (5.15)$$

In this study, we have used MATLAB[®] function `lsqr()` to solve the system of equations represented by Eq. (5.14). The details of the algorithms used in function `lsqr()` can be found in the published work by Paige *et al.*¹¹² In addition, a novel vectorization scheme given by Fedele *et al.*¹¹³ was implemented for finite element global matrix assembly and Jacobian sensitivity calculations in order to avoid computationally intensive loop implementation.

In this study we have used a GN based imaging algorithm as a replacement to the PMBF/CONTN imaging algorithm described in Section 3. Although PMBF/CONTN is a detailed and more efficient imaging algorithm since it can take into account any *a priori* information at hand as well as the physical considerations of the tomographic problem, our current approach is to focus on such means which enable us to make fast decisions about target's presence so that a large number of cases can be investigated. For this reason, we have used the GN based scheme with single iteration for all cases.

The main concern of our investigation is to find a specific answer to whether or not a target is present. Consequently, we have investigated the location of the target as well as a rough estimate of its size without any worries about the fluorophore concentration at the target's site because the GN based algorithm is not capable of answering such questions and, at the same time, it's not something we intended to do herein. To be specific, this study employs the imaging algorithm as a quick means to perform target detection task, (a yes/no decision,) so that a large number of cases can be investigated in a reasonable amount of time. For example, a typical imaging reconstruction problem that requires more than couple of hours when solved using a full PMBF/CONTN routine, but requires only 10 minutes for performing a single iteration of GN based scheme. As described in the following section, the psychophysical analysis of an imaging modality requires observer investigations of numerous reconstructed images to draw conclusions about the diagnostic accuracy of the modality. Using GN based algorithm enables us to perform such analyses in a feasible amount of time.

5.2.2 Psychophysical analysis

Psychophysics describes and investigates individual percepts so that they can be communicated and shared by others.¹¹⁴ In detection tasks, the individual perception usually is the answer to a simple question: "Is there a target present?" The psychophysical approach that involves this kind of decision making falls under the category of signal detection theory (SDT) and has been well researched.⁴⁴ In these binary detection tasks, an observer usually classifies the imaging data at hand into one of

the following two groups: signal-present (H_1) or signal-absent (H_0), implying that hypothesis H_1 or H_0 is true, respectively. Two types of restrictions are imposed on the manner by which observer makes decisions. First, no randomness is allowed in the decision rule, meaning that the repeated observations of the same imaging data must result in the same decision. Second, every observation must result in an unequivocal decision.

The description provided previously in Section 2.4.2 follows that an observer's decision is based on the imaging data \mathbf{g} obtained through the imaging system. The imaging data \mathbf{g} is usually contaminated by noise, as is evident from the imaging equation, $\mathbf{g} = \mathbf{H}(\mathbf{f}) + \mathbf{n}$, where \mathbf{H} is an operator describing how the imaging system maps the object \mathbf{f} being imaged to the discrete measurements \mathbf{g} ; and \mathbf{n} is the noise in the measurement system. In fluorescence imaging, since \mathbf{g} is measured only at the boundaries and is used afterwards to make predictions about the interior tissue, an observer making decisions based totally on \mathbf{g} can not always be correct. In addition, the noise in the imaging data enhances the difficulty of the observer making decisions. As a result, the following four scenarios exist for any observation:

1. True positive (TP): H_1 is true; observer decides H_1 is true.
2. False positive (FP): H_0 is true; observer decides H_1 is true.
3. False negative (FN): H_1 is true; observer decides H_0 is true.
4. True negative (TN): H_0 is true; observer decides H_0 is true.

Furthermore, if N is the total number of decisions made by an observer; and N_{TP} denotes the number of true positive decisions made by the observer, etc; then

$$N = N_{TP} + N_{TN} + N_{FP} + N_{FN}. \quad (5.16)$$

In the limit of an infinite number of observations, the actual true- and false-positive fractions can be obtained:

$$TPF = \lim_{N \rightarrow \infty} \left[\frac{\text{Number of true positive decisions}}{\text{Number of actual positive cases}} \right] = \left\langle \frac{N_{TP}}{N_{TP} + N_{FN}} \right\rangle \quad (5.17)$$

$$TNF = \lim_{N \rightarrow \infty} \left[\frac{\text{Number of true negative decisions}}{\text{Number of actual negative cases}} \right] = \left\langle \frac{N_{TN}}{N_{TN} + N_{FP}} \right\rangle \quad (5.18)$$

$$FPF = \left\langle \frac{N_{FP}}{N_{TN} + N_{FP}} \right\rangle = 1 - TNF \quad (5.19)$$

$$FNF = \left\langle \frac{N_{FN}}{N_{TP} + N_{FN}} \right\rangle = 1 - TPF \quad (5.20)$$

By definition each of the above fractions lies in the range from zero to one. It is obvious that the observer performance can be completely specified by two of the fractions, e.g. TPF and FPF . In medical terminology, the TPF is referred to as the *sensitivity* since it tells how sensitive the decision criterion is to the presence of a target. Similarly, the FPF is referred to as *specificity* since a criterion with low specificity yields many false or meaningless positive decisions.

5.2.2.1 The ROC curve

Receiver operating characteristic (ROC) curve for an observer is obtained by plotting the sensitivity (TPF) against the specificity (FPF). Different points along an ROC curve represent different levels of bias in the decision making. Both sensitivity and specificity depend upon the decision threshold (bias) used by individual observer, and thus vary

with each observer's criterion of what to call positive and what to call negative. As a result, ROC analysis facilitates a systematic tool for quantifying the impact of variability among individuals' biases. It can also incorporate the effect of varying conditions on the performance of diagnostic modality. For example in mammography, the sources of variability can include (i) different radiologist's decision thresholds, (ii) different amounts of time between interpreting mammograms, or (iii) variation within cases due to the inherent imprecision of breast compression.¹¹⁵ In short, the ROC analysis averages the effect of different conditions on the accuracy of the diagnostic modality. Therefore, the area under the ROC curve (*AUC*) is viewed as the diagnostic accuracy of the imaging modality.⁴⁴ Since both the *FPF* and the *TPF* range from 0 to 1, the area under the ROC curve also ranges from 0 to 1. In general, a classification system with higher *AUC* value is preferred over the ones with lower values.⁴⁴

5.2.3 Simulated imaging data

It is obvious from the discussions in previous sections that the assessment of an imaging modality via psychophysical tools of OAIQ requires (i) a task, (ii) an observer, and (iii) patient data so that the observer can perform the detection task. Due to the lack of sufficient clinical trials for fluorescence-enhanced diagnostic of breast malignancies, we have resorted to simulation study as an appropriate alternative. Thus, in lieu of the actual patient data, we have used synthetic patient data obtained through modeling the randomness associated with anatomical structure of mammarian tissues in this study. Specifically, we have used a breast-shaped geometry (see Fig. 4.1) to model the shape of

a typical human breast. In order to model (i) random spatial variations in the absorption and scattering optical properties characteristic of natural anatomical tissue structure, and (ii) non-uniform distribution of the disease markers, we have used the lumpy-object model.¹² The description of lumpy-object model is given in previous sections (refer to Section 2.3.1, 3.2.2 and 4.2.2).

Clinical conditions for breast cancer imaging involve patients who might or might not have a malignancy. In addition, there is no knowledge of the tissue structure of an individual patient. It is well known that the anatomical tissue structure of one patient is randomly different from another, which, coupled with the uncertainty associated with the location of malignancy (if there is one), implies that the simulation studies must incorporate these variations associated with true imaging scenario. In consequence, we have attempted to simulate a “double-blinded” type of situation in which the human observer performing the detection task had no prior knowledge of target’s presence as well as the simulated background* tissue structure. Also, the image reconstruction algorithm had no information regarding the background tissue structure.

In summary, the following describes the steps involved to simulate clinical trials for breast imaging:

1. A breast-shaped geometry (see Fig. 4.1) of volume ~ 300 cc was used to simulate a human breast.
2. The lumpy-object model was employed to simulate background tissue structure.

Lumps in endogenous optical properties were used to simulate the natural anatomical

* In the context of SDT, the term “background” refers to the space consisting of the whole domain except the target.

structure of the tissue, whereas lumps in exogenous optical properties were used to simulate the non-uniform distribution of the disease markers in the background.

3. A dice was thrown to decide whether or not to place a fluorescent target. In case the target must be placed, a random location inside the breast geometry was chosen as the center of the target (a spherical volume of 1 cc).
4. The imaging data were generated by adding the diffusion model's solutions at the boundary detector locations to the noise typical of a clinical imaging setup (as described in Section 4.2.3.2).
5. The noisy imaging data was input to the GN based imaging algorithm. The imaging algorithm had no prior information about the spatial variations of endogenous optical properties which characterize the anatomical structure of biological tissues.
6. The reconstructed images of all the cases were given to a human observer (Amit Sahu, Baylor College of Medicine, Houston, TX) in order for him to perform the detection task. A yes/no decision on target's presence were obtained from observer for all the cases. The observer had no prior information about target's presence, target's location, and the background variations in endogenous and exogenous optical properties.
7. The human observer's decisions were compared with truth in order to estimate the true-positive and true-negative fractions.

As described in previous sections, twenty five source points and 128 detector points (see Fig. 4.2) were used for collecting the boundary measurements of emission photon density wave amplitude (I_{AC_m}) and phase delay (θ_m). Following the treatment

given in Section 4.2.3.2, we added 5% Gaussian noise to I_{AC_m} and uniform random noise in range $(-2^\circ, +2^\circ)$ to θ_m . The tomographic image reconstruction computations were performed on a LINUX workstation with AMD Opteron 285 (2.6 GHz) and 8.0 GB RAM. The general mesh viewer, GMV (LANL, Las Alamos, NM), software was used for 3D visualization of the spatial distribution of reconstructed fluorophore activity (μ_{axf}). The true-positive fractions were calculated for the human observer performing the target detection task in order to assess the effect of (i) endogenous lumpy backgrounds, and (ii) exogenous lumpy backgrounds on the reconstructed images.

5.3 Results and discussion

The lumpy backgrounds were generated using the approach described in Section 4. The generation of synthetic patient data required ~ 1 min for each case. A single iteration of the GN based algorithm to produce reconstructed images required ~ 8 min of CPU time. The human observer performing the detection task spent on an average ~ 1 -2 min to arrive at a final decision for each case.

5.3.1 Sensitivity of the classifier performance to background variations

At first, the sensitivity of the classifier performance to the variations in the tissue type was examined. To accomplish this, we studied how detectability of 1 cc fluorescent targets (TBR=50) superimposed in the lumpy backgrounds of endogenous optical properties was affected by the variations in lump strength. As mentioned earlier, the target locations were chosen randomly inside the hemispherical portion of the breast-

shaped geometry. However, the targets were restricted to depths 2 *cm* or less from the surface of the hemisphere. Table 5.1 reports the decisions made by a human observer on the presence of a target based on the visualization of reconstructed images. The table lists the human observer's decisions for varying endogenous lump strengths in the background as well as the truth for each case. The *TPF* values were calculated as a function of varying lump strengths and are plotted in Fig. 5.1.

Next, we performed a similar study to examine the effects of both the tissue type as well as the non-uniform distribution of the disease markers on the performance of a human observer. However, in this case the targets were allowed to be placed deeper (2.5 *cm* or less) as compared to the above study. In addition, the number of lumps (N_p) was set to 50, as opposed to the value 100 in the above study, so that a comparable number of true-positives can be detected. Our rationale behind this is that the higher level heterogeneous backgrounds in exogenous optical properties make it difficult to detect an underlying target. Thus we reduced the number of lumps in the background to obtain higher true-positives in this case as well. Since the study was performed to compare the results of different lump strengths rather than making an absolute statement, the choice of a lower N_p (or a lower sample space, for that matter) did not introduce any bias. The human observer's decisions based on the reconstructed images generated herein are reported in Table 5.2 and a plot similar to Fig. 5.1 is shown in Fig. 5.2.

Table 5.1 Results of the Qualitative Analysis (Visual Inspection): A human observer's decisions on the presence of a randomly located 1 cc spherical fluorescent target (at depths 2 cm or less from the hemispherical surface of the breast-shaped geometry) having 50 times more contrast than the background. The background endogenous optical properties are heterogeneous in nature represented by the lumpy-object model (Number of lumps, $N_p=100$; lump width, $w=0.5$ cm).

lump strength	5 %		10 %		25 %		50 %		100 %	
case	human	truth	human	truth	human	truth	human	truth	human	truth
1	no	no	no	no	yes	yes	no	no	no	no
2	no	no	yes	yes	no	no	yes	yes	no	no
3	yes	yes	yes	yes	no	no	yes	yes	<u>no</u>	yes
4	yes	yes	no	no	yes	yes	yes	yes	no	no
5	yes	yes	no	no	yes	yes	yes	yes	no	no
6	yes	yes	yes	yes	no	no	no	no	<u>yes</u>	no
7	no	no	yes	yes	no	no	no	no	yes	yes
8	no	no	no	no	no	no	no	no	no	no
9	yes	yes	no	no	no	no	yes	yes	no	no
10	yes	yes	yes	yes	no	no	no	no	no	no
11	no	no	yes	yes	yes	yes	no	no	no	no
12	yes	yes	yes	yes	no	no	no	no	<u>yes</u>	no
13	yes	yes	yes	yes	yes	yes	yes	yes	no	no
14	no	no	no	no	no	no	yes	yes	yes	yes
15	no	no	no	no	yes	yes	no	no	no	no
16	no	no	yes	yes	yes	yes	yes	yes	no	no
17	yes	yes	yes	yes	no	no	yes	yes	yes	yes
18	no	no	no	no	yes	yes	no	no	<u>no</u>	yes
19	yes	yes	no	no	yes	yes	no	no	no	no
20	yes	yes	no	no	no	no	no	no	yes	yes
21	yes	yes	no	no	no	no	no	no	yes	yes
22	no	no	yes	yes	yes	yes	yes	yes	yes	yes
23	no	no	no	no	no	no	yes	yes	yes	yes
24	yes	yes	yes	yes	yes	yes	no	no	yes	yes
25	yes	yes	yes	yes	no	no	yes	yes	<u>no</u>	yes
26	no	no	yes	yes	no	no	yes	yes	<u>yes</u>	no
27	no	no	yes	yes	yes	yes	no	no	no	no
28	no	no	no	no	yes	yes	<u>no</u>	yes	yes	yes
29	no	no	no	no	no	no	no	no	no	no
30	yes	yes	no	no	no	no	no	no	yes	yes
31	yes	yes	yes	yes	yes	yes	<u>no</u>	yes	yes	yes
32	no	no	yes	yes	yes	yes	yes	yes	<u>no</u>	yes
33	yes	yes	no	no	no	no	yes	yes	no	no
34	yes	yes	yes	yes	yes	yes	no	no	yes	yes
35	no	no	yes	yes	yes	yes	no	no	no	no
36	yes	yes	no	no	no	no	no	no	no	no
37	yes	yes	no	no	no	no	no	no	<u>no</u>	yes
38	no	no	yes	yes	yes	yes	no	no	no	no
39	yes	yes	no	no	yes	yes	no	no	no	no
40	no	no	no	no	no	no	no	no	no	no
	TPF=21/21		TPF=20/20		TPF=20/20		TPF=15/17		TPF=12/17	

Table 5.2 Results of the Qualitative Analysis (Visual Inspection): A human observer's decisions on the presence of a randomly located 1 cc spherical fluorescent target (at depths 2.5 cm or less from the hemispherical surface of the breast-shaped geometry) having 50 times more contrast than the average background. The background endogenous as well as exogenous optical properties are heterogeneous in nature represented by the lumpy-object model (Number of lumps, $N_p=50$; lump width, $w=0.5$ cm).

lump strength	5 %		10 %		25 %		50 %		100 %	
case	human	truth	human	truth	human	truth	human	truth	human	truth
1	yes	yes	yes	yes	no	no	yes	yes	yes	yes
2	yes	yes	yes	yes	yes	yes	no	no	yes	yes
3	yes	yes	no	no	yes	yes	yes	yes	no	no
4	no	no	yes	yes	no	no	yes	yes	<u>no</u>	yes
5	no	no	no	no	no	no	<u>no</u>	yes	no	no
6	yes	yes	no	no	yes	yes	yes	yes	<u>no</u>	yes
7	yes	yes	yes	yes	no	no	no	no	no	no
8	yes	yes	no	no	yes	yes	no	no	no	no
9	no	no	yes	yes	no	no	<u>no</u>	yes	no	no
10	yes	yes	yes	yes	yes	yes	no	no	yes	yes
11	no	no	<u>no</u>	yes	no	no	<u>no</u>	yes	yes	yes
12	no	no	no	no	yes	yes	no	no	yes	yes
13	no	no	yes	yes	no	no	no	no	yes	yes
14	no	no	no	no	yes	yes	yes	yes	<u>no</u>	yes
15	yes	yes	yes	yes	no	no	no	no	<u>no</u>	yes
16	no	no	yes	yes	yes	yes	no	no	no	no
17	no	no	no	no	yes	yes	yes	yes	<u>no</u>	yes
18	yes	yes	yes	yes	no	no	no	no	<u>no</u>	yes
19	yes	yes	no	no	yes	yes	no	no	<u>no</u>	yes
20	yes	yes	yes	yes	no	no	no	no	no	no
21	yes	yes	yes	yes	yes	yes	no	no	<u>no</u>	yes
22	no	no	no	no	no	no	yes	yes	yes	yes
23	no	no	no	no	yes	yes	yes	yes	no	no
24	no	no	yes	yes	no	no	no	no	no	no
25	no	no	yes	yes	yes	yes	yes	yes	yes	yes
26	no	no	no	no	yes	yes	no	no	<u>yes</u>	no
27	yes	yes	no	no	no	no	no	no	<u>no</u>	yes
28	no	no	yes	yes	yes	yes	yes	yes	<u>no</u>	yes
29	yes	yes	yes	yes	no	no	yes	yes	yes	yes
30	yes	yes	yes	yes	yes	yes	<u>yes</u>	no	yes	yes
	TPF=15/15		TPF=16/17		TPF=15/15		TPF=11/14		TPF=10/20	

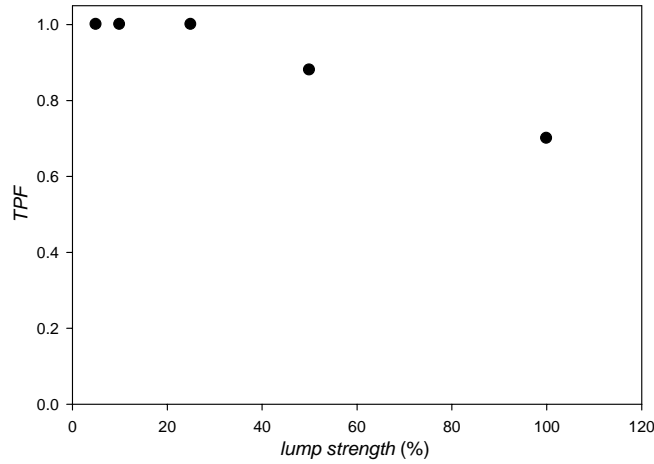


Fig. 5.1 The true-positive fraction (TPF) of human observer's diagnostic test (based on the visualization of reconstructed images) in a "double-blinded" type setup vs. the strength of endogenous lumps (Number of lumps, $N_p=100$; lump width, $w=0.5$ cm). The fluorescent target is a 1 cc spherical volume randomly located at depths of 2 cm or less, and is contrasted from its surroundings by 50:1. A total of 40 simulated patients, as shown in Table 5.1, were considered for each lump strength value.

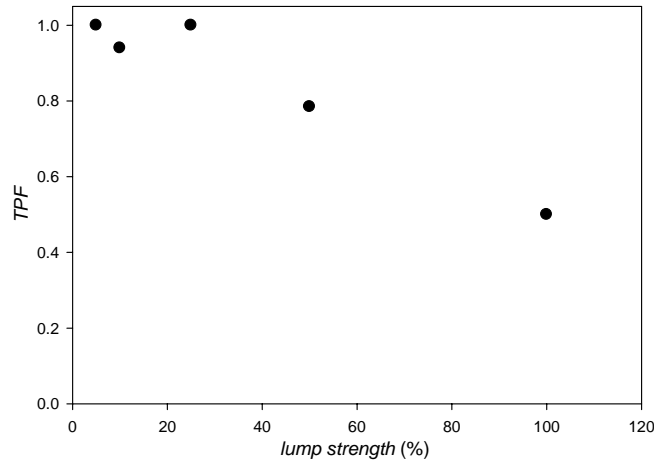


Fig. 5.2 The true-positive fraction (TPF) of human observer's diagnostic test (based on the visualization of reconstructed images) in a "double-blinded" type setup vs. the strength of endogenous as well as exogenous lumps (Number of lumps, $N_p=50$; lump width, $w=0.5$ cm). The fluorescent target is a 1 cc spherical volume randomly located at depths of 2.5 cm or less, and is contrasted from its surroundings by 50:1. A total of 30 simulated patients, as shown in Table 5.2, were considered for each lump strength value.

Both figures (Figs. 5.1 and 5.2) show that the TPF value decreases as the lump strength increases. In other words, when the background becomes more heterogeneous in the optical properties, the “sensitivity” of the human observer to the presence of a target decreases, resulting in his/her inability to positively detect targets in some of the cases. This is consistent with our study in Section 4 involving the Hotelling observer, wherein we showed that the perturbations in background endogenous and/or exogenous optical properties adversely affected the SKE detection task (see Section 4.3.1). In fact, the Hotelling observer studies performed only a statistical manipulation on imaging data \mathbf{g} , and, unlike the present study, computationally intensive reconstructions were not performed to evaluate the imaging system. Yet, the Hotelling observer analysis was successful in making similar predictions, albeit in SKE cases which is in contrast with the present study. This is a positive outcome with regards to establishing the feasibility of OAIQ tools for fluorescence-enhanced optical imaging systems. Nonetheless, we advocate experimental validation to provide further insight into the effects of heterogeneous backgrounds. We present this *simulation-only* study as an aid to understanding the feasibility of OAIQ tools rather than applied as a blanket statement.

Finally, our lack of success in finding an appropriate decision variable has restricted us from employing an ROC curve analysis in the present simulation study. In actual conditions, a relevant study can be done with respect to the type of disease marker that has been used to tag a malignant site. Therein, the level of expression of the marker in the malignancy with respect to the background seems to be an apt choice for decision variable. For example, a group of patients can be imaged with different disease markers

and the true-positives/true-negatives for each disease marker can be plotted as different points along an ROC curve. To explain why this particular analysis is difficult in simulation studies, we first mention that different patients have been characterized by randomly generated backgrounds of endogenous and exogenous optical properties in our methodology of simulating patient data. Therefore, if a certain patient with no malignancy is imaged with different disease markers, the reconstructed images will be exactly the same for each case, without regards to the type of marker used. This is due to our method of characterizing a patient by a fixed* background level of expression of the disease marker (represented by the exogenous optical properties), which, in turn, makes a simulated patient's characteristics independent of the level of expression of the marker in malignant site. This limits our ability to perform an ROC curve analysis based on the above mentioned decision variable. Our future studies will address different methods to simulate patient data so that the above mentioned ROC curve analysis can be performed. Additionally, we will make an effort in the direction of finding decision variables suitable with the present simulation methodology.

5.4 Conclusions

We have presented an approach to perform psychophysical analysis for a fluorescence-enhanced optical imaging system. Specifically, we have employed a simulation methodology to obtain synthetic patient data similar to clinical breast imaging. A lumpy-object model is used to simulate patient variability and the noise associated with

* Although the backgrounds are generated with a randomized lumpy-object model, they remain fixed once assigned to a certain patient.

the imaging system has been considered in the imaging data. A GN based tomographic algorithm has been used to obtain reconstructed images for multiple cases of randomly located targets in random heterogeneous backgrounds. A human observer's performance in detecting a target through visualization of reconstructed images has been evaluated. Specifically, the sensitivity of the human observer's performance to the variations in the tissue type and the background expression of the disease markers have been investigated. The study demonstrates that the detection capability of the human observer decreases as the strength of the background variations increases. Furthermore, the study helps interpret the results of Hotelling observer analysis presented previously in Section 4.3.1.

6. CONCLUSIONS AND SUGGESTED FUTURE WORK

In this dissertation, we have presented a rationale for using the OAIQ tools to assess a fluorescence-enhanced optical imaging system. Our studies mark the first instance of implementing these tools in fluorescence imaging systems. Of particular interest was to analyze how a highly non-linear fluorescence imaging system can be assessed by such tools that have been previously validated for mostly linear imaging systems.

Due to the unavailability of sufficient clinical trials and due to the fact that fluorescence-enhanced optical imaging is a new and upcoming technology, the imaging data involving real patients are not widely reported or easily accessible. For this reason, we have resorted to the methods of simulation as a rational alternative to obtaining imaging data sets typical of clinical breast imaging. In simulations, we have used a lumpy-object model with the assumption that it can reasonably mimic the patient variability associated with the mammarian tissue structure as well as the background expression of the disease markers. With the ability to generate imaging data, we have addressed the issue of image quality assessment for fluorescence imaging systems in the following manner:

- 1) As a first step toward establishing the feasibility of OAIQ tools, we assess a tomographic image reconstruction algorithm's performance in the task of detecting a fluorescently labeled target embedded in the lumpy backgrounds of the optical properties. Specifically, we assessed the performance of a novel PMBF/CONTN imaging algorithm developed by Roy *et al.*⁵⁷ Based on single

cases of tomographically reconstructed images, we showed that the image reconstruction was (i) unaffected by normal anatomical heterogeneity manifested in endogenous tissue optical properties of absorption and scattering, and (ii) restricted by heterogeneous distribution of fluorophore in the background as the contrast was decreased.

- 2) Next, we made an attempt to evaluate the fluorescence imaging system independently from the image reconstruction algorithm. Accordingly, we used a Hotelling observer to directly assess the detection capability of the imaging system based on the imaging measurements. The Hotelling observer's analysis helped in comparing the performance of our imaging system at varying background strengths, target depths, and light-rejection filter properties. Our results showed that the SNR of Hotelling observer (i) decreased as the strength of lumpy perturbations in the background was increased, (ii) decreased as the target depth was increased, and (iii) increased as the excitation light leakage was decreased, and reached a maximum for filter OD values of 5 or higher at λ_x .
- 3) Finally, we presented a method to perform psychophysical analysis of the human observer performing the target detection task. We developed a GN based tomographic algorithm for this study so that multiple cases of reconstructed images can be obtained in feasible amount of computation time. Our results showed that the detection capability of the human observer was sensitive to both the endogenous as well as the exogenous lumps in the background. The results

were consistent with the Hotelling observer's predictions in similar type of studies.

The results contained in the dissertation provide a preliminary assessment of the fluorescence-enhanced optical imaging system with regards to the feasibility of the OAIQ tools to assess the imaging performance as well as to aid in the translation of fluorescence imaging to the clinics.

6.1 Future directions

The following is a list of suggested research work for future development of OAIQ tools and fluorescence imaging, in general, guided along the central theme of making fluorescence imaging suitable for clinics.

- 1) Bochud *et al.*⁴⁶ have shown that the clustered lumpy-object model represents the natural anatomical tissue structures more realistically than the lumpy-object model. Studies similar to this dissertation can be done by using clustered lumpy objects to model patient variability. Since clustered lumps are, indeed, many clusters of the lumpy-objects, it can be expected that the performance of the image reconstruction algorithm will be even more sensitive to clustered lumps.
- 2) Using a statistical model of the measurement system will help in accounting for any statistical information about the measurements noise. This will further aid in developing approached for localization of targets by use of maximum-

likelihood estimation. Furthermore, the probability of target detection and Cramer-Rao bounds⁴⁴ can be used for the optimization of the imaging system.

- 3) In Section 4, it was reported that the Hotelling observer's SNR was biased with respect to the sample size. A study can be performed to find the nature of bias so that the true value of the Hotelling observer's SNR can be calculated using a computationally feasible sample size.
- 4) Research can be performed in the direction of finding suitable decision variables for ROC curves so that simulation studies can be analyzed psychophysically. Accordingly, new methods to simulate patient data need to be devised.
- 5) Other tomographic image reconstruction algorithms, such as PMBF/CONTN, can be tested in studies similar to the analyses given in Sections 3 and 5.
- 6) DeGrand *et al.*¹¹⁶ have recently demonstrated a method to construct tissue-like phantoms NIR fluorescence imaging applications. A similar approach can be applied to manufacture breast phantoms suitable for the research work described in this dissertation.
- 7) Studies can be performed to analyze the nature of covariance matrix, \mathbf{K}_g , in different experimental conditions. For example, the existence of significant off-diagonal elements in the covariance matrix implies that some of the detectors are correlated and, thus, can affect the signal detectability.

REFERENCES

1. E. K. Fry, G. Kossoff, and H. A. Hindman, "Potential of ultrasound visualization for detecting the presence of abnormal structures within the female breast," *IEEE Transactions on Sonics and Ultrasonics* **20**, 49-49 (1973).
2. Z. D. Grossman, M. D. P. Brian, J. G. McAfee, B. Wistow, and D. Bassano, "Comparison of nuclear imaging, gray scale ultrasonography and computed axial tomography of liver," *Journal of Nuclear Medicine* **17**, 544-545 (1976).
3. R. K. Zeman, and A. Gottschalk, "Current aspects of nuclear imaging in clinical oncology," *Cancer* **47**, 1154-1158 (1981).
4. W. Steinbrich, D. Beyer, and U. Modder, "Malignant lymph-node disease-diagnosis with MRI in comparison with other imaging modalities," *Der Radiologe* **25**, 199-205 (1985).
5. P. M. Smithjones, B. Stolz, C. Bruns, R. Albert, H. W. Reist, R. Fridrich, and H. R. Macke, "Gallium-67/Gallium-68-[DFO]-Octreotide- A Potential radiopharmaceutical for PET imaging of somatostatin receptor-positive tumors-synthesis and rediolabeling *in vitro* and preliminary *in vivo* studies," *Journal of Nuclear Medicine* **35**, 317-325 (1994).
6. D. L. Bailey, B. F. Hutton, and P. J. Walker, "Improved SPECT using simultaneous emission and transmission tomography," *Journal of Nuclear Medicine* **28**, 844-851 (1987).

7. J. P. Houston, S. Ke, W. Wang, C. Li, and E. M. Sevick-Muraca, "Quality analysis of *in vivo* NIR fluorescence and conventional gamma images acquired using a dual-labeled tumor-targeting probe," *Journal of Biomedical Optics* **10**, 054010 (2005).
8. A. B. Milstein, S. Oh, K. J. Webb, C. A. Bouman, Q. Zhang, D. A. Boas, and R. P. Millane, "Fluorescence optical diffusion tomography," *Applied Optics* **42**, 3081-3094 (2003).
9. A. Godavarty, A. B. Thompson, R. Roy, M. Gurfinkel, M. J. Eppstein, C. Zhang, and E. M. Sevick-Muraca, "Diagnostic Imaging of breast cancer using fluorescence-enhanced optical tomography," *Journal of Biomedical Optics* **9**, 488-496 (2004).
10. A. Godavarty, M. J. Eppstein, C. Zhang, and E. M. Sevick-Muraca, "Detection of multiple targets in breast phantoms using fluorescence enhanced optical imaging," *Radiology* **235**, 148-154 (2005).
11. R. Roy, and E. M. Sevick-Muraca, "Three-dimensional unconstrained and constrained image reconstruction techniques applied to fluorescence frequency-domain photon migration," *Applied Optics* **40**, 2206-2215 (2001).
12. J. P. Rolland, and H. H. Barrett, "Effect of random background inhomogeneity on observer detection performance," *Journal of Optical Society of America A* **9**, 649-658 (1992).

13. C. K. Abbey, and H. H. Barrett, "Human- and model- observer performance in ramp-spectrum noise: effects of regularization and object variability," *Journal of Optical Society of America A* **18**, 473-488 (2001).
14. H. H. Barrett, "Objective assessment of image quality: effects of quantum noise and object variability," *Journal of Optical Society of America A* **7**, 1266-1278 (1990).
15. H. H. Barrett, J. L. Denny, R. F. Wagner, and K. J. Myers, "Objective assessment of image quality. II. Fisher information, Fourier crosstalk, and figures of merit for task performance," *Journal of Optical Society of America A* **12**, 834-852 (1995).
16. H. H. Barrett, C. K. Abbey, and E. Clarkson, "Objective assessment of image quality. III. ROC metrics, ideal observers, and likelihood-generating functions," *Journal of Optical Society of America A* **15**, 1520-1535 (1998).
17. B. W. Pogue, C. Willscher, T. O. McBride, U. L. Osterberg, and K. D. Paulsen, "Contrast-detail analysis for detection and characterization with near-infrared diffuse tomography," *Medical Physics* **27**, 2693-2700 (2000).
18. F. Gao, H. Zhao, Y. Tanikawa, K. Homma, and Y. Yamada, "Influences of target size and contrast on near infrared diffuse optical tomography - a comparison between featured-data and full time-resolved schemes," *Optical and Quantum Electronics* **37**, 1287-1304 (2005).
19. X. Song, B. W. Pogue, T. D. Tosteson, T. O. McBride, S. Jiang, and K. D. Paulsen, "Statistical analysis of non-linearly reconstructed near-infrared

- tomographic images: part II – experimental interpretation," IEEE Transactions on Medical Imaging **21**, 764-772 (2002).
20. B. W. Pogue, X. Song, T. D. Tosteson, T. O. McBride, S. Jiang, and K. D. Paulsen, "Statistical analysis of non-linearly reconstructed near-infrared tomographic images: part I - theory and simulations," IEEE Transactions on Medical Imaging **21**, 755-763 (2002).
 21. A. R. Pineda, H. H. Barrett, and S. R. Arridge, "Spatially varying detectability for the optical tomography," in *Medical Imaging 2000: Physics of Medical Imaging*, (SPIE, 2000), pp. 77-83.
 22. H. Dehghani, B. W. Pogue, J. Shudong, B. Brooksby, and K. D. Paulsen, "Three-dimensional optical tomography: resolution in small-object imaging," Applied Optics **42**, 3117-3128 (2003).
 23. A. B. Milstein, M. D. Kennedy, P. S. Low, C. A. Bouman, and K. J. Webb, "Statistical approach for detection and localization of a fluorescing mouse tumor in Intralipid," Applied Optics **44**, 2300-2310 (2005).
 24. J. Duderstadt, and L. J. Hamilton, *Nuclear Reactor Analysis* (Wiley New York, 1976).
 25. W. Cai, M. Xu, and R. R. Alfano, "Three-dimensional radiative transfer tomography for turbid media," IEEE Journal of Selected Topics in Quantum Electronics **9**, 189-198 (2003).
 26. A. D. Klose, U. Netz, J. Beuthan, and A. H. Hielscher, "Optical tomography using the time-independent equation of radiative transfer - Part 1: forward

- model," *Journal of Quantitative Spectroscopy & Radiative Transfer* **72**, 691–713 (2002).
27. T. Tarvainen, M. Vauhkonen, V. Kolehmainen, S. R. Arridge, and J. P. Kaipio, "Coupled radiative transfer equation and diffusion approximation model for photon migration in turbid medium with low-scattering and non-scattering regions," *Physics in Medicine and Biology* **50** 4913–4930 (2005).
 28. T. Tarvainen, M. Vauhkonen, V. Kolehmainen, and J. P. Kaipio, "Finite element model for the coupled radiative transfer equation and diffusion approximation," *International Journal for Numerical Methods in Engineering* **65**, 383–405 (2006).
 29. S. Srinivasan, B. W. Pogue, H. Dehghani, S. Jiang, X. Song, and K. D. Paulsen, "Improved quantification of small objects in near-infrared diffuse optical tomography," *Journal of Biomedical Optics* **9**, 1161-1171 (2004).
 30. C. L. Hutchinson, J. R. Lakowicz, and E. M. Sevick-Muraca, "Fluorescence lifetime-based sensing in tissues: a computational study," *Biophysical Journal* **68**, 1574-1582 (1995).
 31. E. M. Sevick-Muraca, G. Lopez, J. S. Reynolds, T. L. Troy, and C. L. Hutchinson, "Fluorescence and absorption contrast mechanisms for biomedical optical imaging using frequency-domain techniques," *Photochemistry and Photobiology* **66**, 55-64 (1997).
 32. R. C. Haskell, L. O. Svaasand, T. T. Tsay, T. C. Feng, and M. S. McAdams, "Boundary-conditions for the diffusion equation in radiative-transfer," *Journal of the Optical Society of America A* **11**, 2727-2741 (1994).

33. M. Keijzer, W. M. Star, and P. R. M. Storch, "Optical diffusion in layered media," *Applied Optics* **27**, 1820-1824 (1998).
34. A. H. Hielscher, S. L. Jacques, L. Wang, and F. K. Tittel, "The influence of boundary conditions on the accuracy of diffusion theory in time-resolved spectroscopy of biological tissues," *Physics in Medicine and Biology* **40**, 1957-1975 (1995).
35. J. N. Reddy, *An Introduction to the Finite Element Method* (McGraw-Hill, New York, 2004).
36. R. H. Gallagher, *Finite Element Analysis: Fundamentals* (Prentice Hall, Englewood Cliffs, NJ, 1975).
37. S. R. Arridge, and M. Schweiger, "A gradient based optimization scheme for optical tomography," *Optics Express* **2**, 213-225 (1998).
38. R. S. Dembo, and T. Steihaug, "Truncated Newton algorithms for large-scale unconstrained optimization," *Mathematical Programming* **26**, 190-212 (1983).
39. R. Roy, and E. M. Sevick-Muraca, "Truncated Newton's optimization scheme for absorption and fluorescence optical tomography: Part I theory and formulation," *Optics Express* **4**, 353-371 (1999).
40. R. Roy, and E. M. Sevick-Muraca, "Truncated Newton's optimization scheme for absorption and fluorescence optical tomography: Part II reconstruction from synthetic measurements," *Optics Express* **4**, 372-382 (1999).

41. R. Roy, and E. M. Sevick-Muraca, "Active constrained truncated Newton method for simple-bound optical tomography," *Journal of Optical Society of America A* **17**, 1627-1641 (2000).
42. F. Facchine, J. Judice, and J. Soares, "An active set Newton algorithm for large-scale nonlinear programs with box constraints," *SIAM Journal of Optimization* **8**, 158–186 (1998).
43. R. Pytlak, "An efficient algorithm for large-scale nonlinear programming problems with simple bounds on the variables," *SIAM Journal of Optimization* **8**, 532-560 (1998).
44. H. H. Barrett, and K. J. Myers, *Foundations of Image Science* (John Wiley & Sons, Inc., Hoboken, NJ, 2004).
45. A. R. P. Fortin, "Detection-theoretic evaluation in digital radiography and optical tomography," Ph.D. thesis, The University of Arizona, Tucson, AZ (2002).
46. F. O. Bochud, C. K. Abbey, and M. P. Eckstein, "Statistical texture synthesis of mammographic images with the clustered lumpy backgrounds," *Optics Express* **4**, 33-43 (1999).
47. J. A. Hanley, and B. J. McNeil, "The meaning and use of the area under a receiver operating characteristics (ROC) curve," *Radiology* **143**, 26-36 (1982).
48. J. A. Hanley, and B. J. McNeil, "A method of comparing the areas under receiver operating characteristics curves derived from the same cases," *Radiology* **148**, 839-843 (1983).

49. N. A. Obuchowski, "Fundamentals of clinical research for radiologist," *American Journal of Radiology* **184**, 364-372 (2005).
50. H. Hotelling, "The generalization of Student's ratio," *The Annals of Mathematical Statistics* **2**, 360-378 (1931).
51. H. H. Barrett, J. Yao, J. P. Rolland, and K. J. Myers, "Model observers for assessment of image quality," *Proceedings of National Academy of Sciences* **90**, 9758-9765 (1993).
52. E. M. Sevick-Muraca, and D. Y. Paithankar, "Fluorescent imaging system and measurement," in *Patent Number 5,865,754*, (U. S. Patent Office, Washington, DC, 1999).
53. D. Y. Paithankar, A. U. Chen, B. W. Pogue, M. S. Patterson, and E. M. Sevick-Muraca, "Imaging of fluorescent yield and lifetime from multiply scattered light reemitted from random media," *Applied Optics* **36**, 2260-2272 (1997).
54. A. Godavarty, M. J. Eppstein, C. Zhang, S. Theru, A. B. Thompson, M. Gurfinkel, and E. M. Sevick-Muraca, "Fluorescence-enhanced optical imaging in large tissue volumes using a gain-modulated ICCD camera," *Physics in Medicine and Biology* **48**, 1701–1720 (2003).
55. A. D. Klose, and A. H. Hielscher, "Iterative scheme for the optical tomography based on the equation of the radiative transfer," *Medical Physics* **26**, 1698-1707 (1999).

56. V. Ntziachristos, and B. Chance, "Accuracy limits in the determination of absolute optical properties using time-resolved NIR spectroscopy," *Medical Physics* **28**, 1115-1124 (2001).
57. R. Roy, A. B. Thompson, A. Godavarty, and E. M. Sevick-Muraca, "Tomographic fluorescence imaging in tissue phantoms: a novel reconstruction algorithm and imaging geometry," *IEEE Transactions on Medical Imaging* **24**, 137-154 (2005).
58. A. B. Thompson, D. J. Hawrysz, and E. M. Sevick-Muraca, "Near-infrared contrast-enhanced imaging with area illumination and area detection: the forward imaging problem," *Applied Optics* **42**, 4125-4136 (2003).
59. A. Godavarty, "Fluorescence enhanced optical tomography on breast phantoms with measurements using a gain modulated intensified CCD imaging system," Ph.D. thesis, Texas A&M University, College Station, TX (2003).
60. R. Marchesini, A. Bertoni, S. Andreola, E. Melloni, and A. E. Sichirollo, "Extinction and absorption coefficients and scattering phase functions of human tissues in vitro," *Applied Optics* **28**, 2318-2324 (1989).
61. V. G. Peters, D. R. Wymant, M. S. Patterson, and G. L. Frank, "Optical properties of normal and diseased human breast tissues in the visible and near infrared," *Physics in Medicine and Biology* **35**, 1317-1334 (1990).
62. K. A. Kang, B. Chance, S. Zhao, S. Srinivasan, E. Patterson, and R. Troupin, "Breast tumor characterization using near-infrared spectroscopy," *Proceedings of*

Photon Migration and Imaging in Random Media and Tissues **1888**, 487-499 (1993).

63. K. Suzuki, Y. Yamashita, K. Ohta, M. Kaneko, M. Yoshida, and B. Chance, "Quantitative measurements of optical parameters in normal breasts using time resolved spectroscopy: *in vivo* results of 30 Japanese women," Journal of Biomedical Optics **1**, 330-334 (1996).
64. T. L. Troy, D. L. Page, and E. M. Sevick-Muraca, "Optical properties of normal and diseased breast tissues: prognosis for optical mammography," Journal of Biomedical Optics **1**, 342-355 (1996).
65. B. J. Tromberg, O. Coquoz, J. Fishkin, T. Pham, E. R. Anderson, J. Butler, M. Cahn, J. D. Gross, V. Venugopalan, and D. Pham, "Non-invasive measurements of breast tissue optical properties using frequency-domain photon migration," Philosophical Transactions of the Royal Society of London Series B-Biological Sciences **352**, 661-668 (1997).
66. D. Grosenick, H. Wabnitz, H. H. Rinneberg, K. T. Moesta, and P. M. Schlag, "Development of a time-domain optical mammography and first *in vivo* applications," Applied Optics **38**, 2927-2943 (1999).
67. N. Shah, A. Cerussi, C. Eker, J. Espinoza, J. Butler, J. Fishkin, R. Hornung, and B. J. Tromberg, "Noninvasive functional optical spectroscopy of human breast tissue," Proceedings of the National Academy of Sciences **98**, 4420-4425 (2001).

68. T. Durduran, R. Choe, J. P. Culver, L. Zubkov, M. J. Holboke, J. Giammarco, B. Chance, and A. G. Yodh, "Bulk optical properties of healthy female breast tissue," *Physics in Medicine and Biology* **47**, 2847-2861 (2002).
69. J. P. Culver, R. Choe, M. J. Holboke, L. Zubkov, T. Durduran, A. Slemp, V. Ntziachristos, B. Chance, and A. G. Yodh, "Three-dimensional diffuse optical tomography in the parallel plane transmission geometry: evaluation of a hybrid frequency domain/continuous wave clinical system for breast imaging," *Medical Physics* **30**, 235-247 (2003).
70. N. Shah, A. E. Cerussi, D. Jakubowski, D. Hsiang, J. Butler, and B. J. Tromberg, "Spatial variations in optical and physiological properties of healthy breast tissue," *Journal of Biomedical Optics* **9**, 534-540 (2004).
71. R. Roy, A. Godavarty, and E. M. Sevick-Muraca, "Fluorescence-enhanced optical tomography using referenced measurements of heterogeneous media," *IEEE Transactions on Medical Imaging* **22**, 824-836 (2003).
72. M. G. Breitfeld, and D. F. Shanno, "Preliminary computational experience with modified log-barrier function for large-scale nonlinear programming," in *Large Scale Optimization: State of the Art*, W. W. Hager, D. W. Hearn, and P. M. Pardalos, eds. (Kluwer Academic, Dordrecht, The Netherlands, 1994), pp. 45–67.
73. M. J. Eppstein, D. E. Dougherty, D. J. Hawrysz, and E. M. Sevick-Muraca, "3-D Bayesian optical imaging reconstruction with domain decomposition," *IEEE Transactions on Medical Imaging* **20**, 147-161 (2001).

74. P. R. Bakic, M. Albert, D. Brzakovic, and A. D. A. Maidment, "Mammogram synthesis using a 3D simulation. I. Breast tissue model and image acquisition simulation," *Medical Physics* **29**, 2131-2139 (2002).
75. A. R. Pineda, and H. H. Barrett, "Figures of merit for detectors in digital radiography. II. Finite number of secondaries and structured backgrounds," *Medical Physics* **31**, 359-367 (2004).
76. A. K. Sahu, R. Roy, A. Joshi, and E. M. Sevick-Muraca, "Evaluation of anatomical structure and nonuniform distribution of imaging agent in nearinfrared fluorescence-enhanced optical tomography," *Optics Express* **13**, 10182-10199 (2005).
77. H. C. Gifford, R. G. Wells, and M. A. King, "A comparison of human observer LROC and numerical observer ROC for tumor detection in SPECT images," *IEEE Transactions on Nuclear Science* **46**, 1032-1037 (1999).
78. C. Lartizien, P. E. Kinahan, and C. Comtat, "Volumetric model and human observer comparisons of tumor detection for whole-body positron emission tomography " *Academic Radiology* **11**, 637-648 (2004).
79. S. D. Wollenweber, B. M. W. Tsui, D. S. Lalush, E. C. Frey, and G. T. Gullberg, "Evaluation of myocardial defect detection between parallel-hole and fan-beam SPECT using the Hotelling trace," *IEEE Transactions on Nuclear Science* **45**, 2205-2210 (1998).
80. M. Chen, J. E. Bowsher, A. H. Baydush, K. L. Gilland, D. M. DeLong, and R. J. Jaszczak, "Using the Hotelling observer on multislice and multiview simulated

- SPECT myocardial images," IEEE Transactions on Nuclear Science **49**, 661-667 (2002).
81. R. M. Gagne, B. D. Gallas, and K. J. Myers, "Toward objective and quantitative evaluation of imaging systems using images of phantoms," Medical Physics **33**, 83-95 (2005).
 82. L. Chen, and H. H. Barrett, "Task-based lens design with application to digital mammography," Journal of Optical Society of America A **22**, 148-167 (2005).
 83. K. Cheong, and E. Clarkson, "Detectability study on OCT in the presence of speckle with Hotelling observer," Medical Physics **32**, 1915-1915 (2005).
 84. E. M. Sevick-Muraca, E. Kuwana, A. Godavarty, J. P. Houston, A. B. Thompson, and R. Roy, "Near infrared fluorescence imaging and spectroscopy in random media and tissues," in *Biomedical Photonics Handbook*, J. Vo-Dinh, ed. (CRC Press, Boca Raton, FL, 2003), Chap. 8.
 85. M. A. Kupinski, E. Clarkson, J. W. Hoppin, L. Chen, and H. H. Barrett, "Experimental determination of object statistics from noisy images," Journal of Optical Society of America A **20**, 421-429 (2003).
 86. S. Park, E. Clarkson, M. A. Kupinski, and H. H. Barrett, "Efficiency of the human observer detecting random signals in random backgrounds," Journal of Optical Society of America A **22**, 3-26 (2005).
 87. K. Hwang, J. P. Houston, J. C. Rasmussen, A. Joshi, S. Ke, C. Li, and E. M. Sevick-Muraca, "Improved excitation light rejection enhances small-animal

- fluorescent optical imaging," *Journal of Molecular Imaging* **4**, 194-204 (2005).
88. K. Hwang, and E. M. Sevick-Muraca, "Influence of excitation light rejection on forward model mismatch," (submitted to *Journal of Biomedical Optics*, 2006).
 89. H. Lohinger, *Teach/Me Data Analysis* (Springer-Verlag, Berlin-New York-Tokyo, 1999).
 90. B. B. Glasgow, M. S. Glaser, and R. H. Whitley, "Remote imaging in the ultraviolet using intensified and nonintensified CCDs," *Proceedings of SPIE* **2173**, 85-96 (1994).
 91. E. J. Ientilucci, "Synthetic simulation and modeling of image intensified CCDs (IICCD)," M.S. thesis, Rochester Institute of Technology, Rochester, NY (2000).
 92. J. D. Sain, and H. H. Barrett, "Performance evaluation of a modular gamma using a detectability index," *Journal of Nuclear Medicine* **44**, 58-66 (2003).
 93. W. A. Kalender, A. Polacin, and C. Suss, "A comparison of conventional and spiral CT - an experimental-study on the detection of spherical lesions," *Journal of Computer Assisted Tomography* **18**, 167-176 (1994).
 94. I. Weinberg, S. Majewski, A. Weisenberger, A. Markowitz, L. Aloj, L. Majewski, D. Danforth, J. Mulshine, K. Cowan, J. Zujewski, C. Chow, E. Jones, V. Chang, W. Berg, and J. Frank, "Preliminary results for positron emission mammography: real-time functional breast imaging in a conventional mammography gantry," *European Journal of Nuclear Medicine* **23**, 804-806 (1996).

95. R. M. L. Warren, and C. Hayes, "Localization of breast lesions shown only on MRI - a review for the UK study of MRI screening for breast cancer," *British Journal of Radiology* **73**, 123-132 (2000).
96. J. A. Swets, R. M. Dawes, and J. Monahan, "Psychological science can improve diagnostic decisions," *Psychological Sciences in the Public Interests* **1**, 1-26 (2000).
97. H. H. Barrett, T. Gooley, K. Girodias, J. P. Rolland, T. White, and J. Yao, "Linear discriminants and image quality," *Image and Vision Computing* **10**, 451-460 (1992).
98. H. P. Chan, C. J. Vyborny, H. McMahon, C. E. Metz, K. Doi, and E. A. Sickles, "Digital mammography - ROC studies of the effects of pixel size and unsharp-mask filtering on the detection of subtle microcalcifications," *Investigative Radiology* **22**, 581 -589 (1987).
99. J. A. Swets, D. J. Getty, R. M. Pickett, C. J. Dorsi, S. E. Seltzer, and B. J. McNeil, "Enhancing and evaluating diagnostic-accuracy," *Medical Decision Making* **11**, 9-18 (1991).
100. Y. L. Jiang, R. M. Nishikawa, D. E. Wolverton, C. E. Metz, M. L. Giger, R. A. Schmidt, C. J. Vyborny, and K. Doi, "Malignant and benign clustered microcalcifications: automated feature analysis and classification," *Radiology* **198**, 671-678 (1996).

101. F. Schmidt, K. A. Hartwagner, E. B. Spork, and R. Groell, "Medical audit after 26,711 breast imaging studies - Improved rate of detection of small breast carcinomas (Classified as Tis or T1a,b)," *Cancer* **83**, 2516-2520 (1998).
102. Z. M. Huo, M. L. Giger, C. J. Vyborny, and C. E. Metz, "Breast cancer: effectiveness of computer-aided diagnosis - Observer study with independent database of mammograms," *Radiology* **224**, 560-568 (2002).
103. N. Houssami, L. Irwig, J. M. Simpson, M. McKessar, S. Blome, and J. Noakes, "The influence of clinical information on the accuracy of diagnostic mammography," *Breast Cancer Research and Treatment* **85**, 223-228 (2004).
104. A. Jensen, I. Vejborg, N. Severinsen, S. Nielsen, F. Rank, G. J. Mikkelsen, J. Hilden, D. Vistisen, U. Dyreborg, and E. Lynge, "Performance of clinical mammography: a nationwide study from Denmark," *International Journal of Cancer* **119**, 183-191 (2006).
105. C. C. Shaw, T. Wang, J. L. King, D. S. Breitenstein, T. S. Chang, K. M. Harris, A. B. Baratz, M. A. Ganott, R. Reginella, J. H. Sumkin, and D. Gur, "Computed radiography versus screen-film mammography in detection of simulated microcalcifications: a receiver operating characteristic study based on phantom images," *Academic Radiology* **5**, 173-180 (1998).
106. C. C. Goddard, R. J. Gilbert, G. Needham, and H. E. Deans, "Routine receiver operating characteristic analysis in mammography as a measure of radiologists' performance," *British Journal of Radiology* **71**, 1012-1017 (1998).

107. D. Gur, J. S. Stalder, L. A. Hardesty, B. Zheng, J. H. Sumkin, D. M. Chough, B. E. Shindel, and H. E. Rockette, "Computer-aided detection performance in mammographic examination of masses: Assessment," *Radiology* **233**, 418-423 (2004).
108. J. C. Dean, and C. C. Ilvento, "Improved cancer detection using computer-aided detection with diagnostic and screening mammography: prospective study of 104 cancers," *American Journal of Roentgenology* **187**, 20-28 (2006).
109. A. Miyawaki, "Fluorescence imaging of physiological activity in complex systems using GFP-based probes," *Current Opinion in Neurobiology* **13**, 591-596 (2003).
110. S. Kim, Y. T. Lim, E. G. Soltesz, A. M. De Grand, J. Lee, A. Nakayama, J. A. Parker, T. Mihaljevic, R. G. Laurence, D. M. Dor, L. H. Cohn, M. G. Bawendi, and J. V. Frangioni, "Near-infrared fluorescent type II quantum dots for sentinel lymph node mapping," *Nature Biotechnology* **22**, 93-97 (2004).
111. D. Elson, J. Requejo-Isidro, I. Munro, F. Reavell, J. Siegel, K. Suhling, P. Tadrous, R. Benninger, P. Lanigan, J. McGinty, C. Talbot, B. Treanor, S. Webb, A. Sandison, A. Wallace, D. Davis, J. Lever, M. Neil, D. Phillips, G. Stamp, and P. French, "Time-domain fluorescence lifetime imaging applied to biological tissue," *Photochemical & Photobiological Sciences* **3**, 795-801 (2004).
112. C. C. Paige, and M. A. Saunders, "LSQR: An algorithm for sparse linear equations and sparse least squares," *ACM Transactions on Mathematical Software* **8**, 43-71 (1982).

113. F. Fedele, J. P. Laible, and M. J. Eppstein, "Coupled complex adjoint sensitivities for frequency-domain fluorescence tomography: theory and vectorized implementation," *Journal of Computational Physics* **187**, 597-619 (2003).
114. W. H. Ehrenstein, and A. Ehrenstein, *Modern Techniques in Neuroscience Research* (Springer, New York, 1999).
115. J. E. Joy, E. E. Penhoet, and D. B. Petitti, *Saving Women's Lives: Strategies for Improving Breast Cancer Detection and Diagnosis* (National Academies Press, Washington, DC, 2005).
116. A. M. DeGrand, S. J. Lomnes, D. S. Lee, M. Pietrzykowski, S. Ohnishi, T. G. Morgan, A. Gogbashian, R. G. Laurence, and J. V. Frangioni, "Tissue-like phantoms for near-infrared fluorescence imaging system assessment and the training of surgeons," *Journal of Biomedical Optics* **11**, 014007 (2006).
117. 'Wolfram,' "<http://mathworld.wolfram.com/L2-InnerProduct.html>" (accessed on 10/17/2006).
118. 'Connexions,' "<http://cnx.org/content/m10684/latest/>" (accessed on 10/17/2006).
119. R. E. Walpole, and R. H. Myers, *Probability and Statistics for Engineers and Scientists* (Macmillan, New York, 1989).
120. W. S. Gosset, "The probable error of a mean," *Biometrika* **6**, 1–25 (1908).

APPENDIX A

A1. L_2 norm

Norm is a concept closely related to distance in metric spaces. For example, in ordinary vector analysis, the norm of a vector is the distance between the vector and the zero vector (origin). L_2 norm is a special type of norm which, for a vector \mathbf{f} in an N dimensional space such that \mathbf{f} can be represented as an ordered set $\{f_n\}$, is defined as:⁴⁴

$$\|\mathbf{f}\|_2 = \left[\sum_{n=1}^N |f_n|^2 \right]^{\frac{1}{2}} \quad (\text{A1})$$

L_2 norm is most commonly used norm because it is easy to derive and is a natural choice for least squares minimization problems.

A2. L_2 inner product

L_2 inner product of two real functions f and g on a metric space X with respect to some variable $x \in X$ is given by:¹¹⁷

$$(f, g)_{L_2} = \int_X fg \, dx \quad (\text{A2})$$

A3. Adjoint theorem

If \mathbf{a} and \mathbf{b} are vectors and \mathbf{A} is a linear operator, then the adjoint theorem states:

$$\langle \mathbf{a}, \mathbf{A}\mathbf{b} \rangle = \langle \mathbf{A}^* \mathbf{a}, \mathbf{b} \rangle, \quad (\text{A3})$$

where $\langle ., . \rangle$ denotes the standard inner product; A^* is the adjoint of A . For complex matrices the adjoint operator is the conjugate transpose operator.

A4. Stationary process

A random process where all of its statistical properties do not vary with time is known as stationary process. In a strict sense, the stationarity of a random process is defined by the time invariance of all of its probability distribution functions. Often times the stationarity requirements of a strict sense stationary (SSS) process are more than necessary and a more relaxed type, wide sense stationary (WSS), is used. A random process is stationary in a wide sense if it is shift invariant, i. e. the statistical properties do not change in space.^{44, 118}

APPENDIX B

B1. Central limit theorem

The central limit theorem can be stated as:¹¹⁹

If \bar{x} is the mean of a random sample size taken from a population with mean μ and finite variance σ^2 , then the limiting form of

$$z = \frac{\bar{x} - \mu}{\sigma / \sqrt{n}}, \quad (\text{B1})$$

as $n \rightarrow \infty$, is the standard normal distribution $\mathbb{N}(0,1)$.

B2. Student's t -distribution

The student's distribution arises in cases (probably true for all practical statistical work) where the random samples are selected from a normally distributed population whose variance is not known.

Suppose x_1, \dots, x_n are independent random variables selected from a normal distribution with mean μ and variance σ^2 . Let the mean of the sample be

$$\bar{x}_n = \frac{(x_1 + \dots + x_n)}{n}, \quad (\text{B2})$$

and variance of the sample be

$$s_n^2 = \frac{1}{n-1} \sum_{i=1}^n (x_i - \bar{x}_n)^2. \quad (\text{B3})$$

Central limit theorem shows that the estimate of the mean, which is represented Eq. (B1) is normally distributed with zero mean and unit variance. If the sample is large, s_n^2 provides a good estimate of the σ^2 . But if the sample size is small, the value of s_n^2 varies considerably from sample to sample and the distribution of

$$t = \frac{\bar{x}_n - \mu}{s_n / \sqrt{n}} \quad (\text{B4})$$

deviates appreciably from that of a standard normal distribution. Gosset¹²⁰ showed that t has the probability distribution function

$$h(t) = \frac{\Gamma((\nu+1)/2)}{\sqrt{\nu\pi}\Gamma(\nu/2)} \left(1 + \frac{t^2}{\nu}\right)^{-(\nu+1)/2} \quad (\text{B5})$$

with ν equal to $n-1$. The distribution of t is called t -distribution and the parameter ν is called the number of degrees of freedom. Note that the distribution depends only on ν , and the dependence on μ and σ^2 has been eliminated. This makes the t -distribution important for statistical analysis purposes. In other words, it enables statisticians to perform exact significance tests and construct exact confidence intervals based on the available, often small, size of the sample.

B3. Hotelling's T -square distribution

Hotelling's T -square distribution is a multivariate method and is the multivariate counterpart of the Student's t -distribution. It is a statistic for the multivariate test of

difference between the mean values of two groups. The null hypothesis is that the centroids* don't differ between two groups.

From the above Section B2, we see that

$$t = \frac{\bar{x}_n - \mu}{s_n / \sqrt{n}}$$

has a t -distribution provided that x is normally distributed, and is applicable as long as x does not differ greatly from a normal distribution. In order to test the hypothesis that the value of the μ is equal to μ^0 , a hypothesized value of population mean, we will have

$$t = \frac{\bar{x}_n - \mu^0}{s_n / \sqrt{n}} \quad (\text{B6})$$

which gives

$$t^2 = \frac{(\bar{x}_n - \mu^0)^2}{s_n^2 / n} = n(\bar{x}_n - \mu^0)(s_n^2)^{-1}(\bar{x}_n - \mu^0). \quad (\text{B7})$$

In the multivariate framework, when t^2 is generalized for p variables X_1, X_2, \dots, X_p , each a vector of length n , it becomes

$$T^2 = n(\bar{X} - \mu^0)^T S^{-1}(\bar{X} - \mu^0), \quad (\text{B8})$$

$$\text{where } \bar{X} = \begin{bmatrix} \bar{X}_1 \\ \bar{X}_2 \\ . \\ . \\ \bar{X}_p \end{bmatrix} \text{ and } \mu^0 = \begin{bmatrix} \mu_1^0 \\ \mu_2^0 \\ . \\ . \\ \mu_p^0 \end{bmatrix}.$$

* The centroid of several continuous variables is the vector of means of those variables.

S^{-1} is the inverse of the sample variance-covariance, or simply, the covariance matrix, S , which is given by

$$S_{ij} = \frac{1}{n-1} (X_i - \bar{X}_i)(X_j - \bar{X}_j)^T, \quad (\text{B9})$$

where superscript T denotes the matrix transpose. S is a square matrix of size p .

APPENDIX C

Bias in Hotelling SNR

In Section 4.2.4.1, Eq. (4.19) describes that the overall covariance matrix, $\mathbf{K}_{\mathbf{g}}$, is decomposed into two matrices, $\mathbf{K}_{\bar{\mathbf{g}}}$ and $\bar{\mathbf{K}}_n$. The disadvantage of this decomposition is that it introduces bias in the estimate of the SNR_{Hot} . In other words, the estimate of SNR_{Hot} varies with the number, N , of imaging data sets, \mathbf{g} . The value of SNR_{Hot} decreases as N increases and reaches a constant (true value of SNR_{Hot}) for large N . To illustrate using a smaller data set than described in the text, Fig. C1 describes a plot of SNR_{Hot} versus N , where the imaging measurements were conducted on the breast phantom with only one source lighted so that the length, M , of each vector \mathbf{g} equals 128. Figure C.1 shows that the true value of SNR_{Hot} is achieved for approximately $N \geq 10 \times M$. Sain *et al.*⁹² also advocate using number of imaging data sets ten times more than the length of \mathbf{g} . For this reason, the theoretical value of N for our study involving 25 sources and 128 detectors should be $10 \times 25 \times 128 = 32000$. Due to the computation time limitations and the fact that the values of SNR_{Hot} are used only relatively for comparing different case studies (with constant M), we chose $N=7000$ to obtain reasonable estimates of SNR_{Hot} .

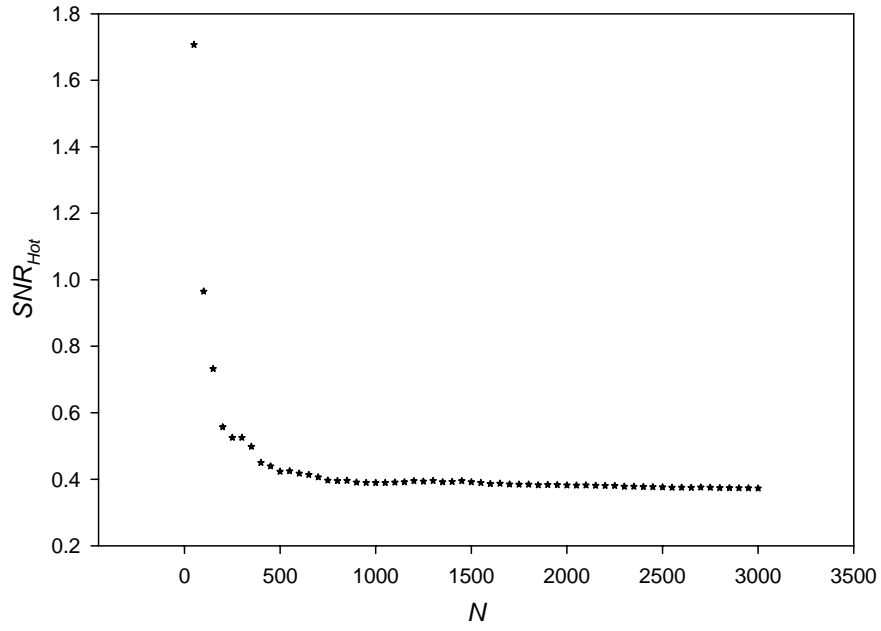


Fig. C.1 SNR_{Hot} computed from simulated measurements of intensity, I_{AC} , in one hundred percent lumpy backgrounds of endogenous as well as exogenous optical properties vs. the number of imaging data sets, N . The centroid of the target lies in the z-axis and it is contrasted from its surroundings by 10:1. One twenty eight point detectors (as shown in Fig. 4.2) are used for the collection of light and only one source is lighted such that the measurement data set is a vector of 128×1 .

VITA

AMIT K. SAHU

EDUCATION B. Tech. (2002) Chemical Engineering,
 Indian Institute of Technology, Roorkee, India

 Ph. D. (2006) Chemical Engineering,
 Texas A&M University, College Station, TX

PUBLICATIONS

- **Amit K. Sahu**, Ranadhir Roy, Amit Joshi, and Eva M. Sevick-Muraca, "Evaluation of anatomical structure and non-uniform distribution of imaging agent in near-infrared fluorescence-enhanced optical tomography," *Optics Express*, vol. **13**(25), p. 10182-10199 (2005).
- **Amit K. Sahu**, Amit Joshi, Ranadhir Roy, and Eva M. Sevick-Muraca, "Simulated anatomical backgrounds for objective assessment of image quality (OAIQ) in optical tomography," *Proceedings of SPIE*, vol. **5693**, p. 513-520, *Optical Tomography and Spectroscopy of Tissue VI*; Britton Chance, Robert R. Alfano, Bruce J. Tromberg, Mamoru Tamura, Eva M. Sevick-Muraca; Eds. (2005).
- **Amit K. Sahu**, Amit Joshi, and Eva M. Sevick-Muraca, "Effect of random structured backgrounds on Hotelling SNR in fluorescence imaging systems," *Proceedings of the 3rd IEEE International Symposium on Biomedical Imaging: Macro to Nano 2006*, p. 586-589 (2006).
- **Amit K. Sahu**, Amit Joshi, Matthew A. Kupinski, and Eva M. Sevick-Muraca, "Assessment of fluorescence-enhanced optical imaging system using the Hotelling observer," *Optics Express*, vol. **14**(17), p. 7642-7660 (2006).
- **Amit K. Sahu** and Eva M. Sevick-Muraca, "Assessment of a fluorescence-enhanced optical imaging system through psychophysical analysis of simulated patient data," (2006) (in preparation).